Reaction Characteristics of Methanol Partial Oxidation Using Thermal Effects of a Porous Material

Yasuhiro RAI

2013

Contents

Acknowledgements

I would like to express my sincere thanks and gratitude to Professor Kazuyoshi Nakabe for his invaluable and kindhearted guidance and professional suggestion on my research work throughout my seven years in Mechanics of Thermal Fluids and Materials Laboratory of Kyoto University.

I would also like to show my deep appreciation to Associate Professor Kazuya Tatsumi for his generous and constructive advice on my research activities in Mechanics of Thermal Fluids and Materials Laboratory of Kyoto University.

I would like to express sincere gratitude to Professor Toshiro Makino and Professor Satoru Komori for their valuable suggestion on my thesis from the perspectives of their professional fields. Their reviews of my thesis considerably helped me to understand more deeply the phenomena presented in the thesis.

I would also like to express my gratitude to Professor Alexander Taylor and Professor Yannis Hardalupas and the members of Multiscale Flow Dynamics Laboratory of Imperial College London. They kindly accepted me to visit their laboratory for three months to learn numerical and experimental procedures regarding droplet evaporation and combustion process in internal combustion engines. Their collaboration helped me to learn the mechanism of droplet evaporation and liquid fuel combustion.

I must also thank Mr. Keisuke Kuwabara and Mr. Masaaki Mizuno for their kindness and patience in instructing me the way to organize an experiment and answering to all the queries regarding my research work.

My sincere thanks are also due to Messrs. H. Kogame, M. Kawabe and Y. Niibayashi for their greathearted support in the experimental work. Some of the works in this thesis were assisted by them with their tremendous efforts.

Special thanks go to the staff members of the mechanical workshop of Faculty of Engineering, Kyoto University. Many of the experimental apparatuses were processed and

manufactured in the workshop on their professional advice.

I would also like to sincerely thank all the members and ex-members of Mechanics of Thermal Fluids and Materials Laboratory for their kindhearted collaborations.

Finally, I would like to show my deepest gratitude to my family for their love, patience, understanding and support throughout my ten years study in Kyoto University.

Chapter 1

Introduction

1.1 Background

Because of the serious problems of fossil fuel depletion and global climate change, hydrogen has gained more attention in recent years as a promising energy carrier. Hydrogen can be used as a fuel for high-efficiency energy devices such as fuel cells and hydrogen engines, which emit only water when pure hydrogen is fed. Moreover, in terms of energy security, hydrogen is a candidate fuel for a secure future energy system because it can be derived from a variety of fuels. However, hydrogen is a secondary energy carrier and must be artificially synthesized from other materials. Furthermore, owing to hydrogen's extremely low energy density, pure hydrogen storage and supply systems need technological innovations such as super-high-pressure tanks, hydrogen absorbing alloys, or hydrogen liquefaction technologies, which will require considerable investments of time, energy, and capital [1]. Therefore, during the transition period until the required hydrogen infrastructure is realized, reforming of various hydrocarbon fuels is the only way to utilize hydrogen devices efficiently. The primary motivation of this study was to obtain the designing principle of a 1-kW-class compact fuel reformer that is suitable for a home-use hydrogen energy system.

Hydrogen can be derived from hydrocarbon fuels through many methods including steam reforming (STR), partial oxidation (POX), and autothermal reforming (ATR).

Detailed characteristics of each reaction are presented in Chap. 2. Among these reforming reactions, catalytic STR is widely used in industrial fields because it can achieve a relatively high hydrogen yield [2–4]. Recently, novel systems have been developed that utilize heat sources such as industrial plants, nuclear power plants [5,6], and solar thermal energy [7,8]. Some plants are already in operation as demonstrative cases. However, in relatively small-scale systems, the complexity of an STR reactor involving a water vapor generator and external heat source makes the overall system difficult to realize. Moreover, because the STR reaction is fairly slow, determining the optimum use of a catalyst is extremely important for an adequate conversion ratio; else, catalyst degradation or soot deposition drastically reduces the efficiency of the reforming reaction. Fuels for STR reactors are also limited to those having low-temperature boiling points. Thus, numerous challenges have yet to be overcome in the design and construction of a compact and inexpensive STR system.

POX—another process for obtaining hydrogen-rich gas—is also known as fuel-rich combustion. Because oxygen is involved in the process, the hydrogen yield of POX is lower than that of STR. Moreover, POX produces a relatively large amount of CO, which has to be reduced in treatment reactors [9,10]. However, because POX is an exothermic reaction and occurs without a catalyst, compact and economic systems can be realized. Furthermore, POX can work with various fuels, including low-quality fuels or heavy fuels, which guarantees the fuel-diversity of the reforming system [11]. The reaction speed of POX is much faster than that of STR, however, if compared with complete combustion, POX is a relatively slow reaction, and the flame temperature and heat release rate are markedly lower.

In a practical use of a fuel reformer, both of the above reactions are combined to take both advantages of these reactions, i.e., oxidizer as well as water vapor are simultaneously introduced with fuel to the reactor. This combined reaction is called ATR [12]. When applying a fuel reformer to automobiles and small-scale home-use hydrogen systems, fast start-up and quick response characteristics are the primary concern in designing the reactor.

ATR is a useful reaction in such systems, where the advantage of POX can be utilized in a start-up condition by increasing the amount of oxidizer, while highly efficient STR can be used in a steady operation by decreasing the amount of oxidizer. Therefore, bearing in mind such a system using ATR, it is crucial to understand in detail the reaction characteristics of POX to design highly efficient fuel reformer.

Because POX is a combustion reaction in a fuel-rich condition, it is difficult to obtain stable reactions with high reaction rates in conventional reactors. Therefore, it is necessary to apply some methods to stabilize the flame or enhance the reaction rate within the reactor. Generally, the flame stabilization can be applied to combustors through several methods: formation of attachment points by secondary flows induced by baffle plates or swirling wings [13–15]; heat recirculation by heat exchange between the exhaust gas and premixed gas [16,17]; flow recirculation of high-temperature radical species in the exhaust gas (EGR) [18,19]; and utilization of a porous material to realize additional heat transfer modes [20–22]. Flame stabilization methods can extend the operating limits further than those of conventional combustors. These methods are often applied to fuel-lean combustion; however, several papers can also be found where these methods are applied to fuel-rich combustion [23,24].

Among the above methods, one of the most promising is to use a porous material as a flame stabilizer. In the presence of a porous material, conduction heat transfer through a solid phase of the porous material from the reaction region to the mixture and thermal radiation exchange between the solid surfaces of the porous material are added to the conventional heat transfer modes. These additional heat transfer and radiation flux is often described as "internal heat recirculation" [25,26]. Due to internal heat recirculation, a stabilized flame can be formed within or in the vicinity of the porous material having a high reaction rate under a wide range of mixture flow rates and equivalence ratios that the flame cannot sustain in a conventional open flame reactor.

In addition to the flame stabilization effect of a porous material, another characteristic of a porous material is its ability to act as a radiation converter, as proposed by Echigo [27].

When a porous material is introduced in the downstream of the reaction region in a combustion chamber, the working gas can flow through the porous material. Because of a high convective heat transfer coefficient of the porous material, enthalpy of the working gas is efficiently converted into radiation emission and induces energy regeneration from the solid surface of the porous material to the upstream reaction region. Okuyama et al. [28] introduced the concept of the radiation converter into a combustion chamber and realized energy regeneration from the exhaust gas to the unburned mixture through irradiation from the radiation converter. Due to the effect of energy regeneration, a super-rich flame can be stabilized beyond the flammability limit. This concept of a porous radiation converter has been applied to a wide variety of industrial burners [29,30].

The application of porous materials to combustion devices is often intended to realize higher combustion efficiency, lower NO_x emission, higher power output, larger turn-down ratio, higher stability, and so on. When these characteristics are to be achieved in combustors with porous materials, the interaction between the flame and porous material is predominant over the basic combustion characteristics. The most significant factor determining the combustion characteristics is the relative location of the flame to the porous material [31,32]. Several factors are known to determine the flame location: the velocity distribution in the reaction region, preheating temperature of the mixture, and energy flux induced by conduction and radiation heat transfers within the porous material.

Many researchers have investigated the factors determining the flame location and stability in cases of fuel-lean combustion when a porous material is involved in the reaction. Yoshizawa et al. [33] and Hanamura et al. [34] numerically studied steady and unsteady flame behaviors and their energy balances within the reactor when the flame is stabilized inside the porous material. They discovered that the flame temperature decreases when the flame is located inside the porous material compared with a flame stabilized outside. Min and Shin [35] investigated the location of a flame stabilized inside the porous material both numerically and experimentally. They discussed the effect on the flame stability of internal heat recirculation within the porous material realized by both conduction and radiation

transfers. They also showed the possibility of flame stabilization by means of a porous material under very low mixture flow rate conditions where a conventional combustor cannot sustain the flame due to backfire.

On the other hand, several researchers have reported that the flame can be stabilized under fuel-rich conditions beyond the upper flammability limit using internal heat recirculation by a porous material. Al-Hamamre et al. [36] investigated the flame location, sooting limit, and product gas composition in kerosene fuel-rich flame stabilized in a ceramic foam combustor. Itaya et al. [37] showed that methane fuel-rich flame with a very low mixture flow rate can be stabilized at the outlet of the porous material because the radiation energy loss from the solid surface prevents the flame from moving into the porous material. In their study, even when the burning velocity was higher than the averaged mixture velocity, the flame was still able to stabilize in the vicinity of the porous material. Pedersen-Mjaanes et al. [38] reported that hydrogen-rich gas can be produced by fuel-rich flames of methanol, methane, and octane stabilized in a reactor composed of several types of porous materials with different porosities. However, even though numerous studies have contributed to fuel-rich combustion in porous materials, few have looked into correlating the heat and fluid flow characteristics of fuel-rich combustion in a porous reactor to the reaction characteristics and hydrogen production performance.

Therefore, in the research on which this thesis is based, we investigated the influential factors on the reaction location, flame shape, and its reaction efficiency on the basis of non-catalytic methanol POX in a honeycomb-type fuel reformer. A ceramic honeycomb was introduced in the reactor as a flame stabilizer; the steady POX flame was stabilized in the vicinity of the honeycomb. The experiments were conducted under various equivalence ratio and mixture flow rate conditions. For the respective experiments, the gas compositions as well as the gas and solid temperature distributions were measured in detail. The flame shapes and velocity distributions within the reactor were also observed and the results were correlated to the reforming performance and reaction stability. The results of the experiments were used to discuss the effects of the thermal interaction between the flame

and ceramic honeycomb on the reaction performance in terms of thermal engineering.

After the reaction characteristics of POX stabilized by the ceramic honeycomb were obtained, we attempted to further enhance the POX performance and increase the hydrogen yield by introducing the concept of a radiation converter into the present fuel reformer. A radiation converter was also constructed from the same ceramic honeycomb used as the flame stabilizer. The radiation converter was expected to enhance the preheating of the mixture gas by means of radiation energy regeneration. Thus, the effects of ceramic honeycomb locations, equivalence ratios, and mixture flow rates on the reforming performance were investigated experimentally, and the optimum use of a ceramic honeycomb as a radiation converter is proposed.

Based on the results obtained in the experiments, we propose the optimum use of a ceramic honeycomb as a porous material in terms of flame stabilization, reaction characteristics and hydrogen yield for non-catalytic POX of methanol. This knowledge of POX can be applied further to the optimum thermal management and reactor design of fuel reformer based not only on POX, but also on ATR.

1.2 Outline of the Thesis

Chapter 2 presents the basic characteristics of the reactions related to a fuel reformer. The advantages and disadvantages of these reactions including non-catalytic POX are given to clarify the concept of the present fuel reformer. Then, the benefits of a fuel reformer and fuel cell (FR-FC) system over the conventional internal combustion engines for power generation are investigated to obtain the efficiency requirements of a fuel reformer.

Chapter 3 investigates the reaction characteristics of non-catalytic methanol POX in the presence of a ceramic honeycomb working as a flame stabilizer. The experiment is conducted in various equivalence ratios where the detailed temperature distributions are measured to clarify the role of the ceramic honeycomb in the POX reaction. The chemical equilibrium compositions are also calculated and compared with the experimental results. Then, the optimum operating condition of non-catalytic methanol POX in terms

of hydrogen production are presented.

Chapter 4 discusses the relation between the reaction performance and flame structure. The mixture velocity represented by thermal load is varied to closely look into the flame structure. The flame temperatures, locations, and shapes are observed experimentally and the effects of the thermal interaction between the flame and ceramic honeycomb are disclosed and related to the reforming performance.

Chapter 5 reports the possibility of the enhancement of the POX reaction by utilizing energy regeneration. By adding the secondary ceramic honeycomb in the post-reaction region, the temperature of the flame is expected to increase by energy regeneration realized by the nature of a radiation converter of the ceramic honeycomb. The degree of energy regeneration with respect to the gap distances, equivalence ratios, and thermal loads are investigated, then the optimum use of a ceramic honeycomb as a radiation converter is proposed.

Chapter 6 finally summarizes the obtained knowledge and major conclusions in the thesis, and presents the suggestion to the further work in the future.

Bibliography

[1] Schlapbach, L., and Züttel, A., "Hydrogen-Storage Materials for Mobile Applications", *Nature*, Vol. 414 (2001), pp. 353–358.

[2] Rostrup-Nielsen, J. R., and Rostrup-Nielsen, T., "Large-Scale Hydrogen Production", *Cattech*, Vol. 6, No. 4 (2002), pp. 150–159.

[3] Emonts, B., Hansen, J. B., J, S. L., Höhlein, B., and Peters, R., "Compact Methanol Reformer Test for Fuel-Cell Powered Light-Duty Vehicles", *Journal of Power Sources*, Vol. 71 (1998), pp. 288–293.

[4] Lindström, B., and Pettersson, L. J., "Development of A Methanol Fuelled Reformer for Fuel Cell Applications", *Journal of Power Sources*, Vol. 118 (2003), pp. 71–78.

[5] Fukushima, K., and Ogawa, T., "Conceptual Design of Low-Temperature Hydrogen Production and High-Efficiency Nuclear Reactor Technology", *JSME International Journal Ser. B*, Vol. 47, No. 2 (2004), pp. 340–343.

[6] Hori, M., Matsui, K., Tashimo, M., and Yasuda, I., "Synergistic Hydrogen Production by Nuclear-Heated Steam Reforming of Fossil Fuels", *Progress in Nuclear Energy*, Vol. 47, No. 1–4 (2005), pp. 519-526.

[7] Möller, S., Kaucic, D., and Sattler, C., "Hydrogen Production by Solar Reforming of Natural Gas: A Comparison Study of Two Possible Process Configurations", *Transactions of the ASME*, Vol. 128 (2006), pp. 16–23.

[8] Pregger, T., Graf, D., Krewitt, W., Sattler, C., Roeb, M., and Möller, S., "Prospects of Solar Thermal Hydrogen Production Processes", *International Journal of Hydrogen Energy*, Vol. 34 (2009), pp. 4256–4267.

[9] Horng, R., Chou, H., Lee, C., and Tsai, H. "Characteristics of Hydrogen Produced by Partial Oxidation and Auto-Thermal Reforming in A Small Methanol Reformer", *Journal of Power Sources*, Vol. 161 (2006), pp. 1225–1233.

[10] Silva, A. M., Farias, A. M. D., Costa, L. O. O., Barandas, A. P. M. G., Mattos, L. V., Fraga, M. A., and Noronha, F. B. "Partial Oxidation and Water-Gas Shift Reaction in An Integrated System for Hydrogen Production from Ethanol", *Applied Catalysis A: General*, Vol. 334 (2008), pp. 179–186.

[11] Marda, J. R., DiBenedetto, J., McKibben, S., Evans, R. J., Czernik, S., French, R. J., and Dean, A. M., "Non-Catalytic Partial Oxidation of Bio-Oil to Synthesis Gas for Distributed Hydrogen Production", *International Journal of Hydrogen Energy*, Vol. 34, No. 20 (2009), pp. 8519–8534.

[12] Taki, M., Negishi, Y., and Kobayashi, N., "Development of Highly-Efficient Compact Methanol Fuel Reformer for Fuel Cells", *TOYOTA Technical Review*, Vol. 47, No. 2 (1997), pp. 76–81 (in Japanese).

[13] Choi, H.S., Katsumoto, Y., Nakabe, K., and Suzuki, K., "An Experimental Investigation of Mixing and Combustion Characteristics on the Can-Type Micro Combustor with A Multi-Jet Baffle Plate", *Fluid Mechanics and its Applications Turbulent, Mixing and Combustion*, Vol. 70 (2002), pp. 367–375.

[14] Yimer, I., Becker, H. A., and Grandmaison, E. W., "The Strong-Jet/Weak-Jet Problem: New Experiments and CFD", *Combustion and Flame*, Vol. 124 No. 3 (2001), pp. 481–502.

[15] Mostafa, A. A., Khalifa, M. M., and Shabana, E. A., "Experimental and Numerical Investigation of Multiple Rectangular Jets", *Experimental Thermal and Fluid Science*, Vol. 21 (2000), pp. 171–178.

[16] Weinberg, F. J., "Combustion Temperatures: The Future?", *Nature*, Vol. 233, No. 5317 (1971), pp. 239–241.

[17] Wünning, J. A., and Wünning, J. G., "Flameless Oxidation to Reduce Thermal NO-Formation", *Progress in Energy and Combustion Science*, Vol. 23, No. 1 (1997),

pp. 81–94.

[18] Pitz, R. W., and Daily, J. W., "Combustion in A Turbulent Mixing Layer Formed at A Rearward-Facing Step", *AIAA Journal*, Vol. 21, No. 11 (1983), pp. 1565–1570.

[19] Shanbhogue, S. J., Husain, S., and Lieuwen, T., "Lean Blowoff of Bluff Body Stabilized Flames: Scaling and Dynamics", *Progress in Energy and Combustion Science*, Vol. 35, No. 1 (2009), pp. 98–120.

[20] Howell, J. R., Hall, M. J., and Ellzey, J. L., "Combustion of Hydrocarbon Fuels within Porous Inert Media", *Progress in Energy and Combustion Science*, Vol. 22 (1996), pp. 121–145.

[21] Kamal, M.M. and Mohamad, A.A., "Combustion in Porous Media", *Proceedings of the Institution of Mechanical Engineers, Part A: Journal of Power and Energy*, Vol. 220, No. 5 (2006), pp. 487–508.

[22] Mujeebu, M. A., Abdullah, M. Z., Bakar, M. Z. A., Mohamad, A. A., and Abdullah, M. K., "A Review of Investigations on Liquid Fuel Combustion in Porous Inert Media", *Progress in Energy and Combustion Science*, Vol. 35 (2009), pp. 216–230.

[23] Schoegl, I., Newcomb, S. R., and Ellzey, J. L., "Ultra-Rich Combustion in Parallel Channels to Produce Hydrogen-Rich Syngas from Propane", International Journal of Hydrogen Energy, Vol. 34, No. 12 (2009), pp. 5152–5163.

[24] Brüggemann, P., Seifert, P., Meyer, B., and Müller-Hagedorn, M., "Influence of Temperature and Pressure on the Non-Catalytic Partial Oxidation of Natural Gas", *Chemical Product and Process Modeling*, Vol. 5, No. 1 (2010).

[25] Takeno, T., Sato, K., and Hase, K. "A Theoretical Study on an Excess Enthalpy Flame", *Proceedings of Symposium (International) on Combustion*, Vol. 18, No. 1 (1981), pp. 465-472.

[26] Tsuji, H., Gupta, A. K., Hasegawa, T., Katsuki, M., Kishimoto, K., and Morita, M. *High Temperature Air Combustion: From Energy Conservation to Pollution Reduction*, (2003), CRC Press.

[27] Echigo, R., "Effective Conversion Method between Gas Enthalpy and Thermal Radiation and Its Application to Industrial Furnaces", *Transactions of Japan Society of Mechanical Engineers Ser. B*, Vol. 48, No. 435 (1982), pp. 2315–2323 (in Japanese).

[28] Okuyama, M., Echigo, R., Yoshida, H., Koda, M., and Hanamura, K., "Spectral Radiation Properties of Super Fuel-Rich Premixed Flame", *Transactions of Japan Society of Mechanical Engineers Ser. B*, Vol. 60, No. 577 (1994), pp. 3145–3152 (in Japanese).

[29] Jugjai, S., and Polmart, N., "Enhancement of Evaporation and Combustion of Liquid Fuels through Porous Media", *Experimental Thermal and Fluid Science*, Vol. 27 (2003), pp. 901–909.

[30] Lammers, F. A., and de Goey, L. P. H., "A Numerical Study of Flash Back of Laminar Premixed Flames in Ceramic-Foam Surface Burners", *Combustion and Flame*, Vol. 133 (2003), pp. 47–61.

[31] Sathe, S. B., Kulkarni, M. R., Peck, R. E., and Tong, T. W., "An Experimental and Theoretical Study of Porous Radiant Burner Performance", *Proceedings of Twenty-Third Symposium (International) on Combustion*, (1990), pp. 1011–1018.

[32] Bouma, P. H., and de Goey, L. P. H., "Premixed Combustion on Ceramic Foam Burners", *Combustion and Flame*, Vol. 119 (1999), pp. 133–143.

[33] Yoshizawa, Y., Sasaki, K., and Echigo, R., "Analytical Study on the Structure of Radiation Controlled Flame", *Transactions of the Japan Society of Mechanical Engineers Ser. B*, Vol. 52, No. 482 (1986), pp. 3587–3593 (in Japanese).

[34] Hanamura, K., Echigo, R., and Yoshizawa, Y., "Structure and Transient Behavior of Radiation-Controlled Flame in A Highly Porous Medium", *Transactions of the Japan Society of Mechanical Engineers Ser. B*, Vol. 57, No. 533 (1991), pp. 315–321 (in Japanese).

[35] Min, D. K., and Shin, H. D., "Laminar Premixed Flame Stabilized Inside A Honeycomb Ceramic", *International Journal of Heat and Mass Transfer*, Vol. 34, No. 2 (1991), pp. 341–356.

[36] Al-Hamamre, Z., Voß, S., and Trimis, D., "Hydrogen Production by Thermal Partial Oxidation of Hydrocarbon Fuels in Porous Media Based Reformer", *International Journal of Hydrogen Energy*, Vol. 34 (2009), pp. 827–832.

[37] Itaya, Y., Miyoshi, K., Maeda, S., and Masatani, M., "Formation of Methane-Air Open Flame on the Surface of A Porous Ceramic Plate", *Kagaku Kogaku Ronbunshu*, Vol. 16, No. 1 (1990), pp. 56–63 (in Japanese).

[38] Pedersen-Mjaanes, H., Chan, L., and Mastorakos, E., "Hydrogen Production from Rich Combustion in Porous Media", *International Journal of Hydrogen Energy*, Vol. 30 (2005), pp. 579–592.

Chapter 2

Fuel Reforming Reactions

2.1 Introduction

A technological difficulty of constructing efficient hydrogen energy system lies on the H_2 supply method. Since most hydrogen atoms exist as chemical compounds in the environment, H_2 needs to be produced when used as a fuel of a hydrogen device by separating hydrogen atoms somehow from the hydrogen compounds such as water, hydrocarbon, and biomass materials. An efficient way to produce H_2 is still challenging and many researchers are exploring this topic [1]. There are several processes proposed to produce H_2 from hydrogen compounds: gasification of coal or petroleum, fuel reforming of hydrocarbon fuels, electrolysis of water, pyrolysis of water using solar thermal energy, and photosynthesis by microbes [2]. Among them, fuel reforming is our consideration to produce H_2.

In this chapter, several reactions related to fuel reforming are explained first. The advantages and disadvantages are given for each reaction so that the reaction characteristics and issues to be overcome for each reaction are clarified.

Then, we consider desired performance of a fuel reformer by analyzing energy efficiency of the hydrogen system. Several components are introduced to compose a hydrogen system, and then electric efficiency of the hydrogen system is compared with the conventional power generation system using an internal combustion engine. The degree of feasibility and the

performance requirements of the fuel reformer in each scale system in terms of energy efficiency are indicated.

2.2 Reforming Reactions

In this thesis, we give attention to liquid fuels, especially to alcoholic fuels since they are chemically stable in normal pressure and temperature, which realize high energy density as a hydrogen carrier. In addition, alcoholic fuels are widely available in industry and can be derived from several resources such as natural gas, coal, and renewable biomass. In recent years, industrial production of alcohol from biomass resources is increasing. Bio-derived alcohol is receiving attention since it is so-called "carbon neutral," which has a significant potential as a fuel for a fuel reformer.

Among alcoholic fuels, methanol is chosen in this study since it is the most basic alcohol. The reaction characteristics of methanol can form the foundations of the reforming process of other alcoholic fuels. In addition, methanol has a relatively high reactivity and fairly low reaction temperature so that it is easy to handle and construct a simple fuel reformer.

In the following section, the methanol-based reactions involved in fuel reformers are explained in detail. The reaction characteristics and recent investigations on catalysts are included in the explanation.

2.2.1 Steam Reforming Reaction

Steam reforming (STR) is a reaction involving high temperature water vapor. Methanol STR is expressed as

$$\mathrm{CH_3OH + H_2O \rightarrow 3\,H_2 + CO_2} \qquad (\Delta H = +49.5\,\mathrm{kJ/mol}). \tag{R 2.1}$$

As seen in reaction (R 2.1), STR extracts hydrogen atoms not only from methanol, but also from supplied steam. Due to this additional source of hydrogen atoms, the concentration of hydrogen in the reforming gas reaches up to 75 % ideally. This high concentration characteristic enabled the STR reaction to be widely applied [5,6].

However, STR is a strongly endothermic reaction, and requires high temperature steam. Therefore, an external heat source and steam generator are needed to sustain the reaction. This causes the reactor of STR to become very complex including the steam generator, external heat source (catalytic combustor is often used), and fuel reformer. That is why STR is suitable for large-scale chemical plants or industrial use, where the thermal loss is not considerably large due to the scale merit.

Moreover, STR needs catalyst to sustain a reaction since the reaction speed is very slow. Metal oxide catalysts on the basis of Cu, Zn, Ni are often applied to the STR reactor [3,4]. The reaction temperature ranges from 500 K to 600 K depending on catalysts. In addition, STR is sensitive to the steam-carbon (S/C) ratio and reaction temperature, therefore, the operating condition must be precisely controlled. The deviation from the optimum operating condition may cause fatal catalyst degradation or soot deposition which drastically reduce the efficiency of the reforming reaction.

The start-up and response times of STR are also markedly long due to the slow reaction speed. This causes the designing limitation of the reactor to ensure long residence time from tens of milli-seconds to several seconds [7,8]. Since STR is a catalytic reaction, the composition, treatment procedure, and surface structure of the catalyst have great influences on the reaction performance. Thus, the optimum use and its treatment process of the catalysts are the primary concern for many researchers [9].

In a compact reactor of a sub-kW scale, the heat management to avoid a major thermal loss is a challenging issue. There are several papers which integrate STR reactors with a catalytic combustor as a heat source and achieve relatively high conversion and efficiency [6,10]. Also, some groups realized a micro-scale fuel reformer with an output of several-W for a mobile device, integrating a micro-channel reactor [11–13]. Although many researchers exploring the high-performance STR reactor, there are still numerous challenges to be overcome in designing and constructing a compact and inexpensive STR system.

2.2.2 Partial Oxidation Reaction

Partial oxidation (POX) is another process for obtaining H_2-rich gas. POX is a combustion reaction in a fuel-rich condition, therefore, it is also known as fuel-rich combustion.

The complete combustion reaction of methanol is written as

$$\mathrm{CH_3OH} + \frac{3}{2}\left(\mathrm{O_2} + 3.76\,\mathrm{N_2}\right) \rightarrow 2\,\mathrm{H_2O} + \mathrm{CO_2} + 5.64\,\mathrm{N_2} \qquad (\Delta H = -638.1\,\mathrm{kJ/mol}). \tag{R 2.2}$$

The equivalence ratio, ϕ, for reaction (R2.2) is defined as $\phi \equiv 1$. The stoichiometric reaction of methanol POX, on the other hand, is a reaction in a fuel-rich condition, $\phi_{\mathrm{st}} = 3$, and written as

$$\mathrm{CH_3OH} + \frac{1}{2}\left(\mathrm{O_2} + 3.76\,\mathrm{N_2}\right) \rightarrow 2\,\mathrm{H_2} + \mathrm{CO_2} + 1.88\,\mathrm{N_2} \qquad (\Delta H = -189.5\,\mathrm{kJ/mol}). \tag{R 2.3}$$

Comparing with STR, POX has several disadvantages regarding its reaction products. As shown in reaction (R 2.3), hydrogen atoms are derived only from the methanol molecule in the reactant. H_2 yield of POX is, therefore, lower than that of STR. In addition, when air is introduced as oxidizer, a dilution effect by N_2 causes the reduction of the H_2 concentration. Even if pure O_2 is supplied as oxidizer, the maximum H_2 concentration realized by POX is 47 %, while it reduces to 41 % when air is supplied.

Taking these disadvantages into account, one of the incentives of POX is that POX is exothermic so that the reaction speed is very fast than STR. The fast reaction of POX leads to a higher conversion ratio and quicker response time compared with STR. Also due to the exothermic nature of the reaction, an external heat source is not required in POX. These advantages regarding the exothermic nature of the reaction enable the POX fuel reformer to be relatively simple and thermally self-sustainable.

There are two types of POX reactions: catalytic and non-catalytic. First, catalytic POX

takes place in the presence of catalysts. Noble metal catalysts like Pt and Rh are reported to have high activity and selectivity to the H_2 production. Typical hydrogen selectivity of catalytic POX in the presence of a noble metal catalyst is 65–75 % with a conversion ratio of 90 % [14–16]. Using a Pd/ZnO catalyst, a conversion ratio is about 70 % and the H_2 selectivity is up to 96 % [17,18]. Much cheaper catalysts based on Cu or Cu-ZnO are also conventionally used, but its conversion and selectivity still need to be improved [19–22].

Since catalysts are prone to poisoning and require great care in operating conditions or the sulphur content of the fuel, non-catalytic POX is another promising candidate for a hydrogen production process. Non-catalytic POX enables the reforming system to be much simpler and easier for maintenance. However, without a catalyst, it is difficult to sustain the reaction within the reactor and achieve a high conversion ratio. One of the most promising techniques to stabilize POX within a reactor is to utilize a porous material. Many researchers explored POX of various fuels in a porous material [23]. Due to its non-catalytic feature, the composition yield reaches the chemical equilibrium when a long residence time is ensured. Therefore, non-catalytic POX produces a relatively large amount of CO, which has to be reduced in a treatment reactor based on CO purification reactions presented later [24,25].

2.2.3 Autothermal Reforming Reaction

Autothermal reforming (ATR) is a combination of the above two reactions, where both steam and O_2 are introduced with a fuel to the reactor. This reaction enables the reactor to gain both advantages of POX and STR. The reaction of ATR can be written as

$$\mathrm{CH_3OH} + \frac{1}{2}\zeta\,(\mathrm{O_2} + 3.76\,\mathrm{N_2}) + (1-\zeta)\,\mathrm{H_2O} \rightarrow \mathrm{CO_2} + (3-\zeta)\,\mathrm{H_2} + 1.88\zeta\,\mathrm{N_2}$$

$$(\Delta H = 49.5 - 239.0\zeta\,\mathrm{kJ/mol}), \quad (\mathrm{R}\,2.4)$$

where ζ represents the reaction ratio of POX. In this reaction, both steam and O_2 are supplied simultaneously to the reactor depending on ζ. When $\zeta = 0$, the resulting reaction is identical to STR, while $\zeta = 1$ corresponds to POX. The overall reaction can be,

therefore, both exothermic and endothermic depending on ζ. This characteristic enables the reaction to have a flexible heat release/absorb rate, thus it is possible to build a thermally self-sustainable system by controlling ζ so as to balance the exothermic and endothermic reactions.

Due to the STR characteristic, the reaction efficiency of ATR is greater than the simple POX reaction. Therefore, to make the best use of the flexibility of ATR, one can operate the ATR reactor in large ζ condition to utilize the fast reaction characteristic of POX in a start-up operation. And then, one can reduce ζ to keep the high production efficiency of H_2 in a steady operation. By controlling the overall reaction by ζ in this manner, it is possible to optimize the reaction start-up, response, and efficiency. Therefore, many researches and developments on ATR are proposed in the automobile industry where the reaction response characteristic is the primary concern [26–28].

2.2.4 CO Purification Reactions

When reforming gas produced by a fuel reformer is supplied to a fuel cell, the CO concentration in the reforming gas is a major concern. In high-temperature-type fuel cells like solid oxide fuel cell (SOFC) and molten carbonate fuel cell (MCFC), both H_2, CO, and even CH_4 can be used as a fuel. Therefore, these fuel cells can introduce POX as a reforming reaction which enables the system to have quick start-up and response characteristics. However, in low-temperature-type fuel cells, such as polymer electrolyte fuel cell (PEFC) and phosphoric acid fuel cell (PAFC), CO gas causes poisoning of cell electrodes even in a small amount. Therefore, for such systems, the reforming gas is required to contain CO less than 1 % for PAFC, and less than 100 ppm for PEFC. To reduce the amount of CO in the reforming gas, a CO purification reactor is required in the downstream of the fuel reformer.

Water-gas shift (WGS) reaction is commonly used for preliminary purification of CO.

WGS can reduce the concentration of CO to about 1 %. The WGS reaction is expressed as

$$\mathrm{CO} + \mathrm{H_2O} \rightleftharpoons \mathrm{CO_2} + \mathrm{H_2} \qquad (\Delta H = -41.0\,\mathrm{kJ/mol}). \tag{R 2.5}$$

Because of the moderately exothermic characteristic, the WGS reaction is very sensitive to the reaction temperature. The chemical equilibrium of the reaction has a tendency to shift to the product side at a lower reaction temperature (and vice versa). Therefore, the WGS reactor is favorable to operate at a lower temperature to achieve an efficient reduction of CO and production of H_2. However, the lower the reaction temperature is, the slower the reaction speed becomes. A catalyst is, therefore, necessary for the WGS reactor to lower the activation energy of the reaction. Cu-Zn or Fe-Cr-based catalysts are often used for the WGS reaction and a high conversion ratio of CO in a low temperature condition (470–550 K) is realized [29].

The fuel cells operating in a very low temperature such as PEFC (about 350 K) needs more purification of CO. For example, the platinum electrodes of PEFC are considerably sensitive to the presence of CO, so that the CO concentration must be reduced to less than 100 ppm. To realize such a low CO concentration, additional CO purification by preferential CO oxidation needs to be introduced. The preferential CO oxidation reaction is expressed as

$$\mathrm{CO} + \frac{1}{2}\,\mathrm{O_2} \rightarrow \mathrm{CO_2}. \tag{R 2.6}$$

This oxidation reaction of CO in the presence of H_2 should take place between the outlet temperature of the WGS reactor and inlet temperature of the fuel cell ($\sim$ 350 K for PEFC). Many kinds of catalysts are investigated by researchers based on noble metals such as Pt, Ru, Pd, and Au [5,30–32].

2.3 Requirements of the Reforming Efficiency

In a hydrogen system, the combination of energy devices (fuel reformer, fuel cell, and other related components) determines the overall efficiency of the system. In this section, therefore, the efficiency of each components are considered and the requirement of the reforming efficiency of the fuel reformer is discussed.

We concern a fuel reforming system to supply H_2-rich gas for fuel cells by methanol non-catalytic POX in this thesis. As mentioned in the previous section, the non-catalytic POX reaction produces relatively high concentration of CO in the reforming gas ($\sim 15\,\%$). Therefore, when using low-temperature-type fuel cells like PEFC, the reforming gas needs post-treatment (WGS and preferential CO oxidation) to reduce CO concentration less than 100 ppm. On the other hand, the reforming gas of POX can be directly supplied as syngas (CO + H_2) to fuel cells like SOFC when the operating temperature is high enough to consume CO as a fuel. In this section, we pick up SOFC and PEFC as representatives of fuel cells, operating in high-temperature and low-temperature conditions, respectively.

SOFC is operated under high temperature ($\sim 1200\,\mathrm{K}$), therefore, it is often applied to a relatively large scale power supply (MW-class) system [33,34]. However, the miniaturization of the SOFC system has been seen these days. A small-scale system of SOFC for home-use (several-kW-class) has been developed recently. The maximum electrical efficiency of the home-use SOFC system is reported up to 45 % (HHV-basis). In addition, due to its high temperature operation, the exhaust gas still possesses relatively large amount of sensible heat, which can be utilized by constructing a combined cycle or a co-generation system. The total thermal efficiency can expected to be up to 85 % [33].

PEFC, on the other hand, operating at a lower temperature ($\sim 400\,\mathrm{K}$), is generally used as a power generation system for several-kW to up to 100-kW-class systems. However, PEFC has lower electric efficiency compared with SOFC. The electric efficiency of PEFC is reported to be 30–40 % [35].

Considering the total system as power generation, it has a significant meaning to

compare the total efficiency of a fuel reformer and fuel cell system (FR-FC system) with that using an internal combustion engine (ICE system). Therefore, in the following, both FR-FC and ICE systems fueled by methanol are considered and the requirements of the fuel reformer to achieve a competitive electric efficiency are calculated.

It is well known that the electric efficiency of ICE is greatly affected by its operation scale (called scale effect). A scale effect is a tendency that the thermal efficiency of the system becomes higher with the scale-up of the system. This tendency is related to the thermal loss of the system which becomes relatively small when the scale of the system is large. When methanol is directly combusted as a fuel of ICE, the electric efficiency of ICE, therefore, depends on the scale of the system. When ICE is less than 1-kW-class, the efficiency of ICE is about 8 %. While the efficiency increases to 30 % when the scale becomes 100 kW [36]. Thus, ICE is not favorable in a relatively small scale system ($\sim$ 1 kW). ICE also has poor efficiency in a partial load condition which also becomes an issue in a small scale power generation system.

Figure 2.1 shows the efficiency requirements of the fuel reformer in both large and small scale systems. The requirements are calculated by comparing the total efficiency of the hydrogen systems with that of ICE. When the scale is relatively large ($\sim$ 100 kW), the efficiency of ICE becomes large (30 %) due to the scale effect. Therefore, even if SOFC can achieve 50 % of electric efficiency, the fuel reformer needs efficiency of more than 60 % to exceed the ICE system in this scale.

On the other hand, when the scale of the system is relatively small ($\sim$ 1 kW), the efficiency of ICE drastically deteriorates to 8 %, while the fuel cell does not experience such a deterioration. For example, PEFC system can achieve 45 % electric efficiency in this scale. The requirement of the fuel reformer is, therefore, 20 % in order to achieve comparable efficiency to the ICE system.

In this manner, the conventional ICE system is exposed to a scale effect by which the efficiency is drastically deteriorated in a smaller scale system. Hence, a FR-FC system has an advantage in a relatively small scale system. In a large scale system, on the other

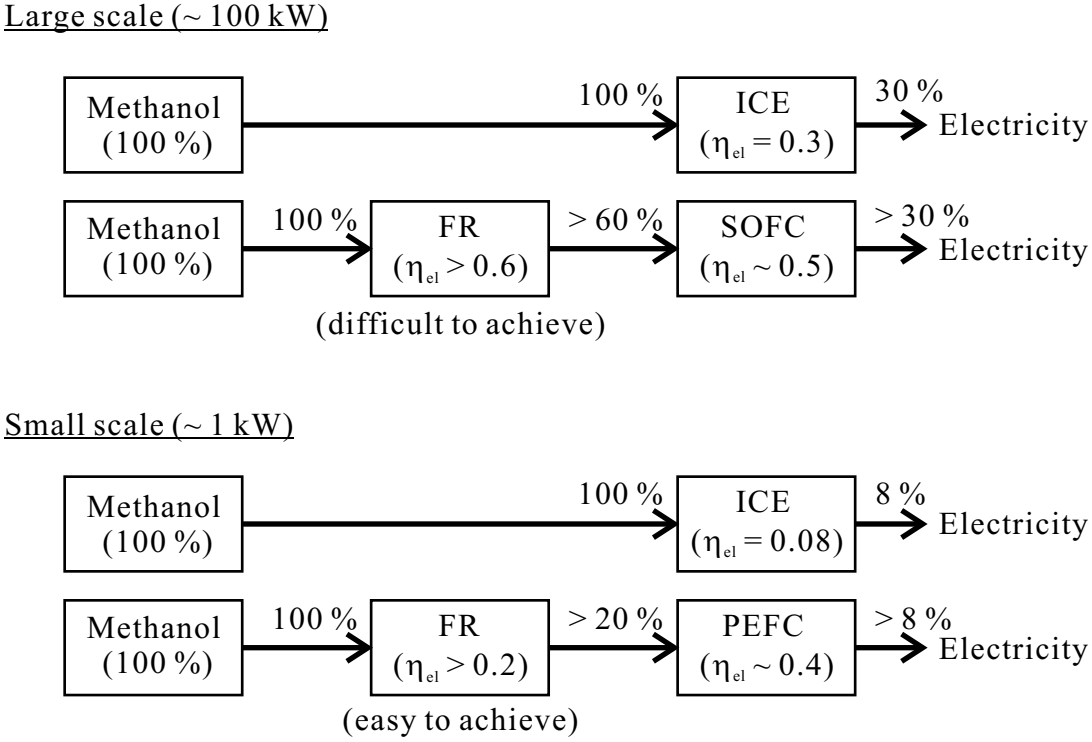

Figure 2.1: Comparison between ICE system and FR-FC system.

hand, a fuel reformer needs more than 60 % efficiency to achieve a competitive system with ICE. Therefore, a high-efficiency fuel reformer using catalysts are required in a large scale system.

The requirement of the fuel reformer for a hydrogen system is much lower in a small scale system. Therefore, non-catalytic POX having relatively lower efficiency than STR can still be applied to the small-scale system thanks to the advantageous feature of fuel cells in a small scale.

Also in a smaller scale system, thermal management is an important issue since the thermal loss of the system has great effects on the total reforming characteristics. Therefore, in the present thesis, we consider the optimization of the fuel reformer by thermal management without introducing catalysts. This thermal management procedure and its knowledge of the reaction characteristics can also be applied to the fuel reformers using catalysts since the reaction location and its thermal effects are also crucial to the catalytic

reaction and overall efficiency of the fuel reformer.

2.4 Summary

In this chapter, the basic reactions related to fuel reformers are introduced. There are three major reactions involved in fuel reforming: steam reforming (STR), partial oxidation (POX), and autothermal reforming (ATR). Also as post-treatment reactions, water-gas shift (WGS) and preferential CO oxidation are explained. We explored these basic reactions in terms of reaction characteristics including exothermic/endothermic manners, reaction temperature levels, reaction speeds, and catalytic characteristics.

STR is a catalyst-based endothermic reaction, which is suitable for relatively large scale hydrogen production, since it needs an external heat source and the reaction is fairly slow. Many researchers investigated in the optimum use of the catalysts, generally based on Cu, Zn and their oxides.

POX is an exothermic reaction which enables the system to be simple and compact. In the case of catalytic POX, noble catalysts are needed to operate a high conversion ratio. Catalysts like Cu and Zn are also used for catalytic POX but still needs improvement for a higher conversion ratio. In the case of non-catalytic POX, on the other hand, the crucial issue is the stability of the reaction. Many researchers work on the stabilization of the reaction, especially by using porous materials.

In the latter part of this chapter, efficiency requirements of the fuel reformer as a part of a hydrogen system are calculated. A fuel reformer and fuel cell (FR-FC) system is considered in both large and small scale cases. By comparing the FR-FC system with a system with an internal combustion engine (ICE), the following results were obtained:

- The efficiency required for the fuel reformer in a large scale case is up to 60 %. While that in a small scale case is as low as 20 %.

- In the system using an internal combustion engine, the bottleneck of the total electric efficiency is the efficiency of ICE, which reduces drastically in a small scale system.

- The efficiency requirement of fuel reformer is not so much severe in the case of small

scale system. This is due to the advantage of a fuel cell which is not so much affected by its operation scale.

- FR-FC system is more advantageous in a smaller scale system.

Bibliography

[1] Marbán, G., and Valdés-Solís, T., "Towards the Hydrogen Economy?", *International Journal of Hydrogen Energy*, Vol. 32 (2007), pp. 1625–1637.

[2] Tamagnini, P., Axelsson, R., Lindberg, P., Oxelfelt, F., Wünschiers, R., and Lindblad, P., "Hydrogenases and Hydrogen Metabolism of Cyanobacteria", *Microbiology and Molecular Reviews*, Vol. 66, No. 1 (2002), pp. 1–20.

[3] de Wild, P. J., and Verhaak, M. J. F. M., "Catalytic Production of Hydrogen from Methanol", *Catalysis Today*, Vol. 60 (2000), pp. 3–10.

[4] Choi, Y., and Stenger, H. G., "Kinetics, Simulation And Optimization of Methanol Steam Reformer for Fuel Cell Applications", *Journal of Power Sources*, Vol. 142, (2005), pp. 81–91.

[5] Takeda, K., Baba, A., Hishinuma, Y., and Chikahisa, T., "Performance of A Methanol Reforming System for A Fuel Cell Powered Vehicle and System Evaluation of A PEFC System", *JSAE Review*, Vol. 23, No. 2 (2002), pp. 183–188.

[6] Emonts, B., B-Hansen, J., J, S.L., Höhlein, B., and Peters, R., "Compact Methanol Reformer Test for Fuel-Cell Powered Light-Duty Vehicles", *Journal of Power Sources*, Vol. 71, No. 1–2 (1998), pp. 288–293.

[7] Iwasa, N., Kudo, S., Takahashi, H., Masuda, S., and Takezawa, N., "Highly Selective Supported Pd Catalysts for Steam Reforming of Methanol", *Catalysis Letters*, Vol. 19 (1993), pp. 211–216.

[8] Jiang, C. J., Trimm, D. L., and Wainwright, M. S., "Kinetic Study of Steam Reforming of Methanol over Copper-Based Catalysts", *Applied Catalysis A: General*, Vol. 93 (1993), pp. 245–255.

[9] Ghenciu, A.F., "Review of Fuel Processing Catalysts for Hydrogen Production in PEM Fuel Cell System", *Current Opinion in Solid State and Materials Science*, Vol. 6 (2002), pp. 389–399.

[10] Höhlein, B., Boe, M., B-Hansen, J., Bröckerhoff, P., Colsman, G., Emonts, B., Menzer, R., and Riedel, E. "Hydrogen from Methanol for Fuel Cells in Mobile Systems: Development of A Compact Reformer", *Journal of Power Sources*, Vol. 61, (1996), pp. 143–147.

[11] Yoshida, K., Tanaka, S., Hiraki, H., and Esashi, M., "A Micro Fuel Reformer Integrated with A Combustor And A Microchannel Evaporator", *Journal of Micromechanics and Microengineering*, Vol. 16, No. 9 (2006), pp. S191–S197.

[12] Kundu, A., Park, J. M., Ahn, J. E., Park, S. S., Shul, Y. G., and Han, H. S., "Micro-Channel Reactor for Steam Reforming of Methanol", *Fuel*, Vol. 86, No. 9 (2007), pp. 1331–1336.

[13] Holladay, J. D., Jones, E. O., Dagle, R. A., Xia, G. G., Cao, C., and Wang, Y., "High Efficiency And Low Carbon Monoxide Micro-Scale Methanol Processors", *Journal of Power Sources*, Vol. 131, (2004), pp. 69–72.

[14] Traxel, B. E. and K. L. Hohn. "Partial Oxidation of Methanol at Millisecond Contact Times", *Applied Catalysis A: General*, Vol. 244, No. 1 (2003), pp. 129–140.

[15] Cao, C., Hohn, K. L., "Study of Reaction Intermediates of Methanol Decomposition And Catalytic Partial Oxidation on Pt/Al_2O_3", *Applied Catalysis A: General*, Vol. 354 (2009), pp. 26–32.

[16] Wanat, E. C., Suman, B., and Schmidt L. D., "Partial Oxidation of Alcohols to Produce Hydrogen And Chemicals in Millisecond-Contact Time Reactors", *Journal of Catalysis*, Vol. 235 (2005), pp. 18–27.

[17] Cubeiro, M. L., and Fierro, J. L. G., "Partial Oxidation of Methanol over Supported Palladium Catalysts", *Applied Catalysis A: General*, Vol. 168, No. 2 (1998), pp. 307–322.

[18] Cubeiro, M. L., and Fierro, J. L. G., "Selective Production of Hydrogen by Partial Oxidation of Methanol Over ZnO-Supported Palladium Catalysts", *Journal of Catalysis*, Vol. 179, No. 1 (1998), pp. 150-162.

[19] Huang, T. J., and Chren, S. L., "Kinetics of Partial Oxidation of Methanol Over a Copper-Zinc Catalyst", *Applied Catalysis*, Vol. 40 (1988), pp. 43–52.

[20] Huang, T. J., and Wang, S. W., "Hydrogen Production via Partial Oxidation of Methanol over Copper-Zinc Catalysts", *Applied Catalysis* Vol. 24, No. 1–2 (1986), pp. 287–297.

[21] Alejo, L., Lago, R., Peña, M. A., and Fierro, J. L. G., "Partial Oxidation of Methanol to Produce Hydrogen Over Cu-Zn-Based Catalysts", *Applied Catalysis A: General*, Vol. 162, No. 1–2 (1997), pp. 281–297.

[22] Chen, W. S., Chang, F. W., Roselin, L. S., Ou, T. C., and Lai, S. C., "Partial Oxidation of Methanol Over Copper Catalysts Supported on Rice Husk Ash", *Journal of Molecular Catalysis A: Chemical*, Vol. 318, No. 1–2 (2010), pp. 36–43.

[23] Al-Hamamre, Z., Voß, S., and Trimis, D., "Hydrogen Production by Thermal Partial Oxidation of Hydrocarbon Fuels in Porous Media Based Reformer", *International Journal of Hydrogen Energy*, Vol. 34 (2009), pp. 827–832.

[24] Horng, R., Chou, H., Lee, C., and Tsai, H. "Characteristics of Hydrogen Produced by Partial Oxidation and Auto-Thermal Reforming in A Small Methanol Reformer", *Journal of Power Sources*, Vol. 161 (2006), pp. 1225–1233.

[25] Silva, A. M., Farias, A. M. D., Costa, L. O. O., Barandas, A. P. M. G., Mattos, L. V., Fraga, M. A., and Noronha, F. B. "Partial Oxidation and Water-Gas Shift Reaction in

An Integrated System for Hydrogen Production from Ethanol", *Applied Catalysis A: General*, Vol. 334 (2008), pp. 179–186.

[26] Lindström, B., and Pettersson, L. J., "Development of A Methanol Fuelled Reformer for Fuel Cell Applications", *Journal of Power Sources*, Vol. 118 (2003), pp. 71–78.

[27] Taki, M., Negishi, Y., and Kobayashi, N., "Development of Highly-Efficient Compact Methanol Fuel Reformer for Fuel Cells", *TOYOTA Technical Review*, Vol. 47, No. 2 (1997), pp. 76–81 (in Japanese).

[28] Patel, S., and Pant, K. K., "Kinetic Modeling of Oxidative Steam Reforming of Methanol over $Cu/ZnO/CeO_2/Al_2O_3$ Catalyst", *Applied Catalysis A: General*, Vol. 356 (2009), pp. 189–200.

[29] Rhodes, C., Hutchings, G. J., and Ward, A. M., "Water-Gas Shift Reaction: Finding the Mechanistic Boundary", *Catalysis Today*, Vol. 23 (1995), pp. 43–58.

[30] Liu, X., Korotkikh, O., and Farrauto, R., "Selective Catalytic Oxidation of CO in H_2: Structural Study of Fe Oxide-Promoted Pt/Alumina Catalyst", *Applied Catalysis A: General*, Vol. 226 (2002), pp. 293–303.

[31] Kahlich, M. J., Gasteiger, H. A., and Behm, R. J., "Kinetics of the Selective CO Oxidation in H_2-Rich Gas on Pt/Al_2O_3", *Journal of Catalysis*, Vol. 171, No. 1 (1997), pp. 93–105.

[32] Schubert, M. M., Kahlich, M. J, Gasteiger, H. A., and Behm, R. J., "Correlation between CO Surface Coverage and Selectivity/Kinetics for the Preferential CO Oxidation over Pt/γ-Al_2O_3 and Au/α-Fe_2O_3: an In-Situ DRIFTS Study", *Journal of Power Sources*, Vol. 84, No. 2 (1999), pp. 175–182.

[33] Zhang, X., Chan, S. H., Li, G., Ho, H. K., Li, J., and Feng, Z., "A Review of Integration Strategies for Solid Oxide Fuel Cells", *Journal of Power Sources*, Vol. 195, No. 3 (2010), pp. 685–702.

[34] Dokiya, M., "SOFC System and Technology", *Solid State Ionics*, Vol. 152–153, (2002), pp. 383–392.

[35] NISTEP MEXT (Ed.), *Technical Front of Hydrogen Energy*, (2003), p. 32, Kogyo Chosakai Publishing Co. Ltd. (in Japanese).

[36] Delsman, E. R., Uju, C. U., de Croon, M. H. J. M., Schouten, J. C., and Ptasinski, K.J., "Exergy Analysis of An Integrated Fuel Processor and Fuel Cell (FP-FC) System", *Energy*, Vol. 31, No. 15 (2006), pp. 3300–3309.

Chapter 3

Reaction Characteristics of Methanol Partial Oxidation

3.1 Introduction

Since the process of the fuel reforming determines the overall efficiency of the hydrogen energy system, it is important to understand and obtain knowledge on the reaction characteristics of the fuel reforming reaction. In this chapter, therefore, we investigate the basic characteristics of the non-catalytic methanol partial oxidation (POX) reaction.

As is often the case with combustion, the reaction temperature is the primary concern in designing a reactor. In the same way, the fuel reforming reaction to obtain hydrogen from a hydrocarbon fuel is sensitive to the reaction temperature [1,2]. Therefore, we consider the temperature distributions and energy flows in the reactor and their influences on the reaction in order to obtain reactor designing principle.

First, in order to estimate the reforming characteristics and performance, the chemical equilibrium compositions and adiabatic flame temperatures were calculated. By these results, it is possible to evaluate if the size and configuration of the reactor are appropriate to attain a chemical equilibrium and adiabatic reaction. Also, the results can show how the change of the operating condition affects the product gas components and reformer performance, which is helpful for the discussion.

The reactor was constructed as simply as possible, but also considering the practical use in the engineering perspective. The reformer was, therefore, composed of a stainless steel pipe as the reactor exterior, and a ceramic honeycomb was inserted in the reactor as a flame stabilizer. The POX reaction, mentioned in the previous chapter and also known as fuel-rich combustion, is normally unstable due to its fuel-rich condition so that the reactor needs a flame stabilizer to obtain a stable reaction. By the thermal effects of the ceramic honeycomb, the reaction was stabilized on the surface of the ceramic honeycomb under a wide range of equivalence ratio beyond the flammable limit. As the initial step of evaluating the reforming reaction, the experiments were conducted without the catalyst, by which catalytic effects can be separated from those of thermal effects.

The effects of mixture component and reaction temperature on the reforming characteristics were also discussed, using detailed temperature distributions within the reactor and reactor exterior. Those results were related to the reforming gas components and evaluated by several parameters: methanol conversion ratio, hydrogen production ratio, and preferential production ratios.

3.2 Experimental Apparatus and Conditions

3.2.1 Reforming System

Figure 3.1 shows the overview of the reforming system. The room air was pressurized to about 0.8 MPa by the air compressor and stored in a surge tank. The pressure of the air was then reduced to 0.3 MPa by pressure regulators and the air was supplied both to the fuel and air supply paths. Liquid methanol as a fuel was stored in a fuel tank and pressurized from the upper port by the pressurized air. This enabled the fuel to be pumped to the injector with an electric valve and injected to the evaporator as spray. The air supplied to the air supply port was also introduced to the evaporator as oxidizer in an atmospheric pressure. The air flow rate was adjusted to the desired value by a mass flow controller. Supplied air and fuel formed a mixture in the evaporator and was introduced to the reactor. The reaction took place in the reactor, then the reforming gas was sampled from the most

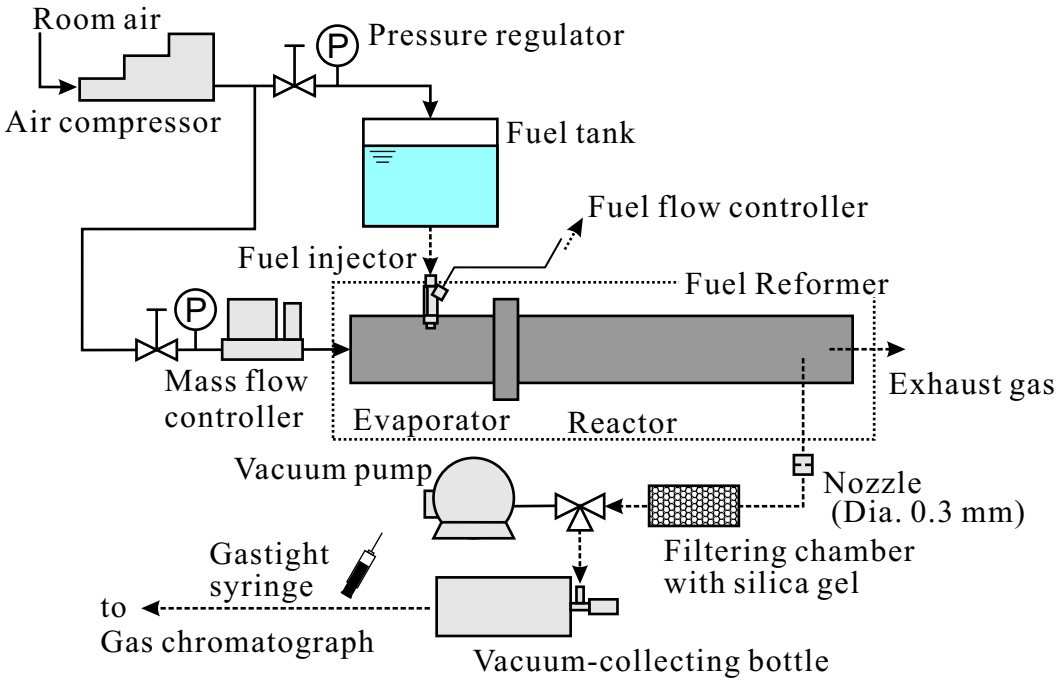

Figure 3.1: Schematic overview of the fuel reformer system.

downstream part of the reactor. The gas sampling was conducted by a vacuum bottle connected to the gas sampling probe having a 0.3 mm nozzle and silica gel packed column, which froze the gaseous reactions and removed unreacted fuel and generated water vapor.

3.2.2 Fuel Reformer

Figure 3.2 illustrates the schematic and cross-sectional views of the reformer. As shown in the figure, the reformer was composed of two parts, i.e., the evaporator and the reactor. The evaporator was made of a stainless steel pipe with inner diameter and length of 28 mm and 200 mm, respectively. A fuel injection port was located on the wall surface of the evaporator, on which an injector with an electric valve was mounted. A rectangular electric signal was sent from a function generator (Yokogawa; WE500, WE7281) to the injector to control the valve timing and opening duration. A flow rate of liquid fuel spray was, therefore, controlled by adjusting the frequency and duty ratio of the electric signal. In this experiment, the frequency and duty ratio were set to 20 Hz and 4.3 %, respectively.

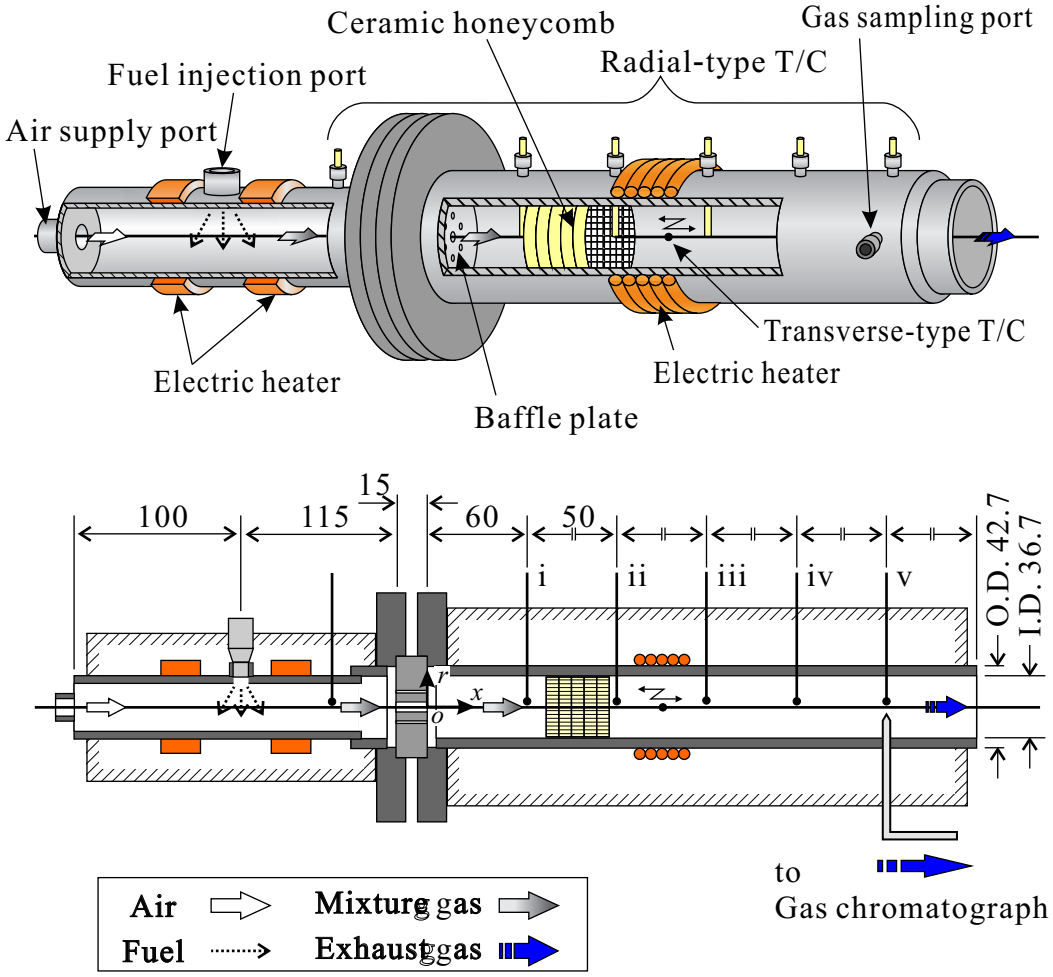

Figure 3.2: Schematic view of the fuel reformer (evaporator and reactor, unit: mm).

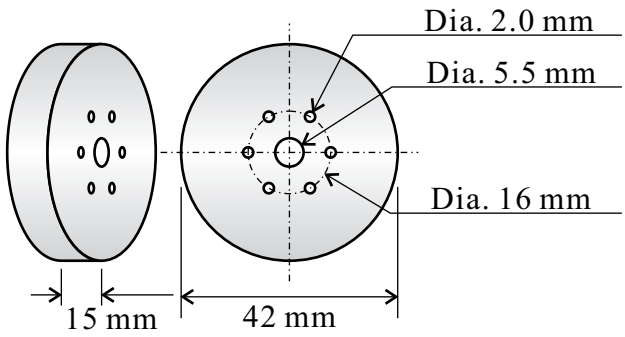

Figure 3.3: Baffle plate.

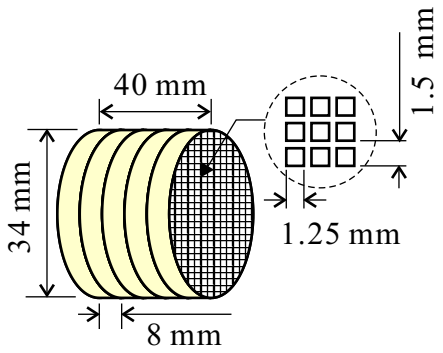

Figure 3.4: Ceramic honeycomb.

This setting condition represents the fuel flow rate $\dot{V}_{\text{fuel}} = 5.56\,\text{mL(liq.)/min}$. An air supply port was set at the uppermost end of the evaporator. Air supply rate was controlled by a mass flow controller (Yamatake; MQV0020). At the upstream and downstream locations adjacent to the fuel supply port, electric band heaters (Sakaguchi E.H. Voc.; BH3430) were placed and wrapped around the evaporator. These heaters were connected to a variable autotransformer (Yamabishi; V-130-3) and the electric power loads were controlled to keep the temperature inside the evaporator at 420 K during the experiment. The fuel spray impinged on the inner wall of the evaporator was, therefore, vaporized instantaneously. The vaporized fuel joining the air flowing from the upstream air supply port was then supplied to the reactor through a baffle plate.

Between the evaporator and reactor, there was a baffle plate shown in Fig. 3.3 connecting these two parts. Multiple holes were drilled in the 15 mm-thick stainless steel disk, i.e., a 5.5 mm hole was located at the center of the disk and six holes with 2.0 mm in diameter surrounded the center one. This multi-hole baffle plate was expected to enhance the mixing of the methanol vapor and air, and also to prevent backfiring from the reactor to the evaporator.

The reactor was made of a stainless steel pipe $D = 36.7\,\text{mm}$ in inner diameter and 300 mm in length. The origin of the x–r coordinate system was set at the center of the downstream surface of the baffle plate. In the reactor, a ceramic honeycomb shown in Fig. 3.4 was inserted in the upstream region of the reactor, $1.74 \leq x/D \leq 2.83$. Detailed

Table 3.1: Material characteristics of ceramic honeycomb.

Material	Cordierite
Composition	2 MgO_2· Al_2O_3· 5 SiO_2
Cell [cell/in^2]	300

configuration and the purpose of the ceramic honeycomb will be explained later.

Another electric band heater (Watlow; MB01E1AB3005) was twined around the reactor wall at the location $3.1 \leq x/D \leq 4.3$. This electric heater was powered by a variable autotransformer in the same way as those in the evaporator.

To avoid undesired heat loss to the environment, the fuel reformer was wrapped by heat insulator with a thickness of 40 mm.

3.2.3 Ceramic Honeycomb

A cylindrical ceramic honeycomb with 34 mm in diameter was inserted into the reactor in order to stabilize the POX reaction. The dimensions and material characteristics of the ceramic honeycomb are shown in Fig. 3.4 and Table 3.1, respectively. The ceramic honeycomb was made of cordierite ceramic, having a cell density of 300 cells per square inch. The hydraulic diameter of a unit square cell was 1.25 mm and the fraction of the open frontal area was 69%. A single piece of the ceramic honeycomb was 8 mm-thick, and five pieces of them were glued together with fireproof cement to create a 40 mm-long stack. This ceramic honeycomb, called Honeycomb A, was inserted in the region $1.74 \leq x/D \leq 2.83$ to serve as a flame stabilizer.

In the present reactor, a POX reaction could not be sustained for any fuel-rich conditions if a ceramic honeycomb was not inserted in the reactor. Therefore, the basic reaction characteristics in the reactor using a ceramic honeycomb were investigated first and we clarify the role of the ceramic honeycomb in the following discussion.

Table 3.2: The coordinates of the radial-type thermocouples.

Position	i	ii	iii	iv	v
x [mm]	60	110	160	210	260
x/D	1.6	3.0	4.4	5.7	7.1

3.2.4 Measuring Methods

Temperature Measurement

In order to measure gas temperatures, two kinds of temperature probes were fabricated: radial-type and transverse-type probes. The radial-type probe was composed of a pair of 0.1 mm K-type thermocouple wires and a two-holed ceramic tube with an outer diameter of 3 mm. This probe was inserted through the holes on the sidewall of the fuel reformer (one in the evaporator and five in the reactor), enabling the six local gas temperatures to be measured simultaneously during experiments. The positions of the radial-type probes inserted in the reactor are named as Position i to Position v, and these coordinates are shown in Table 3.2.

The transverse-type probe, on the other hand, was composed of a pair of 0.1 mm K-type thermocouple wires inserted from the uppermost port of the evaporator and stretched along the center axis of the reformer. By using the transverse-type probe, it was possible to measure detailed gas temperature distributions along the center axis of the reactor.

In addition to the gas temperatures, the outer wall surface temperatures were also measured. This was done by the same 0.1 mm K-type thermocouples attached on the reactor surface. The positions of the wall-attached thermocouples correspond to those of radial-type probes shown in Table 3.2.

All of the welded junctions of the thermocouples were coated with silica particles to prevent the probe from being degraded and acting as a catalyst for the reaction. The sampling rate and the accuracy of the temperature measurement were 1 Hz and ± 1 K,

Table 3.3: Air flow rate ($\dot{V}_{\mathrm{fuel}} = 5.56\,\mathrm{mL(liq.)/min}$).

ϕ	$\dot{V}_{\mathrm{air}}$ [L/min]
3.0	7.65
3.5	6.56
4.0	5.74
4.5	5.10

respectively.

Gas Component Analysis

Gas sampling for gas component analysis was conducted by inserting a sampling probe at Position v ($x/D = 7.1$). The probe was made of a stainless steel tube, 3 mm in outer diameter, to which a 0.3 mm nozzle was applied in order to freeze the gaseous reaction. The position of the tip end of the probe was set at the reactor centerline, and the gas was sampled by connecting the tube to a vacuum-collecting bottle. Sample gas was then supplied to gas chromatograph (Shimadzu; GC-8A) through a filtering chamber packed with silica gel, by which water vapor and unreacted methanol were removed from the sample gas. A component detector on the basis of TCD (Thermal Conductivity Detector) method was applied to the gas chromatography. The column (Shinwa chem.; Shincarbon ST) mounted in the chromatograph oven was calibrated on the basis of external standard method for H_2, N_2, O_2, CO, and CO_2 gases. Argon gas was used as the carrier gas.

3.2.5 Experimental Conditions

In this study, we investigate how the ceramic honeycomb influences on the reforming reaction. Table 3.3 shows the flow rate conditions of reactants. Fuel and air were both introduced to the evaporator and supplied to the reactor through the baffle plate. $\dot{V}_{\mathrm{air}}$ and $\dot{V}_{\mathrm{fuel}}$ are the volume flow rates of the air and fuel fed to the evaporator, respectively. Note that $\dot{V}_{\mathrm{fuel}}$ represents the volume flow rate of the fuel in a liquid state. Equivalence ratio, ϕ,

is defined based on the complete combustion reaction. The stoichiometric equivalence ratio of POX is, therefore, $\phi_{st} = 3$ as mentioned in the previous chapter. As shown in Table 3.3, $\dot{V}_{fuel}$ was fixed to a specified condition in this chapter, and $\dot{V}_{air}$ was varied in the range of $3.0 \leq \phi \leq 4.5$.

The procedure applied in the experiment is described as follows:
The evaporator and reactor pipes were first heated up by the electric band heaters so that the reaction started smoothly. The preheating temperatures of the evaporator and reactor were 470 K and 820 K, respectively. Then, the heaters attached to the reactor were turned off and the fuel and air were supplied to the reformer. This heaters of reactor is only for the start-up of the reaction. Once the reaction starts, therefore, the reaction sustains by itself even though the heaters of the reactor have been switched off. Note that the heaters of the evaporator continued to be powered during the experiment and the temperature inside the evaporator was kept at about 420 K.

3.3 Fuel Reformer Evaluation Parameters

To evaluate the efficiency of the fuel reformer, one of the most significant parameters is the gas concentration of each species in the reforming gas. The gas concentrations of the sample gas are analyzed by gas chromatograph, the procedure to convert the sample gas concentration to the reforming gas concentration is presented in this section. Moreover, another evaluation parameters are presented by which the effects of the unreacted methanol and the dilution by N_2 in air are removed.

In the following discussion, the parameter M and Y denote the molar flow rate and gas concentration, respectively. On the other hand, the subscripts "u", "r", and "s" correspond to the unreacted gas, reforming gas, and sample gas, respectively.

In the present apparatus, the reforming gas was collected from the reactor and dried by the filtering chamber with silica gel. By this filtering chamber, unreacted methanol and produced water are removed from the reforming gas. Thus, the dry-based sampling gas is analyzed by gas chromatograph. The actual flow rate of each species in the reforming

gas, therefore, needs to be estimated on the basis of N_2 flow rate, which is assumed to be unchanged during the reaction and gas sampling process.

The molar flow rate of N_2 in the unreacted gas, $M_{\mathrm{u,N2}}$, can be calculated from the air flow rate determined by the experimental condition and N_2 concentration in the atmosphere (21 %). Since the chemical reactions involving N_2 molecule are assumed to be absent in the reactor, the molar flow rate of N_2 in the reforming gas is identical to that in the unreacted gas as

$$M_{\mathrm{u,N2}} = M_{\mathrm{r,N2}}. \tag{3.1}$$

The molar flow rate of species X in the reforming gas, $M_{\mathrm{r},X}$, is, therefore, calculated from the gas analysis result as

$$M_{\mathrm{r},X} = \frac{Y_{\mathrm{s},X}}{Y_{\mathrm{s,N2}}} \times M_{\mathrm{r,N2}} \qquad (X = \mathrm{H_2}, \mathrm{O_2}, \mathrm{CO}, \text{ and } \mathrm{CO_2}). \tag{3.2}$$

Since the summation of the analyzed gas concentrations, $\sum Y_{\mathrm{s},X}$ (X = H_2, O_2, N_2, CO, and CO_2), was 100 ± 2 % and no soot formation was visually observed during experiments, major components of the reforming gas was assumed to be these five species plus H_2O and unreacted methanol that were collected by the filtering chamber. Therefore, when paying attention to the carbon atoms, the components possessing carbon atoms among the products are only CO, CO_2, and unreacted methanol. The conservation of the number of carbon atoms provide the following relation:

$$M_{\mathrm{u,CH3OH}} = M_{\mathrm{r,CH3OH}} + M_{\mathrm{r,CO}} + M_{\mathrm{r,CO2}}. \tag{3.3}$$

The value of $M_{\mathrm{r,CH3OH}}$ can be calculated indirectly by using the above equation, which reveals the amount of consumed methanol in the reactor. The ratio of the consumed methanol to the supplied methanol, which we call methanol conversion ratio, α, is defined

as follows:

$$\alpha \equiv \frac{M_{\mathrm{u,CH3OH}} - M_{\mathrm{r,CH3OH}}}{M_{\mathrm{u,CH3OH}}} = \frac{M_{\mathrm{r,CO}} + M_{\mathrm{r,CO2}}}{M_{\mathrm{u,CH3OH}}} \tag{3.4}$$

The conservation of atoms regarding hydrogen, on the other hand, can introduce the relation:

$$4M_{\mathrm{u,CH3OH}} = 4M_{\mathrm{r,CH3OH}} + 2M_{\mathrm{r,H2}} + 2M_{\mathrm{r,H2O}}. \tag{3.5}$$

This equation discloses the value of $M_{\mathrm{r,H2O}}$ which is not directly available due to the filtering chamber.

Next, to evaluate the reforming gas components in relation to the supplied methanol, the production rate of species X, ξ_X, is defined as follows:

$$\xi_X \equiv \frac{M_{\mathrm{r},X}}{M_{\mathrm{u,CH3OH}}}. \tag{3.6}$$

The parameters ξ_{H2} and ξ_{CO} indicate the amount of H_2 and CO production, however, it is better to consider the traces of reacted methanol for the closer look of the reforming reaction. The parameter representing the preferential production rate of H_2, β, and that of CO, γ, are defined as follows, respectively:

$$\beta \equiv \frac{M_{\mathrm{r,H2}}}{M_{\mathrm{r,H2}} + M_{\mathrm{r,H2O}}}, \tag{3.7}$$

$$\gamma \equiv \frac{M_{\mathrm{r,CO}}}{M_{\mathrm{r,CO}} + M_{\mathrm{r,CO2}}}. \tag{3.8}$$

The above procedure for the calculation of the fuel reformer evaluation parameters are summarized in Fig. 3.5.

Finally, by using the above parameters, the resulting reaction taking place in the fuel

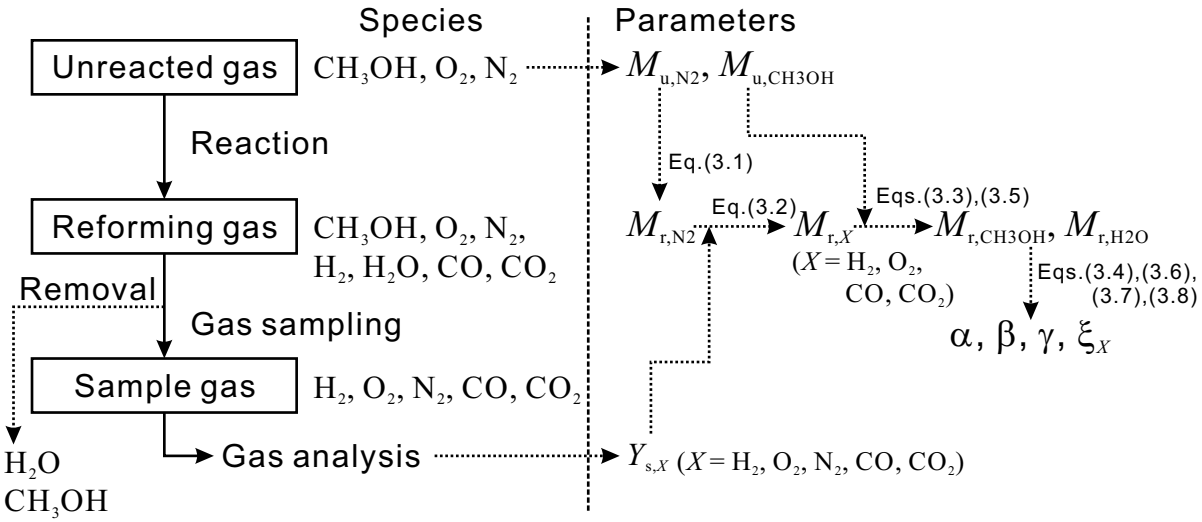

Figure 3.5: Procedure to calculate the evaluation parameters.

reformer can be expressed as

$$\mathrm{CH_3OH} + \frac{3}{2\phi}\left(\mathrm{O_2} + 3.76\,\mathrm{N_2}\right) \rightarrow (1-\alpha)\,\mathrm{CH_3OH} + \frac{3}{2\phi} \times 3.76\,\mathrm{N_2} + 2\alpha\beta\,\mathrm{H_2} + 2\alpha(1-\beta)\,\mathrm{H_2O} + \alpha\gamma\,\mathrm{CO} + \alpha(1-\gamma)\,\mathrm{CO_2}. \quad \text{(R 3.1)}$$

3.4 Numerical Analysis

3.4.1 Chemical Equilibrium

For the calculation of the chemical equilibrium, we assume the chemical formula of a fuel to be $\mathrm{C}_n\mathrm{H}_m\mathrm{O}_l\mathrm{N}_k$ (for methanol in this case, $(n, m, l, k) = (1, 4, 1, 0)$), and atmospheric air is introduced as an oxidizer.

When the mixture is lean ($\phi \leq 1$), the reaction is defined such that the products are simply CO_2 and H_2O. When the mixture is rich ($\phi > 1$), on the other hand, and the reaction temperature is relatively low (less than 2000 K), the additional species produced

are: CO and H_2. Therefore, the overall combustion reaction can be written as

$$\phi\epsilon\, C_nH_mO_lN_k + (O_2 + 3.76\, N_2) \longrightarrow \nu_1\, CO_2 + \nu_2\, H_2O + \nu_3\, N_2 + \nu_4\, O_2 + \nu_5\, CO + \nu_6\, H_2, \quad \text{(R 3.2)}$$

where ϵ is the stoichiometric molar ratio of fuel to O_2 ($\epsilon = 4/(4n + 3 - 2l)$), and ν_i ($i = 1, 2, \ldots, 6$) represents the coefficients of the product composition.

The following approximations for lean and rich combustion are used to determine the product composition.

$$\phi \leq 1 \qquad \nu_5 = \nu_6 = 0 \tag{3.9}$$

$$\phi > 1 \qquad \nu_4 = 0 \tag{3.10}$$

For lean or stoichiometric cases, atom-balance equations are sufficient to determine the product composition (four unknowns in four equations). For rich case, since additional product species are considered, the following water-gas shift (WGS) reaction and equilibrium constant need to be introduced.

$$CO + H_2O \rightleftharpoons CO_2 + H_2 \tag{R 3.3}$$

$$K = \frac{\nu_1\nu_6}{\nu_2\nu_5} \tag{3.11}$$

This equilibrium constant, K, is dependent only on temperature, therefore, if the reaction temperature is given, the product composition can be determined. The product composition solutions for both lean and rich cases are summarized in Table 3.4 [3].

In a fuel-rich condition, the parameter ν_5 is given by the solution of a quadratic equation:

$$a\nu_5^2 + b\nu_5 + c = 0, \tag{3.12}$$

Table 3.4: Combustion products, ν_i [mol/mol of O_2].

Number	Species	$\phi \leq 1$	$\phi > 1$
1	CO_2	$n\phi\epsilon$	$n\phi\epsilon - \nu_5$
2	H_2O	$m\phi\epsilon/2$	$2 - \phi\epsilon(2n - l) + \nu_5$
3	N_2	$3.76 + k\phi\epsilon/2$	$3.76 + k\phi\epsilon/2$
4	O_2	$1 - \phi$	0
5	CO	0	ν_5
6	H_2	0	$2(\phi - 1) - \nu_5$

where

$$a = 1 - \frac{1}{K}, \tag{3.13}$$

$$b = 2 - \phi\epsilon(2n - l) + \frac{1}{K}[2(\phi - 1) + n\phi\epsilon], \tag{3.14}$$

$$c = -2n\phi\epsilon(\phi - 1)\frac{1}{K}. \tag{3.15}$$

Therefore, the solution can be expressed as:

$$\nu_5 = \frac{-b + \sqrt{b^2 - 4ac}}{2a}. \tag{3.16}$$

By using this simple procedure, the product composition can be calculated for given ϕ and temperature conditions.

3.4.2 Adiabatic Flame Temperature

In an adiabatic and constant pressure process in an open system, the first law of thermodynamics leads to

$$\Delta h = e_b, \tag{3.17}$$

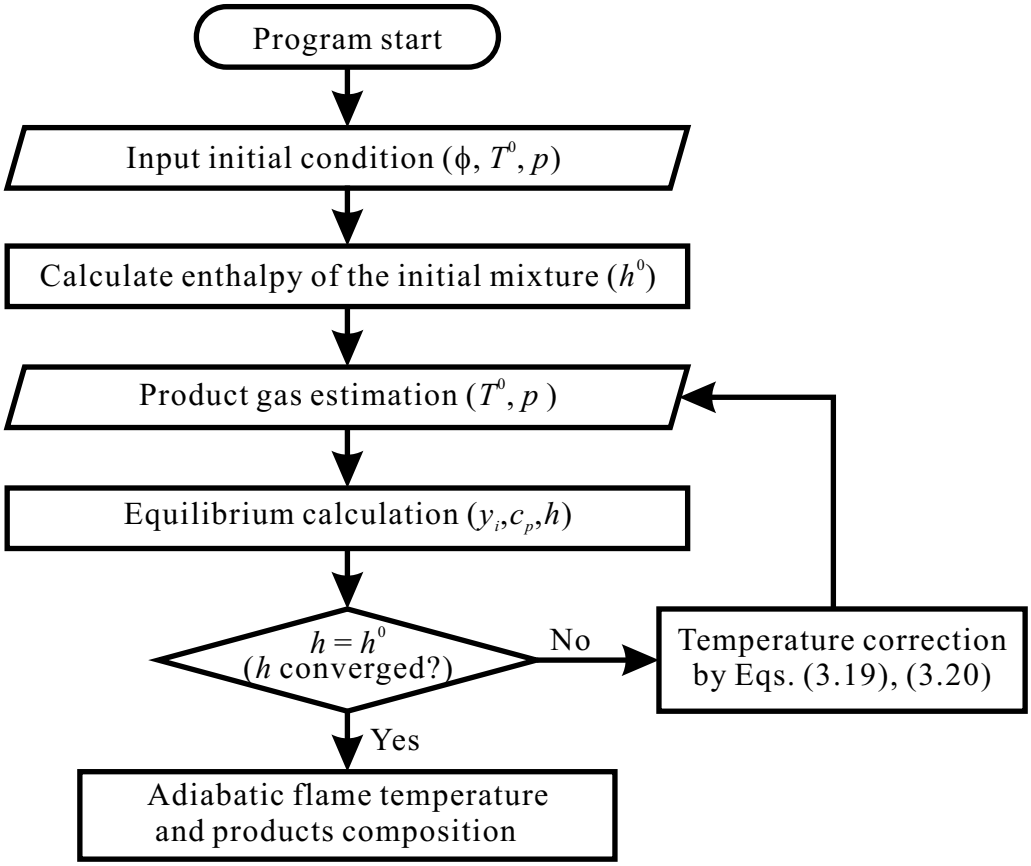

Figure 3.6: Flow chart of the calculation of the adiabatic flame temperature.

where Δh is the enthalpy increase of the system during the process, and $e_{\rm b}$ is the amount of energy transferred through the boundary into the system. This equation means that the enthalpy of the product is equal to that of reactant plus any heat transferred through the boundary, for example energy gain from the outside of the system or energy loss to the environment. In this case, since the system is assumed to be adiabatic, the energy transferred through the boundary is zero. Therefore, the equation can be re-written as

$$\Delta h = 0. \tag{3.18}$$

The flow chart of the calculation of the adiabatic flame temperature, $T_{\rm af}$, and the product composition is shown in Fig. 3.6. To calculate $T_{\rm af}$ and the product composition, the initial conditions of the mixture (ϕ, p, T^0) are input. The enthalpy h^0 possessed by

the initial mixture is calculated from the given initial condition. Then, we set the first estimate of the product gas temperature, T^1 (in this case, $T^1 = 1500\,\mathrm{K}$). For the estimated temperature, T^1, the estimated products compositions, y_i^1, are calculated by the procedure presented in Sec. 3.4.1. In addition, the specific heat of the product mixture, c_p^1, and total enthalpy of the products, h^1, are calculated. However, the first value of the estimated enthalpy, h^1, is deviated from the initial value h^0 due to the deviation of the temperature estimation, T^1, from the actual T_{af}. We, then, re-estimate the temperature by the following equations and do the iteration loop until the temperature converges.

$$\Delta T = \frac{h^j - h^{j-1}}{{c_p}^j} \tag{3.19}$$

$$T^{j+1} = T^j + \Delta T \tag{3.20}$$

By the iteration, T_{af} can be calculated for the given initial temperature and the mixture composition. The validity of the calculation was confirmed by Ref. [4].

3.5 Results and Discussion

3.5.1 Chemical Equilibrium

The adiabatic flame temperature and the composition of the product gas were calculated to estimate the reformer performance on the assumption that the reforming reaction can be represented by fuel-rich combustion. Usually, a combustor is designed to assure the reactant mixture to have enough residence time to attain chemical equilibrium. Therefore, we introduce the calculation to confirm whether the reaction in the experiment reaches the chemical equilibrium or not. The numerical results shown in this section will be compared with the experimental results for the evaluation of the present fuel reformer and its performance.

As mentioned in Sec. 3.2.5, a mixture was introduced to the reactor at a constant temperature of 420 K. Therefore, the initial temperature in the calculation, T_0, was also set to 420 K. The chemical equilibrium composition and adiabatic flame temperature

were calculated by a numerical iteration under a constant enthalpy (adiabatic) condition, considering the major product species: CO_2, H_2O, H_2, O_2, and CO.

In addition, calculations of the product gas composition under specified reaction temperatures, T_{gas}, were also performed in several ϕ conditions. These calculations considered the conservation of elements and equilibrium of WGS reaction under given temperature conditions.

The numerical results of the equilibrium composition of the product and adiabatic flame temperature, T_{af}, of methanol–air combustion in various ϕ conditions are shown in Fig. 3.7.

First, the dependence of the equilibrium composition on ϕ is shown in Fig. 3.7(a). Note that this graph shows wet-based concentration of the reforming gas. In a fuel-rich condition, O_2 supply is reduced from the stoichiometric mixture. Therefore, supplied O_2 is consumed completely in all the conditions of our interest, $\phi > 2.0$.

In the present calculation, all the supplied methanol is assumed to react, and unreacted fuel loss is not considered. Therefore, incomplete products, H_2 and CO, are produced due to the lack of O_2 in fuel-rich conditions.

The value of T_{af} in Fig. 3.7(b) decreased monotonically with an increase in ϕ. This is due to the decrease in the heat release rate of the reaction in higher ϕ. In a complete combustion reaction, most of the energy possessed by methanol (LHV-basis) is released as heat, so that the high reaction temperature is obtained. However, in a fuel-rich case, incomplete reaction occurs, which produces CO and H_2. These products store a portion of energy which was supposed to be released in complete combustion, so that the reaction temperature decreases.

Other species in Fig. 3.7(a) are influenced by the dilution effect of N_2. In this calculation, N_2 is assumed to be unchanged during the reaction, therefore, the decrease in Y_{N2} with an increase in ϕ represents directly the decrease in air supply in higher ϕ. The effect of N_2 dilution varies with respect to ϕ conditions; a smaller ϕ means a larger N_2 flow rate condition, which results in a larger effect of N_2 dilution. Thus, in order to separate the dilution effect from the result, several parameters defined in the previous section are

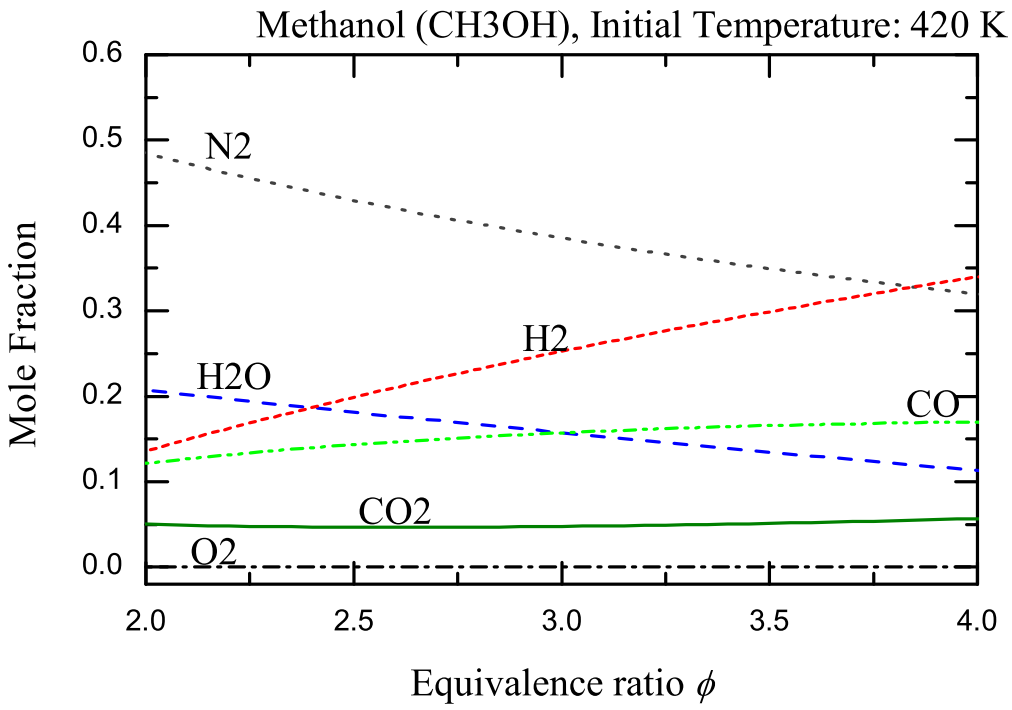

(a) Equilibrium composition of major species

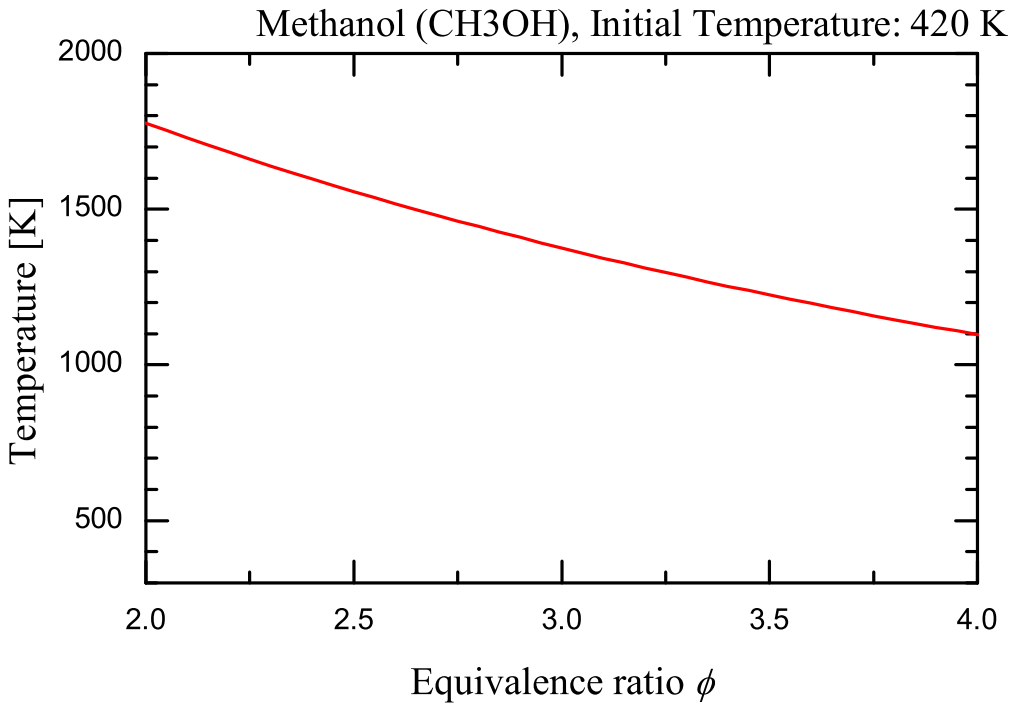

(b) Adiabatic flame temperature

Figure 3.7: Equilibrium composition of the product gas and adiabatic flame temperature.

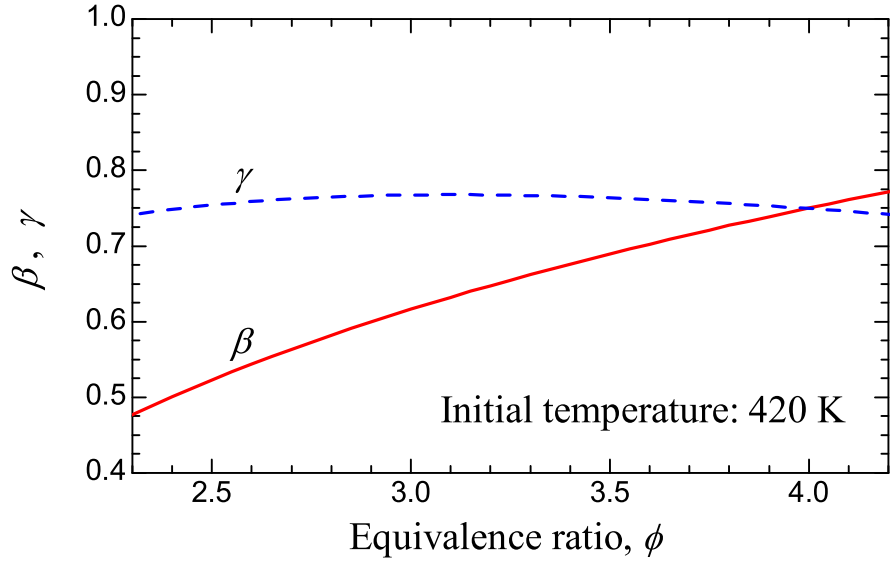

Figure 3.8: Preferential production ratios by the chemical equilibrium calculation.

introduced.

Figure 3.8 shows the dependence of the preferential production ratio of H_2, β, and that of CO, γ, on ϕ in the adiabatic flame. As shown in the figure, β increases monotonically with ϕ, and its variation range is relatively large. On the other hand, γ takes an almost-constant value but has a gentle peak at $\phi \approx 3.1$. The reasons of these trends will be discussed later.

Figure 3.9 shows the product gas composition at fixed ϕs under a given reaction temperature, T_{gas}, varied from 500 to 1500 K. In the calculation, since ϕs are fixed at constant values, the mole fraction of N_2 stays at a constant value. This is because the total molar flow rate of working gas does not vary by the reaction due to the absence of unreacted methanol. This means the effect of N_2 dilution does not change in a figure. Therefore, only the temperature dependence of the chemical equilibrium appears in the figure.

The chemical equilibrium considered in the calculation is that of WGS reaction. Since the WGS reaction is a moderately exothermic reaction, the chemical equilibrium shifts to the reactant side ($CO + H_2O$) with an increase in temperature, while it shifts to the product side ($CO_2 + H_2$) with a decrease in temperature. That is to say, with an increase

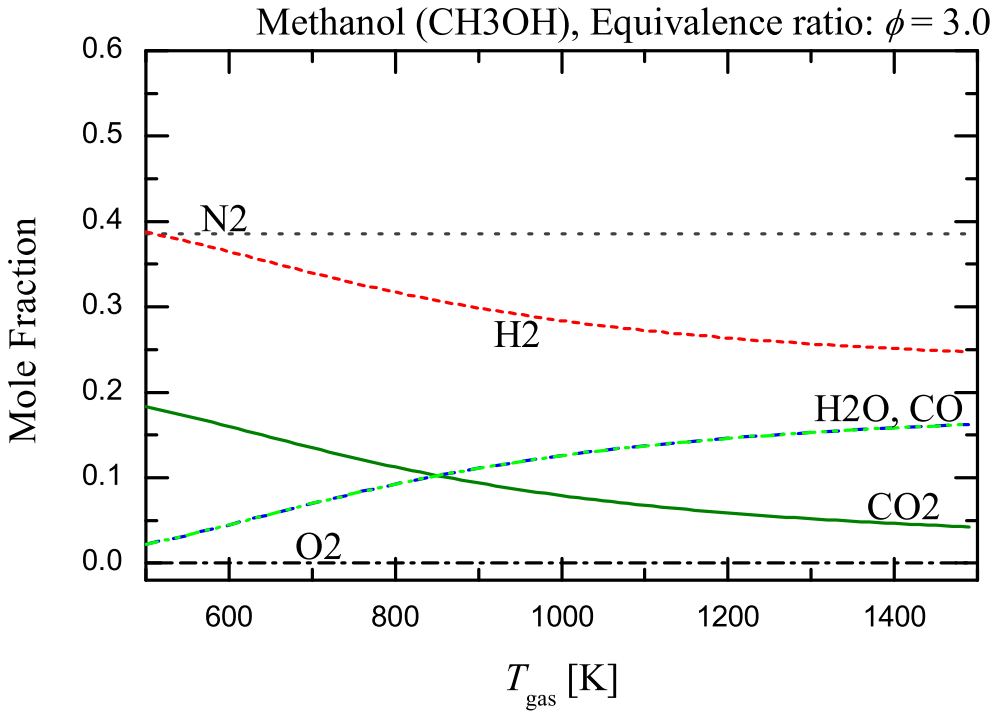

(a) $\phi = 3.0$

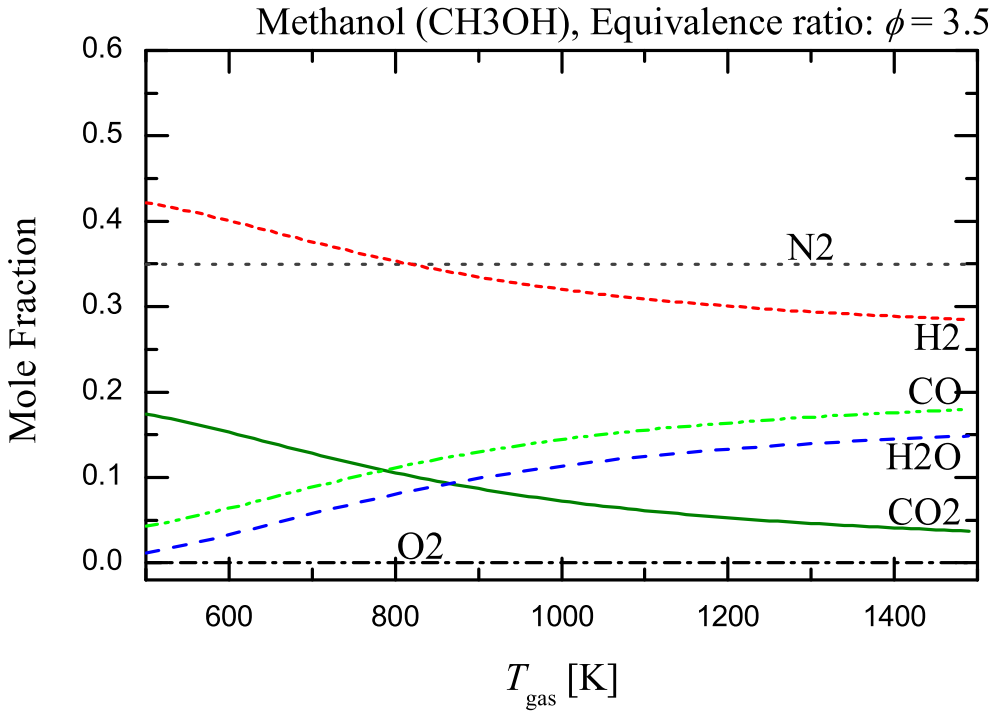

(b) $\phi = 3.5$

Figure 3.9: Temperature dependence of the equilibrium product composition in calculation.

in temperature, the fractions of CO and H_2O increase, while those of H_2 and CO_2 decrease. This dependence of each species concentration on temperature is correctly predicted in the numerical results shown in the figure. The same trend can be seen in both $\phi = 3.0$ and 3.5.

Figure 3.10 shows the contour of β and γ plotted in the figure with ϕ on the abscissa and T_{gas} on the ordinate. The adiabatic flame temperature, T_{af}, as a function of ϕ is also plotted as a broken line in the figure.

The contour shows that β increases with an increase in ϕ or a decrease in T_{gas}. While, the value of γ increases with an increase in ϕ or an increase in T_{gas}. When ϕ is increased, the amount of O_2 supply is reduced so that the rate of incomplete reaction increases. This incomplete reaction produces more CO and H_2. Therefore, ϕ vs. β (or ϕ vs. γ) has positive correlation. On the other hand, when T_{gas} is increased, the chemical equilibrium of WGS reaction shift to the product side, which increases the amount of CO, and reduces that of H_2. Therefore, T_{gas} and γ has a positive correlation, while T_{gas} and β has a negative one. As a consequence, the trend of β and γ regarding ϕ agrees with each other, however, that in T_{gas} disagrees. This disagreement causes the different trend of β and γ in Fig. 3.8. The broken line indicating T_{af} crosses the contour lines nearly at right angles as shown in Fig. 3.10(a), while the broken line runs nearly parallel to the contour lines in Fig. 3.10(b). The relatively large increase in β in Fig. 3.8 is caused by this orthogonal relation between the contour lines and the T_{af} plot in terms of ϕ. On the other hand, an almost-constant distribution of γ having a gentle peak at $\phi \approx 3.1$ is due to the parallel feature of T_{af} in the contour.

Therefore, it is estimated by the above calculation, the value of β has a great sensitivity to ϕ, while γ is not so much affected by ϕ in the ϕ conditions of our interest.

3.5.2 Reaction Regime and Temperature Distributions

In this reformer, a steady-state, fuel-rich flame of methanol could be stabilized in the vicinity of Honeycomb A. The operating limit was extended to $\phi = 5.0$, even though the upper flammability limit of methanol is $\phi = 4.07$ [5]. This is due to the thermal

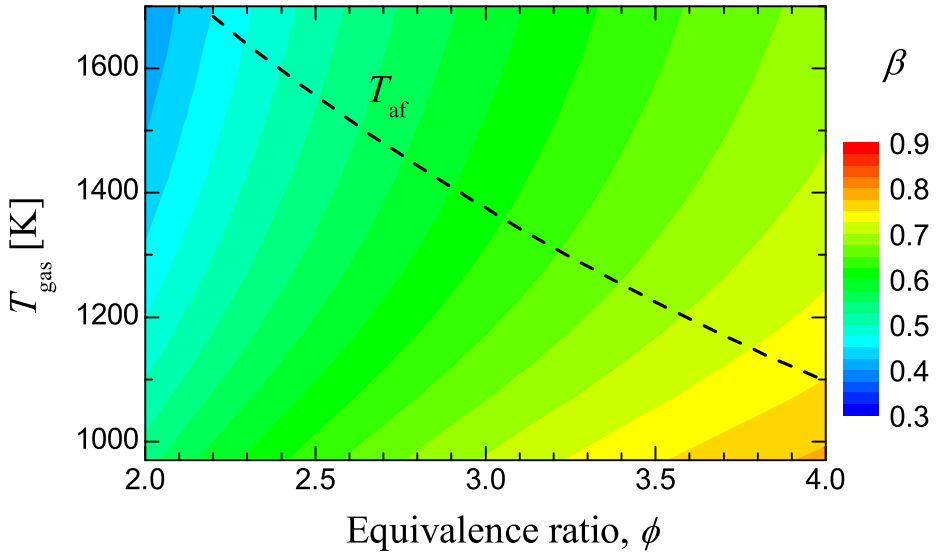

(a) β

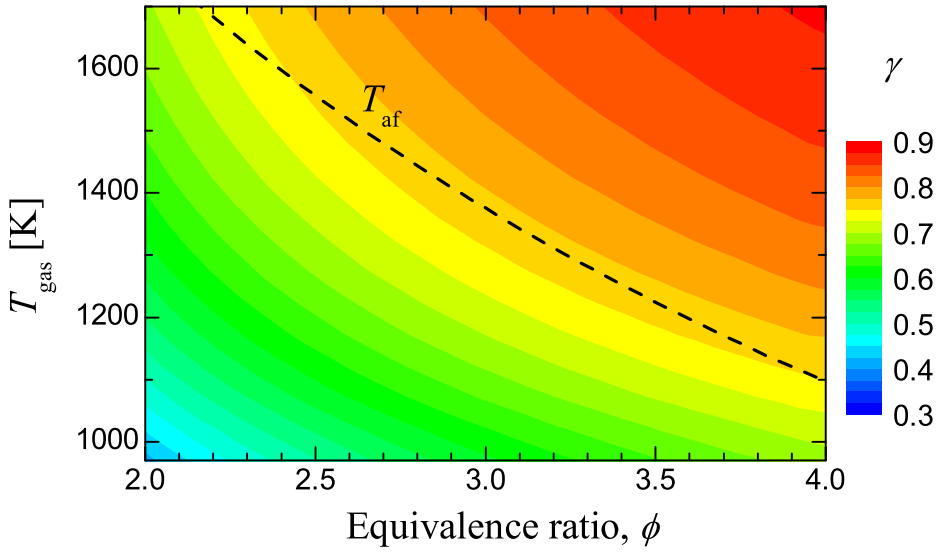

(b) γ

Figure 3.10: Contour of the preferential production ratios with respect to the reaction temperature, T_{gas}, and equivalence ratio, ϕ.

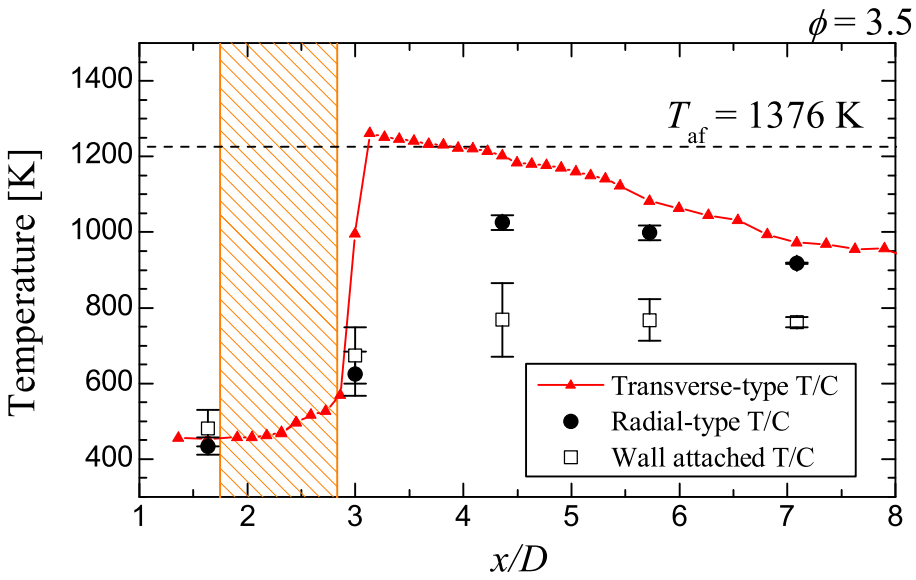

Figure 3.11: Typical streamwise temperature distributions measured by several types of thermocouples.

characteristics of the ceramic honeycomb.

Figure 3.11 shows the typical temperature profiles measured at the center axis of the reactor using both radial-type (plotted by •) and transverse-type probes (plotted by ▲). Temperature profile on the reactor outer wall surface is also shown (plotted by □) in the figure. The calculated value of the adiabatic flame temperature in the corresponding ϕ condition, T_{af}, is shown as a broken line in the figure.

Since the radial positions of the temperature measurements are identical between the radial-type and transverse-type probes, the readings of these two probes should also be identical. However, the values of these two probes disagree in the high-temperature region ($x/D \sim 4.4$); the transverse-type probe indicated higher temperature values than that of the radial-type probes. This inconsistency was caused by the difference of the extent to which the probe is cooled by radiation and conduction heat transfer effects.

It is well known that the flame temperature measured by bear-bead thermocouple is significantly affected by radiation error [6]. When a flame is confined by a cooler surrounding wall and a thermocouple bear-bead is exposed to the flame, the apparent thermocouple

junction temperature becomes lower than the actual gas temperature, since the radiation loss from the surface of the thermocouple bead to the surrounding wall reduces the bead temperature.

The thermal conduction through the rod material of the thermocouple probe, on the other hand, is also a major cause of temperature error. In the present apparatus, the thermocouple junctions of the radial-type probes are attached to the ceramic tube tip, so that the effect of the ceramic tube working as a heat sink is significant for the temperature reading. The ceramic tube inserted to the reactor experiences heat conduction in a radial direction, and also the ceramic tube surface emits radiation to the surrounding reactor wall which is cooler than the reacting gas. By these thermal effects, the temperature of the ceramic tube becomes lower than the actual gas temperature, which results in the lower temperature indication of the thermocouple than the actual gas temperature. Therefore, the actual temperature value of the reacting gas should be higher than the profile indicated in the figure, and this disagreement is especially remarkable in the high-temperature region since the thermal loss from the thermocouple becomes larger as the temperature increases.

The transverse-type probe also experiences a radiation cooling, though the degree of cooling is smaller than the radial-type probe. In the literature, temperature decrease by the the radiation loss using 0.25 mm bear-bead thermocouple exposed to the high temperature gas of 1200 K with the velocity of 0.5 m/s and confined by 773 K surrounding wall is estimated about 80 K [7]. In the present case, the thermocouple wire is much finer than the literature, 0.1 mm, therefore, the temperature decrease may be much smaller. However, since the precise temperature distribution of inner wall surface is not available, the accurate radiation corrections are not possible. Therefore, we use the temperature values by the transverse-type probes without a correction for quantitative discussion. Radial-type data, on the other hand, is used for qualitative and schematic discussion.

The wall temperature of the reactor is higher than the gas temperature at the center axis in the upstream region of the reactor($x/D \leq 3$). In addition, gas temperature inside Honeycomb A is far beyond the boiling temperature of methanol (338 K). Thus, the mixture

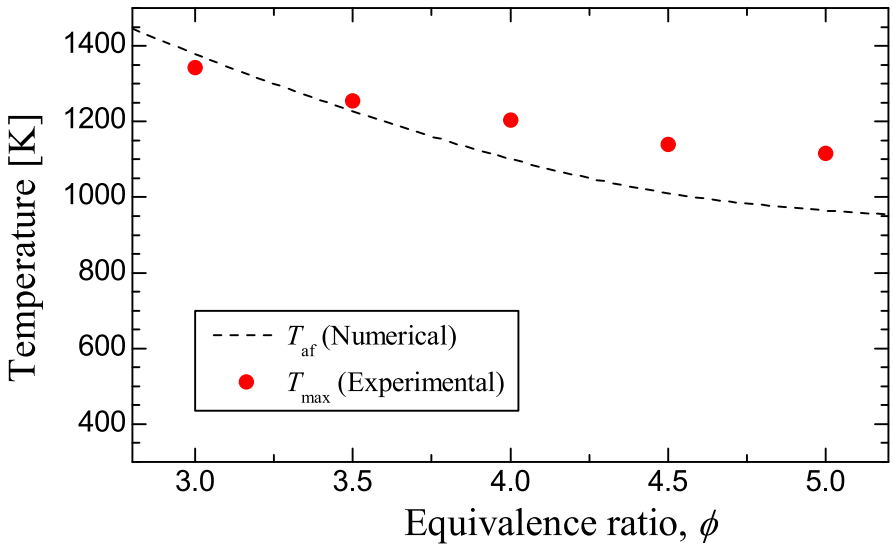

Figure 3.12: Calculated adiabatic flame temperature and measured maximum flame temperature in various ϕ conditions.

is preheated and evaporation of methanol is completed due to the high temperature solid surface of the ceramic honeycomb which is heated up by the heat transferred through the reactor wall by conduction and the radiation from the downstream region.

Although no visualization of the flame was conducted, the temperature profile in Fig. 3.11 indicates that the reaction occurs in the vicinity of Honeycomb A where the steep temperature gradient is observed in as wide as several millimeters to one centimeter region. The maximum flame temperature, $T_{\max}$, reached slightly beyond the adiabatic flame temperature, $T_{\rm af}$. This means the reaction occurred in an adiabatic manner when the flame is stabilized in the vicinity of Honeycomb A.

Major exothermic reaction took place in the region of several centimeters where steep temperature gradients were observed. In the downstream region, on the other hand, the gas temperature decreased monotonically, which corresponds to the heat loss to the environment.

Figure 3.12 shows the relation between $T_{\max}$ and ϕ plotted with the adiabatic flame temperature, $T_{\rm af}$. From these results, the present reactor using a ceramic honeycomb can

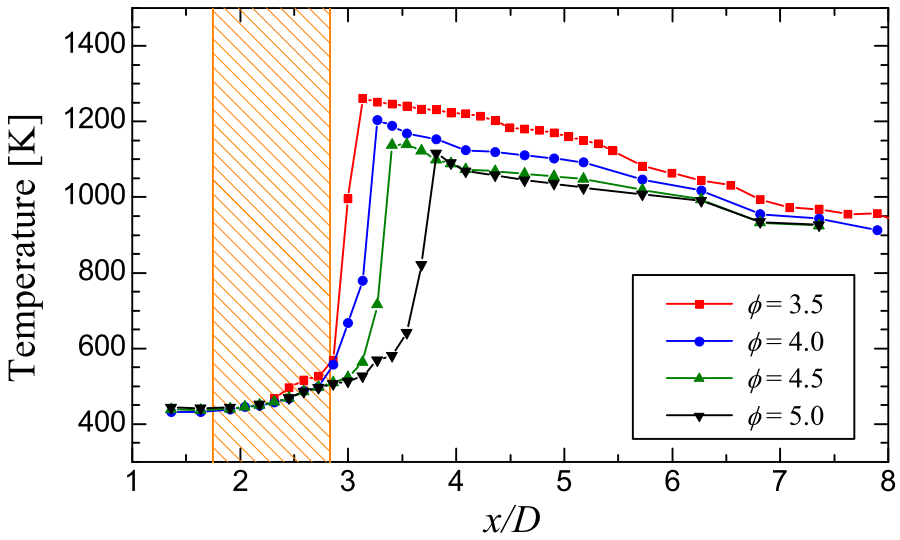

Figure 3.13: Streamwise gas temperature distributions at the axial center of the reactor in various ϕ conditions.

achieve almost an adiabatic flame. In all cases, the flame temperature, $T_{\max}$, is close to or beyond T_{af}. This is due to the existence of the solid surface of the ceramic honeycomb. The solid surface existing close to the flame is heated up by the flame, which enables the mixture to be preheated, so that the local heat recirculation can be realized. This characteristic enabled the released heat to stay in the vicinity of the honeycomb and the reaction to occur in an adiabatic manner. This feature of heat exchange between the flame and the ceramic honeycomb is so-called "internal heat recirculation" [8,9].

Temperature distributions in several ϕ conditions measured by the transverse-type probe are shown in Fig. 3.13. In all ϕ cases, temperature profiles showed a similar shape, i.e., the maximum flame temperature was observed at the outlet of Honeycomb A, and then the temperature decreased as the gas travels downstream. The location where the maximum flame temperature was observed moved downstream as ϕ was increased. In other words, in richer ϕ conditions, the reaction needed longer distance and time after the mixture gas passing through Honeycomb A. This is due to the dependence of the reaction speed of POX on ϕ. As ϕ is increased, the reaction speed represented by the laminar burning velocity

is decreased, which results in the slower reaction. Therefore, by increasing ϕ, the flame location shifted downstream to shape a stable flame and eventually blew off when ϕ exceeds 5.0.

The values of $T_{\max}$, on the other hand, decreased as ϕ was increased (also see Fig. 3.12). In addition to the same reason as T_{af} decreasing in higher ϕ due to the formation of H_2 and CO, the decrease in O_2 supply resulted in the lower methanol conversion ratio, α, which decreased the flame temperature. Moreover, the effect of heat loss to the environment decreased the gas temperature especially in higher ϕ conditions, where the ratio of the heat loss to the heat release rate became large. By these two effects, in higher ϕ conditions, the gas temperature decreased which determined the operating limit $\phi = 5.0$.

Figure 3.14 shows the radial temperature distributions at Position i to Position v, corresponding to the five radial-type probes. Each figure (a)–(c) shows the profile in each ϕ condition with a dimensionless radial coordinate, r/D, on the abscissa and measured temperature on the ordinate. The chain line in the graph indicates the center axis of the reactor, and the hatched region means the reactor wall. At Position i, in all ϕ conditions, temperature of the reactor wall is higher than the gas temperature, and the temperature decreases toward the center of the reactor. In this region, the reaction involving heat release has not started, therefore, the mixture supplied from the baffle plate was just heated to about 470 K, but the temperature was still low for the exothermic reaction to start in this region.

At Position ii, the temperature profile differs with ϕ conditions. For a comparison, temperature profiles at Position ii are picked out to Fig. 3.15. In a higher ϕ condition ($\phi = 4.0$), the temperature profile is almost flat even at the outlet of Honeycomb A (Position ii), while in $\phi = 3.0$ or 3.5, the drastic temperature increase is observed in the surrounding region ($0.25 \leq r/D \leq 0.45$). The temperature rise observed at Position iii is larger in smaller ϕ conditions.

Figure 3.16 shows the streamwise temperature distributions at several radial locations ($r/D = 0$, 0.16, 0.33, and 0.49) in $\phi = 3.0$ condition. From this figure, the temperature rise

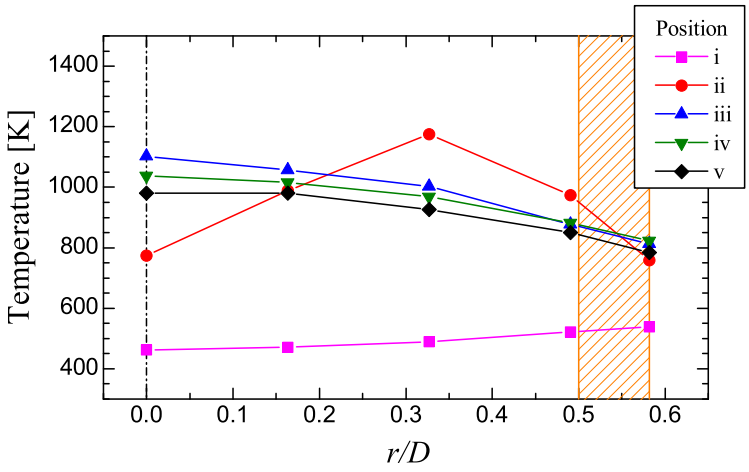

(a) $\phi = 3.0$

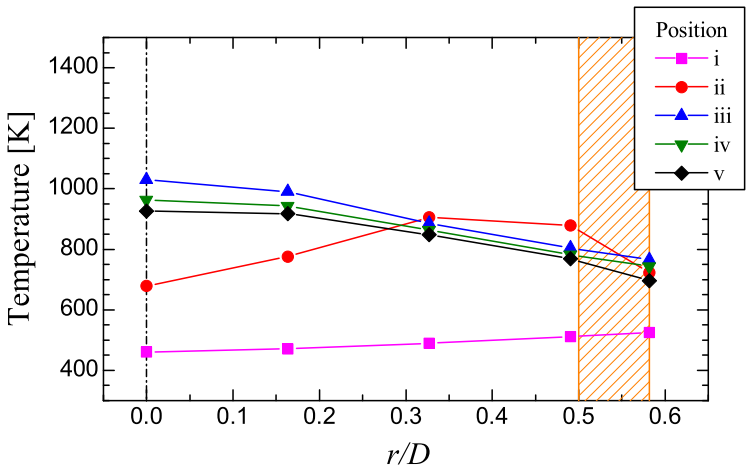

(b) $\phi = 3.5$

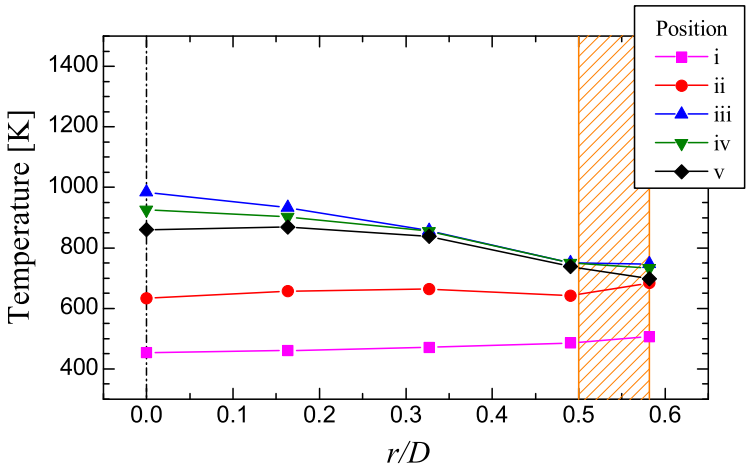

(c) $\phi = 4.0$

Figure 3.14: Radial temperature distributions at each position in the reactor measured by radial-type thermocouples.

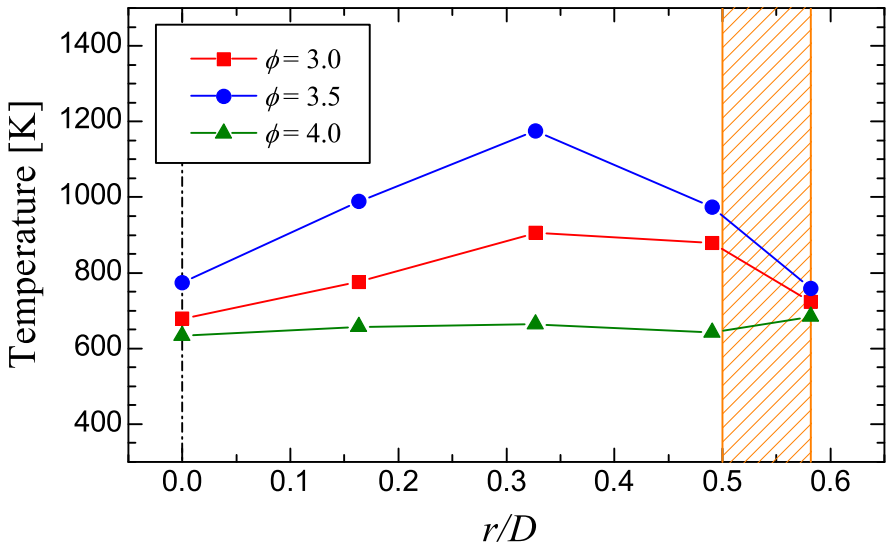

Figure 3.15: Radial temperature distribution at Position ii in each ϕ condition.

at $r/D = 0.33$ is observed at more upstream location than that of $r/D = 0$. This implies that the reaction region of this fuel reformer has a shape of parachute shown in Fig. 3.17; the mixture gas needs longer time or distance to start the reaction at the center axis than in the surrounding region.

The radial temperature distributions at Position iii to Position v in Fig. 3.14 shows the same trend; the maximum temperature is observed at the center axis and the profile has a mound-like shape. The temperature distributions are dominated by the convective heat transfer to the reactor wall so that the effects of the location of the reaction did not appear in the the downstream temperature distributions.

Finally, by integrating the results of temperature distributions, the role of the ceramic honeycomb is summarized as follows:
At the outlet of Honeycomb A, the gas temperature is 70–130 K higher than the initial temperature, 420 K. This indicates that the vicinity of Honeycomb A worked as a preheating region where the premixed gas was heated up by the solid surface of the ceramic honeycomb. The reason why temperature of the outlet of Honeycomb A becomes high can be explained

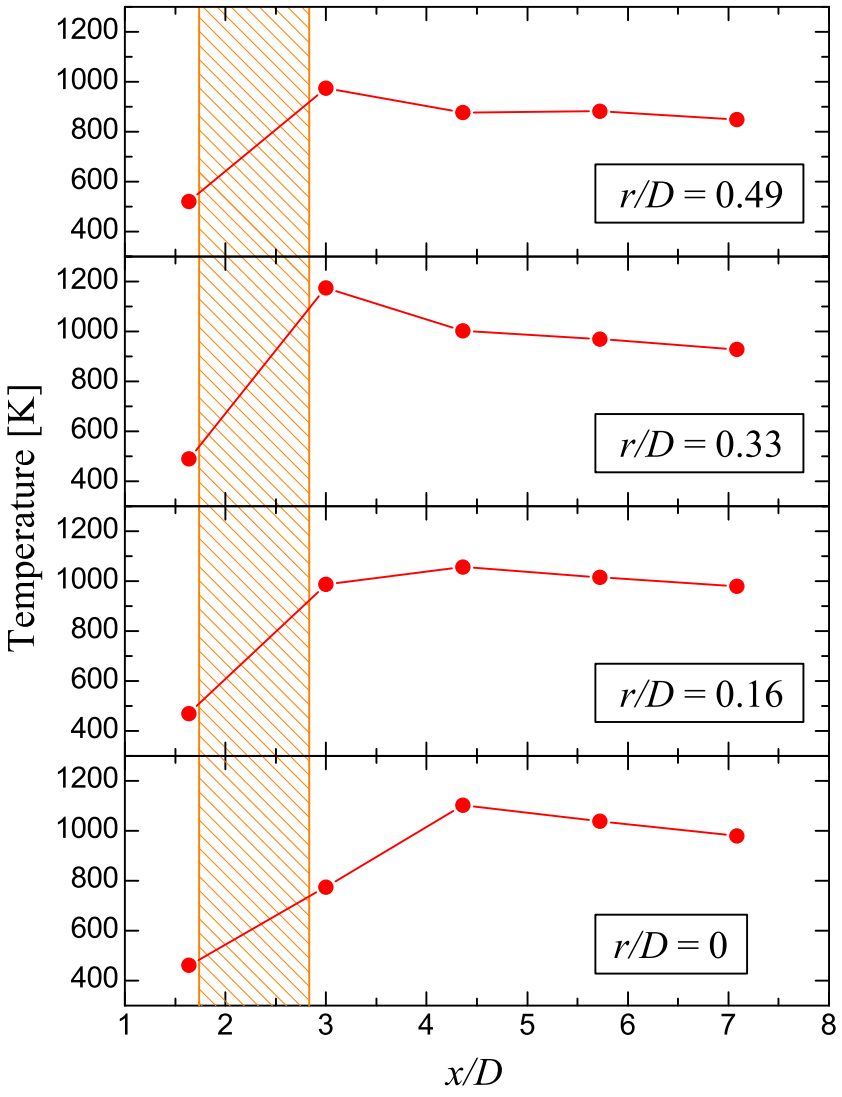

Figure 3.16: Streamwise temperature distribution measured at each radial location (ϕ = 3.0).

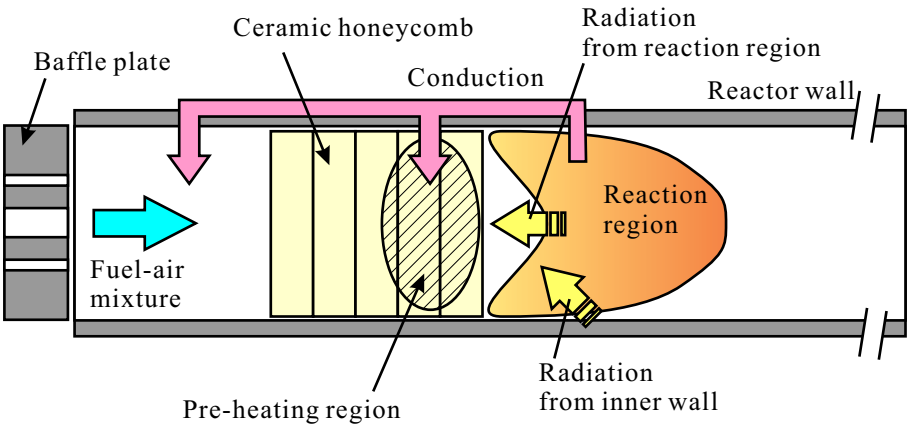

Figure 3.17: Schematic of the energy flow realized within the reactor.

by the conduction heat transfer through the reactor wall, and the thermal radiation from downstream region. Regarding the conduction heat transfer, it is seen in Fig. 3.11 that the wall temperature, T_{ex}, takes the maximum temperature at Position iii, which proves that there exists conduction heat transfer heading negative-x direction through the reactor wall around Position ii. On the other hand, it can also be shown that there exists high temperature inner wall downstream of Honeycomb A (see Fig. 3.14). Thus, the thermal radiation also takes part in heating up the outlet surface of Honeycomb A. By both of these effects, the outlet surface of Honeycomb A was heated up and took a role to preheat the mixture, which realized the "internal heat recirculation".

In addition, in the vicinity of Honeycomb A, the velocity had such a distribution that relatively smaller velocity realized in a near-wall region than in a center region. Due to the small velocity, the mixture in a near-wall region experienced a quicker heat up so that the reaction started more closer to Honeycomb A than the mixture in a center region. Therefore, the reaction region formed a parachute-like shape shown in Fig. 3.17.

The characteristic of the reaction shape and its stability will be discussed in the next chapter, where the visualization and the numerical simulation of the flame are conducted and both of these results are compared in detail.

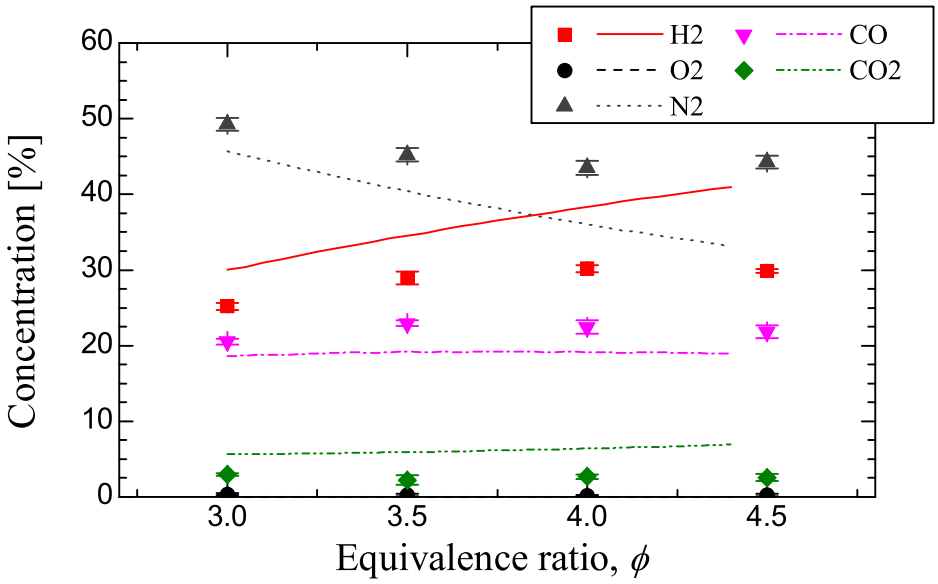

Figure 3.18: Product gas composition in dry-basis. Symbols indicate the experimental results, and lines shows the chemical equilibrium calculation.

3.5.3 Reforming Characteristics

Figure 3.18 shows the dependence of the sample gas composition on ϕ. The gas analysis was conducted by gas chromatograph after the sample gas was dried by a filtering chamber with silica gel. Thus, the concentrations of unreacted methanol and produced water in the reforming gas were not taken into account. The calculated values of the dry-basis equilibrium gas composition in an adiabatic flame are also plotted as lines in the figure.

The values of Y_{O2} in experiments are below 0.5 % in all ϕ conditions. In fuel-rich conditions, the amount of O_2 is reduced compared with the stoichiometric mixture of complete combustion. Therefore, supplied O_2 was totally consumed by the reforming reaction, which agreed with the numerical result.

In $\phi \leq 4.0$, Y_{H2} increases slightly with ϕ, while it stays at a constant value in $\phi > 4.0$. The numerical result, on the other hand, shows that Y_{H2} increases monotonically with ϕ. This monotonic increase in the numerical Y_{H2} is due to the reduction of the N_2 dilution effect and the equilibrium shift of the WGS reaction. As mentioned previously, the

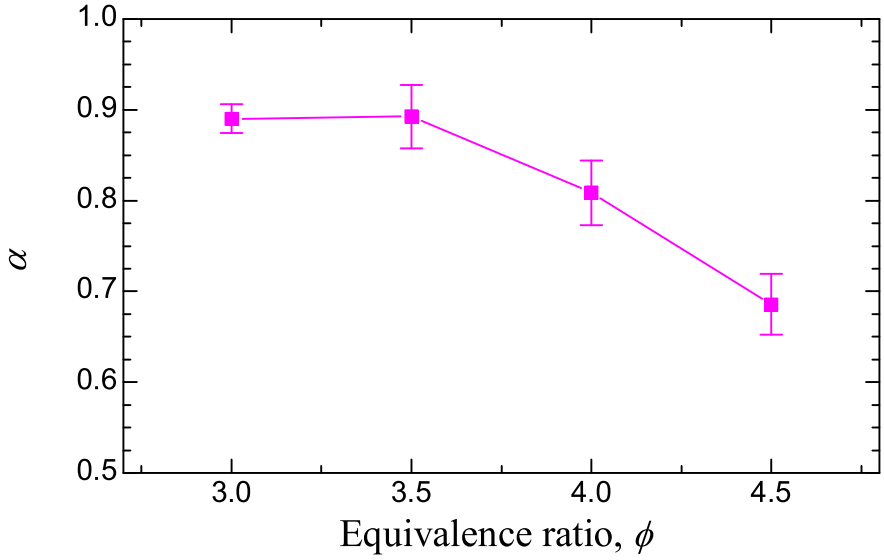

Figure 3.19: Methanol conversion ratio, α.

equilibrium of WGS reaction shifts to the product side (CO_2 + H_2) when the temperature decreases in the fuel-rich conditions. However, the numerical result does not consider the unreacted methanol, which is significant in fuel-rich conditions. Therefore, the value of Y_{H2} in calculation is overestimated in fuel-rich conditions.

The experimental results of CO and CO_2 concentrations agree roughly with the numerical ones in the present operating conditions. Both results stays almost at constant values in $\phi \geq 3.0$.

If the value of Y_{H2} is the only concern, the optimum operating condition of this fuel reformer is $\phi = 4.0$. However, it is necessary to consider the effects of removed water and methanol for more precise evaluation in the following discussion.

Figure 3.19 shows the relation between methanol conversion ratio, α, and ϕ. The value of α decreases monotonically in $\phi > 3.5$. As discussed in the results of gas concentration, the supplied O_2 is consumed totally in the reforming reaction. Therefore, the increase in ϕ directly caused the lack of O_2 which resulted in the reduction of methanol consumption. While in smaller ϕ conditions, the O_2 supply increased so that the volumetric heat release

rate increased, which caused the promotion of the methanol decomposition due to the higher temperature in the reactor. However, α became no larger than 0.9 in $\phi \leq 3.5$, which was the limit of α in the present reformer.

There are several important reasons that α did not reach unity with a decrease in ϕ: the effect of residence time in the reaction region, and the interaction between the reaction region and ceramic honeycomb. The first reason, the residence time, becomes important when the reaction speed is fairly slow. POX reaction is a combustion reaction in fuel-rich conditions, hence the reaction speed is slower than complete combustion reaction. In the present experimental procedure, the air flow rate was increased with a fixed fuel flow rate when ϕ was decreased. Therefore, the total mixture flow rate was increased in a smaller ϕ condition. The increase in flow rate means the increase in the mixture velocity, which results in the shorter residence time of the mixture within the reaction region. As the residence time became shorter, incomplete reaction was apt to happen, so that α did not reach unity even in the stoichiometric condition of POX, $\phi = 3.0$.

The second reason, the interaction of the reaction with the ceramic honeycomb, is related to the radiation and conduction loss of the reaction heat. When the equivalence ratio was decreased, the reaction became more vigorous, so that the reaction location moved more close to the ceramic honeycomb, or shifted into the ceramic honeycomb. If there exists solid surface within the reaction region, the heat diffuses by thermal radiation from the solid surface of the ceramic honeycomb and conduction through the solid phase having much higher thermal conductivity than the gaseous phase. These thermal loss effects may have caused the temperature drop of the reaction and produced unreacted methanol. The detail discussion of this thermal interaction will be presented in the next chapter.

Figure 3.20 shows the relation between the preferential production ratios of H_2, β and that of CO, γ, and ϕ. Equilibrium compositions in an adiabatic condition by calculation are also shown as lines in the graph. The value of β increased monotonically with ϕ in both numerical and experimental results. These results represent the equilibrium shift of the WGS reaction in the change of ϕ. However, the larger the equivalence ratio is, the larger

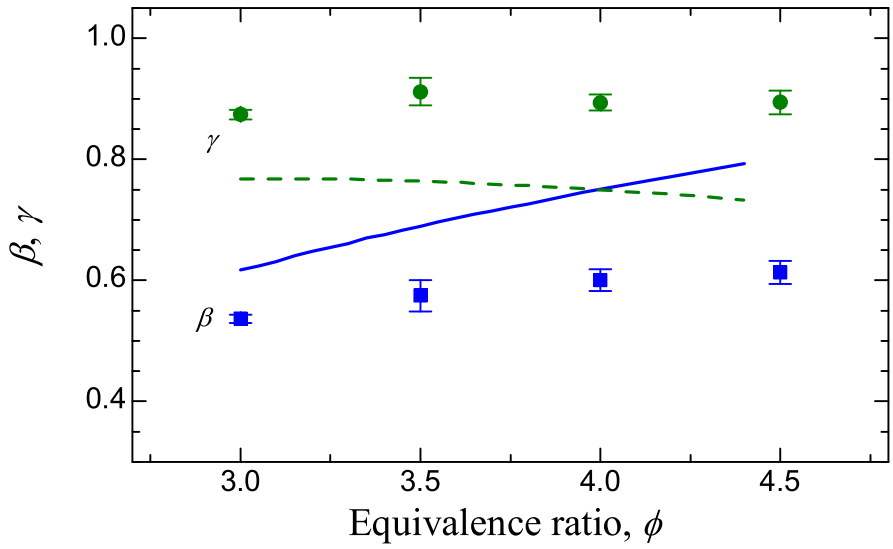

Figure 3.20: Preferential production ratios of H_2 (β) and CO (γ).

the deviation of the numerical result becomes. The deviation of the present combustion model from the experimental results became prominent in the fuel-rich region, where more precise reaction model incorporating C_2 species or other elementary processes are needed.

The value of γ shows an almost-constant distribution in experiments, and also in a numerical result. This result was expected in the equilibrium calculation that the balance of carbon atom does not experience a remarkable change with regard to ϕ in the present operating condition.

Figure 3.21 shows the dependence of production ratios, ξ_X, on ϕ. Since a molecule of methanol contains one carbon atom as well as four hydrogen atoms, the product species as a consequence of the reaction of one mole of methanol contains one mole in total of CO and CO_2, and two moles in total of H_2O and H_2 considering the conservation of atoms. Therefore, the maximum possible values of ξ_{CO} and ξ_{CO2} are one, while those of ξ_{H2} and ξ_{H2O} are two.

In all the species, the production ratios decreased in $\phi \geq 3.5$. This is because of the deterioration of α in fuel-rich conditions. The value of α decreased drastically from 90 %

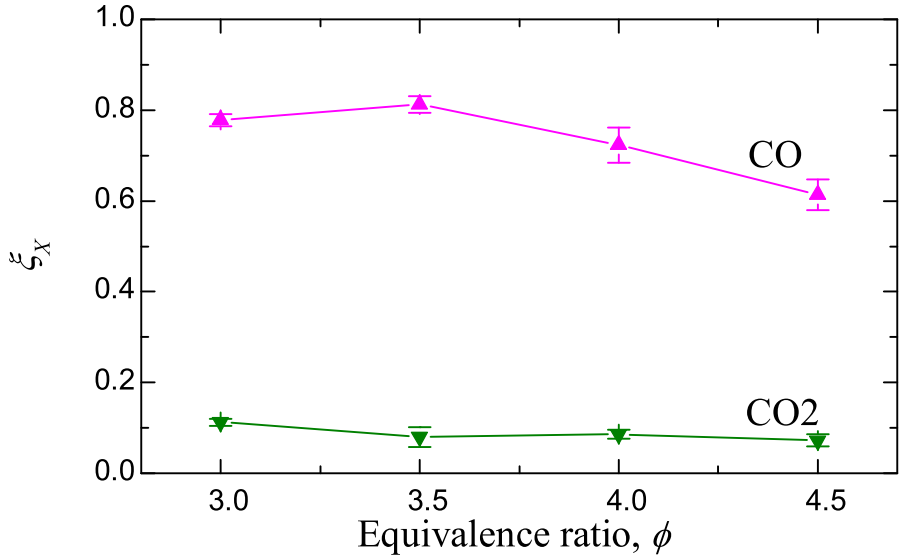

(a) C-species (CO and CO_2); the maximum possible value of ξ is one.

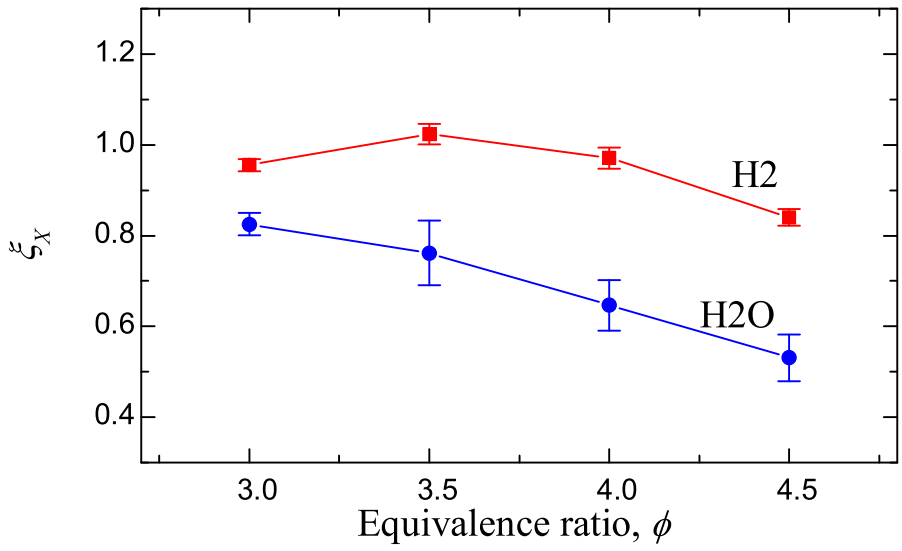

(b) H-species (H_2 and H_2O); the maximum possible value of ξ is two.

Figure 3.21: Production ratio of each species, ξ_X.

at $\phi = 3.5$ to below 70 % at $\phi = 4.5$ (see Fig. 3.19). This decrease in α directly caused the decrease in the production ratios in $\phi \geq 3.5$.

Using the relations described by Eq. (3.4) and Eq. (3.6) regarding CO and H_2, ξ_{CO} and ξ_{H2} can also be written as

$$\xi_{CO} = \alpha\gamma, \tag{3.21}$$

$$\xi_{H2} = 2\alpha\beta. \tag{3.22}$$

The value of ξ_{CO}, therefore, traced the same trend as α, since γ did not change so much with respect to ϕ as shown in Fig. 3.20.

The value of ξ_{H2}, on the other hand, took the maximum value at $\phi = 3.5$. As stated above, α decreased with an increase in ϕ, while β increased with ϕ. This trade-off relation between α and β made the value of ξ_{H2} having a peak at $\phi = 3.5$, since both α and β have an influence on the value of ξ_{H2} based on Eq. (3.22). In $\phi < 3.5$, α took almost a constant value, while β increased with ϕ. Thus, the value of ξ_{H2} increased with ϕ in $\phi < 3.5$. In $\phi > 3.5$, on the other hand, even though β increased with ϕ, the deterioration of α was so drastic that the resultant ξ_{H2} decreased with an increase in ϕ.

By this trade-off effect, the maximum performance in this reformer was realized at $\phi = 3.5$ which was a little richer condition than the stoichiometry of POX, $\phi_{st} = 3.0$. The total efficiency in this maximum performance is finally calculated. If the ideal reaction of methanol POX (shown as reaction (R 2.3)) occurs, H_2 production ratio becomes $\xi_{H2} = 2$. The maximum value of ξ_{H2} is 1.02 in $\phi = 3.5$, which is about 51 % of the ideal reaction. If calculated based on LHV, H_2 production efficiency is 37 %. This is not so much high, but still be competitive with the ICE system in a small scale system (see Fig. 2.1). Moreover, if utilizing also CO as a fuel, the efficiency increases as high as 71 %, which is competitive even in a large scale system. Note that the power supplied to the electric heaters is not considered in the above efficiency values. However, the exhaust gas still possesses a large amount of enthalpy, which can be recirculated to the evaporator to realize a truly self-sustainable

POX reactor in the future. The present POX reactor, therefore, is concluded to have a possibility to be utilized in a highly efficient hydrogen system.

3.6 Conclusions

In this chapter, the basic reaction characteristics of the methanol POX reaction were investigated. A tubular-type compact fuel reformer with an evaporator was fabricated and a ceramic honeycomb was introduced inside the reactor for stabilization of the reaction.

First, the adiabatic flame temperature and the equilibrium composition of methanol fuel-rich combustion was calculated. Using these results, the performance of the fuel reformer was estimated.

The experiments using the fuel reformer with a ceramic honeycomb was then conducted. It was possible to stabilize the reaction in a vicinity of the ceramic honeycomb in a wide range of equivalence ratio conditions. By the measurements of temperature, the thermal structure within the reactor was disclosed.

Then, the reaction characteristics of POX was investigated in terms of reforming gas composition, methanol conversion ratio, preferential production ratios, and production ratios of each species.

The following results were obtained through the discussion:

- The stable reaction of POX was realized using the ceramic honeycomb in the condition $3.0 \leq \phi \leq 5.0$, which was extended beyond the upper flammable limit of methanol combustion.

- The reaction took place in the vicinity of the ceramic honeycomb, and the reaction was occurred in an adiabatic manner due to the existence of the ceramic honeycomb near the reaction region.

- The outlet vicinity of the ceramic honeycomb worked as a preheating region which was realized by the conduction heat transfer through the reactor wall and the thermal radiation from the downstream region. This thermal effect of the ceramic honeycomb is summarized as “internal heat recirculation”.

- As ϕ is increased, the reaction region shifted downstream and eventually blew off when ϕ exceeded 5.0.

- The numerical results of the chemical equilibrium showed that, in the present operating conditions, the preferential production ratio of H_2, β, increases with the equivalence ratio, ϕ, and that of CO, γ, takes an almost-constant value, which agreed qualitatively with the experimental results.

- Due to the trade-off relation between methanol conversion ratio, α, and preferential production ratio of H_2, β, the maximum value of H_2 production ratio, ξ_{H2}, was realized at the slightly fuel-rich condition of $\phi = 3.5$.

- The present fuel reformer based on POX of methanol can achieve up to 71 % thermal efficiency (LHV-basis) if utilizing CO and H_2 as a syngas. This efficiency has a potential to be utilized in a highly efficient hydrogen energy system.

Bibliography

[1] Li, B., Kado, S., Mukainakano, Y., Nurunnabi, M., Miyao, T., Naito, S., Kunimori, K. and Tomishige, K., "Temperature Profile of Catalyst Bed during Oxidative Steam Reforming of Methane over Pt-Ni Bimetallic Catalysts", *Applied Catalysis A: General*, Vol. 304 (2006), pp. 62–71.

[2] Pan, C., He, R., Li, Q., Jensen, J. O., Bjerrum, N. J., Hjulmand, H. A. and Jensen, A. B., "Integration of High Temperature PEM Fuel Cells with a Methanol Reformer", *Journal of Power Sources*, Vol. 145 (2005), pp. 392–398.

[3] Ferguson, C. R., *Internal Combustion Engines: Applied Thermosciences*, (1985), pp. 108–114, John Wiley & Sons.

[4] Date, A. W., *Analytic Combustion with Thermodynamics, Chemical Kinetics, and Mass Transfer*, (2011), Cambridge University Press.

[5] Turns, S. R., *An Introduction to Combustion, 2nd Ed.*, (2000), McGraw-Hill.

[6] Kim, C. S., Hong, S. D., Seo, D. U., and Kim, Y. W., "Temperature Measurement with Radiation Correction for Very High Temperature Gas", *Proceedings of the 14th International Heat Transfer Conference*, IHTC14-23074 (2010), Washington D.C.

[7] Brohez, S., Delvosalle, C., and Marlair, G., "A Two-Thermocouples Probe for Radiation Corrections of Measured Temperatures in Compartment Fires", *Fire Safety Journal*, Vol. 39 (2004), pp. 399–411.

[8] Takeno, T., Sato, K., and Hase, K. "A Theoretical Study on an Excess Enthalpy Flame", *Proceedings of Symposium (International) on Combustion*, Vol. 18, No. 1 (1981), pp. 465-472.

[9] Tsuji, H., Gupta, A. K., Hasegawa, T., Katsuki, M., Kishimoto, K., and Morita, M., *High Temperature Air Combustion: From Energy Conservation to Pollution Reduction*, (2003), CRC Press.

Chapter 4

Thermal Effects of Flame Shape and Location on Reforming Reaction Performance

4.1 Introduction

In the previous chapter, the basic reaction characteristics of POX were investigated regarding the equivalence ratio, ϕ, and reaction temperature. It was revealed that the reaction was optimized at $\phi = 3.5$ due to the trade-off relation between the methanol conversion ratio, α, and the preferential production ratio of H_2, β.

Following those results, we investigate the methanol POX reaction further to obtain knowledge on the POX flame structure when the ceramic honeycomb is thermally involved in the reaction. One of the most significant factors having an influence on the reforming reaction performance is the flame shape and its location relative to the ceramic honeycomb. Therefore, these factors are explored in this chapter, and the relation between the reforming performance and the thermal influences of the ceramic honeycomb is investigated.

Generally, when a porous material is involved in a combustion reaction, thermal interaction between the flame and solid surface of the porous material plays a significant role in the reaction characteristics [1,2]. In this case, several factors dominating the thermal structure of the reaction should be considered: Reaction heat release rate of the mixture

gas, equivalence ratio, mixture velocity distribution, thermal properties and dimensions of the porous material, and energy loss from the reaction region to the environment. In order to investigate the effect of the ceramic honeycomb on the POX flame and its reaction characteristics, several experiments regarding the above factors were conducted.

First, the stainless steel reactor, investigated in the previous chapter, was applied to the experiments in various thermal load conditions, q_{load}, (representing the mixture flow rates). Detailed temperature measurements and gas component analyses in various q_{load} were conducted in order to reveal the relation between the flame location and reaction performance. Through the study, the major influential factor of the flame on the reforming reaction performance in the stainless steel reactor was obtained.

In the stainless steel reactor, however, the reactor wall has a significant influence on the reaction where internal heat recirculation from the post-reaction region to the mixture gas was realized as discussed in Chap. 3. This internal heat recirculation causes a thermally two-dimensional structure of the flame. Therefore, in order to reduce the thermal effect of the reactor wall on the flame structure, a quartz glass reactor was also fabricated and the experiments in the same flow rate conditions as the stainless steel reactor were conducted. Much simpler thermal field was achieved in the quartz glass reactor, that help us to understand the thermal and flow effects on the flame shape and its location more in detail.

The quartz glass reactor also has a purpose to visualize the flame and to measure the velocity distributions. By the visualization of the flame, the flame shape was observed directly and it was clarified that the thermal interaction between the flame and honeycomb had a significant influence on the reaction performance. From these results obtained, the stability and reaction performance of the POX flame using ceramic honeycomb was summarized, and the factors which should be considered when designing a fuel reformer using a porous material are discussed.

4.2 Experimental Apparatus and Conditions

4.2.1 Stainless Steel Reactor

The stainless steel reactor used in this chapter is the same apparatus used in the previous chapter. Therefore, the components and the dimensions are referred to Sec. 3.2.

4.2.2 Quartz Glass Reactor

In addition to the previous stainless steel reactor, a quartz glass reactor having the similar dimensions was fabricated. By introducing this reactor, conduction through the reactor wall and radiation emission from the reactor inner wall surface could be reduced due to the lower thermal conductivity and emissivity of quartz glass. This enabled much simpler thermal structure within the reactor to realize. The quartz glass reactor also enabled the visualization of the flame. The shape and location of the flame were, therefore, observed easily by using this reactor.

Figure 4.1 shows the schematic and cross-sectional views of the quartz glass reactor. The evaporator and baffle plate in the upstream part of the fuel reformer was the same as the stainless steel reactor. In the same way as Chap. 3, the required amount of air and methanol were supplied to the evaporator through the mass flow controller and fuel injector, respectively. The evaporator was kept at 420 K same as in the stainless steel reactor case by the electric band heaters for the continuous evaporation of methanol and formation of the mixture gas.

The reactor was made of quartz glass having an inner diameter, length and thickness of $D_{\mathrm{qz}} = 36\,\mathrm{mm}$, 300 mm, and 3 mm, respectively. The inner diameter of the reactor, D_{qz}, is slightly smaller than that of the stainless steel reactor, $D = 36.7\,\mathrm{mm}$. The cross-sectional area of the quartz glass reactor is, therefore, 3.8 % smaller. The smaller cross-sectional area of the quartz glass reactor results in about 3.9 % larger velocity profiles. However, we considered this error to be negligibly small in the following discussion.

The origin of the x–r coordinate system was set at the outlet surface of the baffle plate

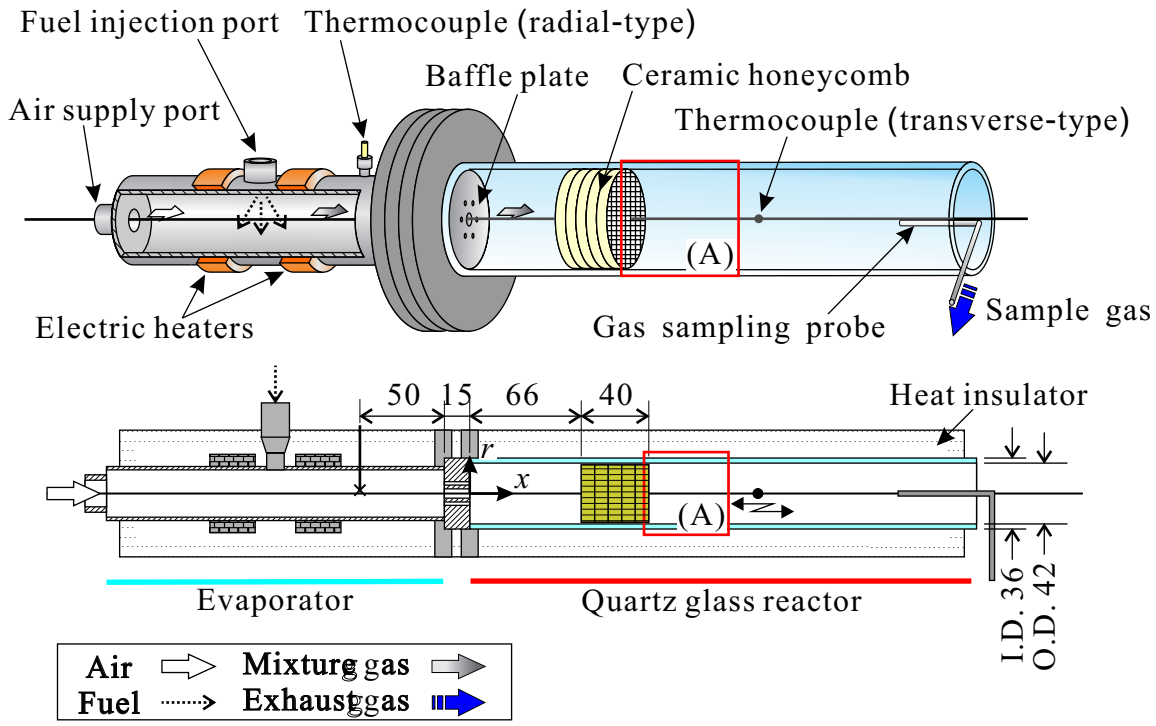

Figure 4.1: Schematic and cross-sectional views of the quartz glass reactor (unit: mm). Square (A) in the figure shows the observation region of the flame in photographs.

shown as Fig. 4.1. In the upstream region of the reactor, $1.74 \leq x/D_{\mathrm{qz}} \leq 2.83$, a ceramic honeycomb having a diameter and length of 34 mm and 40 mm, respectively, was inserted. The gap between the ceramic honeycomb and reactor inner wall was filled by silica tape in order to avoid undesired leakage of the mixture through the gap.

The outside wall of the quartz glass reactor was insulated by thermal insulator to minimize the effects of heat loss from the external wall surface of the reactor to the environment. The thickness of the insulator was about 40 mm. In the visualization experiments, however, the insulator was removed only at a necessary location temporarily (shown as a square (A) in Fig. 4.1).

4.2.3 Experimental Conditions

As discussed in the previous chapter, the POX flame can be stabilized in the vicinity of the ceramic honeycomb and sustained in a wide range of ϕ. In terms of the H_2 production, ξ_{H2}, the optimum reaction was realized in a slightly fuel-richer condition, $\phi = 3.5$, compared with the stoichiometry of POX, $\phi_{\mathrm{st}} = 3.0$. On the other hand, even in smaller ϕ, methanol conversion ratio, α, stayed at around 0.9 and did not reached unity. One of the major reasons of this phenomenon was believed to be the thermal interaction between the ceramic honeycomb and flame. Thus, in the following discussion, ϕ was fixed at 3.0 and 3.5, while thermal load, q_{load}, was varied to observe the flame structure and the stability of the reaction in various mixture flow rates. The relation of these factors to the reforming performance was also investigated.

Thermal load, q_{load}, was varied in a wide range in which the flame was formed in the vicinity of the ceramic honeycomb. The value of q_{load} was calculated based on the lower heating value (LHV) of methanol. Tables 4.1 and 4.2 show the volume flow rate conditions of fuel and air in the corresponding q_{load} of both $\phi = 3.0$ and 3.5 (PIV conditions are also shown, but explained in the next section). The value of $\dot{V}_{\mathrm{fuel}}$ represents the volume flow rate of liquid methanol, and $\dot{V}_{\mathrm{air}}$ is the volume flow rate of the air. The ratio of the total mixture flow rate to that in the smallest q_{load} of each ϕ is also shown in the same tables.

Table 4.1: Fuel and air flow rate conditions in the reforming experiment, and air flow rate conditions in the PIV measurement ($\phi = 3.0$).

q_{load} [kW]	$\dot{V}_{\mathrm{fuel}}$ [mL(liq.)/min]	$\dot{V}_{\mathrm{air}}$ [L/min]	Ratio [–]	Air flow rate (PIV) [L/min]	U_{m} [m/s]	Re_D [–]
0.37	1.40	1.93	1.00	4.09	0.06	89
0.53	2.04	2.81	1.46	5.96	0.09	130
0.64	2.43	3.35	1.74	7.10	0.11	154
0.84	3.21	4.42	2.30	9.39	0.15	204
1.04	4.00	5.50	2.85	11.68	0.18	254
1.45	5.56	7.65	3.97	16.25	0.25	353
1.76	6.73	9.26	4.81	19.68	0.30	427
2.12	8.10	11.15	5.79	23.68	0.37	514

Table 4.2: Fuel and air flow rate conditions in the reforming experiment, and air flow rate conditions in the PIV measurement ($\phi = 3.5$).

q_{load} [kW]	$\dot{V}_{\mathrm{fuel}}$ [mL(liq.)/min]	$\dot{V}_{\mathrm{air}}$ [L/min]	Ratio [–]	Air flow rate (PIV) [L/min]	U_{m} [m/s]	Re_D [–]
0.37	1.40	1.65	1.00	3.68	0.06	80
0.53	2.04	2.41	1.46	5.36	0.08	117
0.64	2.43	2.87	1.74	6.39	0.10	139
0.84	3.21	3.79	2.30	8.45	0.13	183
1.04	4.00	4.71	2.85	10.50	0.16	228
1.45	5.56	6.56	3.97	14.61	0.23	317
1.76	6.73	7.94	4.81	17.70	0.27	384
2.12	8.10	9.55	5.79	21.29	0.33	463

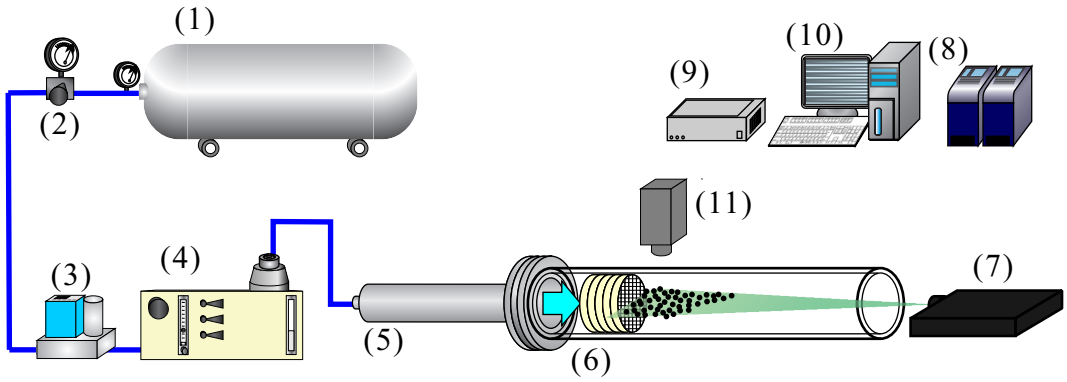

(1) Air compressor
(2) Pressure regulator
(3) Mass flow controller
(4) Particle generator
(5) Evaporator
(6) Test section
(7) Double-pulsed laser
(8) Laser oscillator
(9) Synchronizer
(10) PC
(11) CCD camera

Figure 4.2: Schematic diagram of the PIV measurement system.

4.2.4 PIV Measurement

In order to evaluate the flame shape and its stability in terms of the flow field, velocity distributions in the flame existing area was measured using the PIV method. It should be noted that the measurement was made in a non-combustion state, in which only air at room temperature was supplied to the reactor. Therefore, the influences of buoyancy and fluid property variation due to the temperature and gas component change were not considered. This may lead to some discrepancy with the practical flow field in a combustion state. However, we believe that the results will provide some insight into the understanding of the flow characteristics in the present fuel reformer.

The schematic view of the PIV measurement system is shown in Fig. 4.2. The PIV system is composed of a double-pulsed Nd:YAG Laser, CCD camera, and synchronizer. The laser light was introduced horizontally to the measurement area as a sheet form from the outlet of the reactor. This light sheet was aligned to the center axis of the reactor. The CCD camera was set above the reactor to obtain images of the measurement area from

the vertical direction. The timing of the laser oscillation and CCD camera exposure was synchronized by the synchronizer.

A particle generator (TSI; model #9306) was installed upstream of the reactor along the air supply path. A small amount of DEHS (Di-Ethyl-Hexyl-Sebacate, $C_6H_{50}O_4$) oil mist was supplied to the air as tracing particles. The nominal diameter of the oil mist was 1.0 μm.

The frame rate of the PIV measurement was 10 fps and a sufficient number of frames of the instantaneous particle images were taken to calculate the time mean velocity field. PIV analysis software (TSI; Insight Ver. 3.1) was used to obtain the flow velocity field from the images obtained.

The air flow rates of the PIV measurements are also shown in Tables 4.1 and 4.2. The air was introduced to the measurement section at a room temperature. The volume flow rate in the PIV measurement was set to the volume flow rate of the mixture at 420 K in the reforming experiment. The cross-sectional averaged flow velocity in the streamwise direction, $U_{\mathrm{x,m}}$, and the Reynolds number, Re_D, based on the inner diameter of the reactor, D_{qz}, was also shown in the same tables.

4.3 Results and Discussion

4.3.1 Effects of Thermal Load in Stainless Steel Reactor

This section discusses the effects of the thermal load, q_{load}, on the temperature profile and reaction characteristics in the stainless steel reactor. The experiments were conducted in various q_{load} conditions under two ϕs (ϕ = 3.0 and 3.5).

Temperature Distributions

Figure 4.3 shows the streamwise temperature distributions in q_{load} conditions varied from 0.37 kW to 2.12 kW. A hatched region corresponds to the location of Honeycomb A, and a horizontal broken line indicates the calculated value of the adiabatic flame temperature, T_{af}, with the initial temperature condition of 420 K.

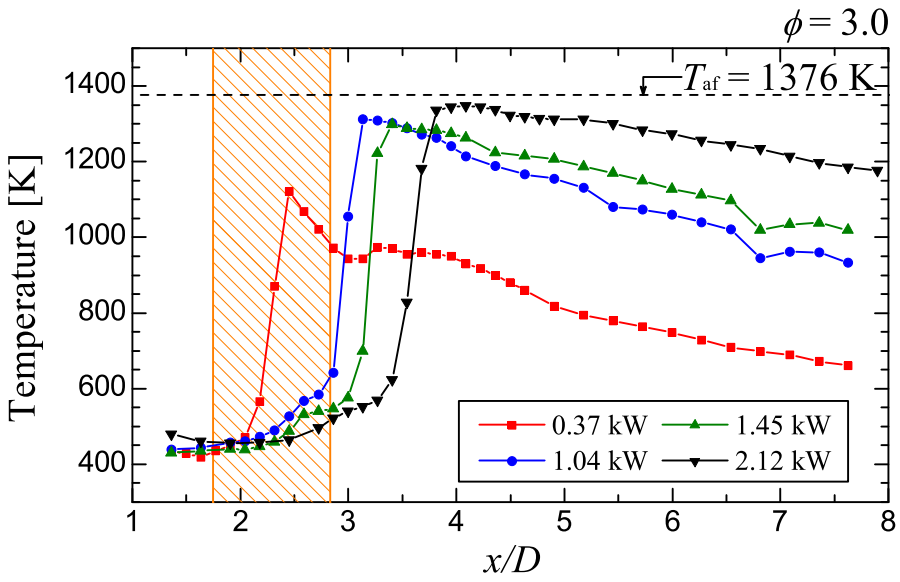

(a) $\phi = 3.0$

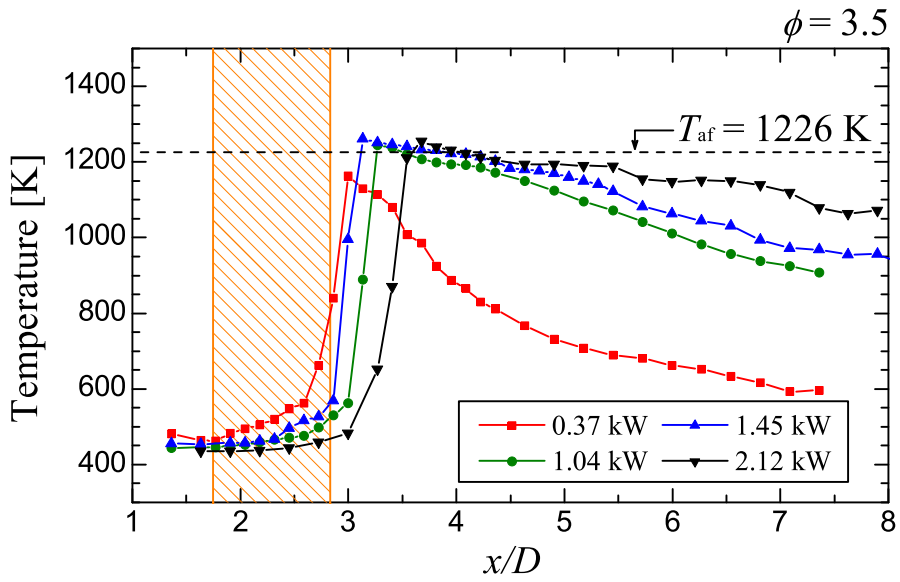

(b) $\phi = 3.5$

Figure 4.3: Streamwise temperature distributions in various q_{load} conditions in the stainless steel reactor.

First, in most of the q_{load} conditions of both $\phi = 3.0$ and 3.5, the maximum gas temperature, T_{max}, was observed at the outlet of Honeycomb A, which indicates that the flame was stabilized in the vicinity of Honeycomb A. On the other hand, the location of the temperature peak varies with respect to q_{load}.

In the cases when q_{load} is relatively large ($q_{\mathrm{load}} > 1\,\mathrm{kW}$), the value of T_{max} reached almost T_{af}. This indicates that the reaction occurred almost in an adiabatic condition.

The slope of temperature decrease in the downstream region of the reactor, $x/D > 4.0$, varies with q_{load}. In larger q_{load}, the slope of temperature decrease is smaller than that in smaller q_{load}. This is because the net heat release rate of the reaction increases with q_{load}. Thus, the heat loss from the exterior surface of the reactor to the environment becomes more significant in a smaller q_{load}. Therefore, the slope in the downstream region becomes smaller with an increase in q_{load}.

Figure 4.4 shows the location in both ϕ conditions where T_{max} was observed. The location where T_{max} was observed is expressed in the dimensionless form, $(x/D)_{T\mathrm{max}}$. The abscissa indicates q_{load} and the ordinate indicates $(x/D)_{T\mathrm{max}}$. The experiments were conducted several times in each q_{load} condition. In each figure, symbols $\times$ indicate the raw data for the respective experiments. In addition, the line and symbol plots indicate the averaged values of these experiments conducted in the same q_{load} conditions.

Figure 4.5 shows the maximum flame temperature, T_{max}, with respect to q_{load} in $\phi = 3.0$ and 3.5. The horizontal broken line in the figure indicates T_{af} in the respective ϕ conditions.

As shown in Fig. 4.4(a), in $0.64 \leq q_{\mathrm{load}} \leq 1.76\,\mathrm{kW}$ of $\phi = 3.0$, the flame stays at a constant location around $x/D = 3.5$, indicating that the stable reaction occurs at an almost-identical location in spite of the variation of q_{load}. In these conditions, T_{max} shown in Fig.4.5(a) slightly increased with a decrease in q_{load}. This slight increase in temperature is because of the enhancement of the preheating of the mixture gas. As q_{load} is decreased, indeed, the temperature measured at the downstream end of Honeycomb A ($x/D \approx 2.83$) increases (see Fig. 4.3(a)). This indicates that the preheating of the mixture is enhanced due to the flame existing close to the honeycomb, which causes the enhancement of the thermal

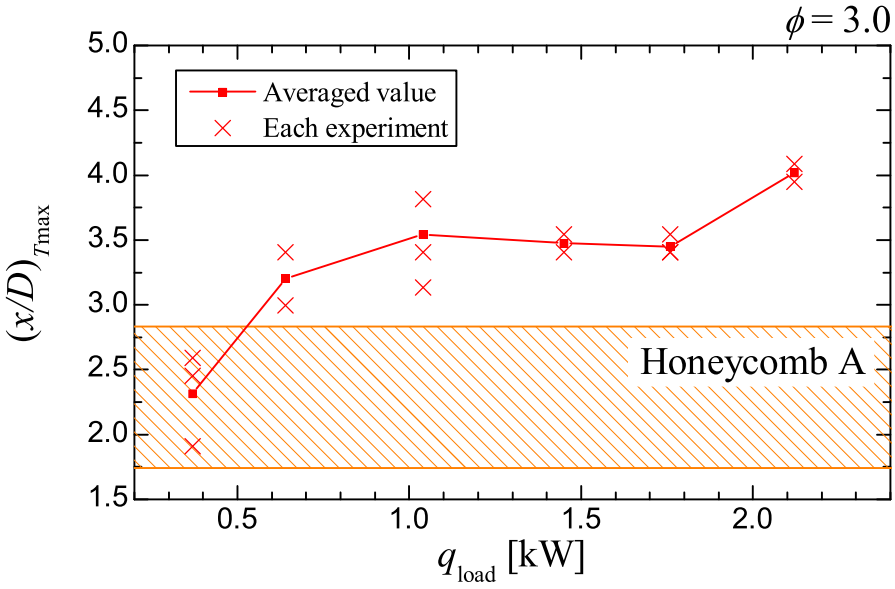

(a) $\phi = 3.0$

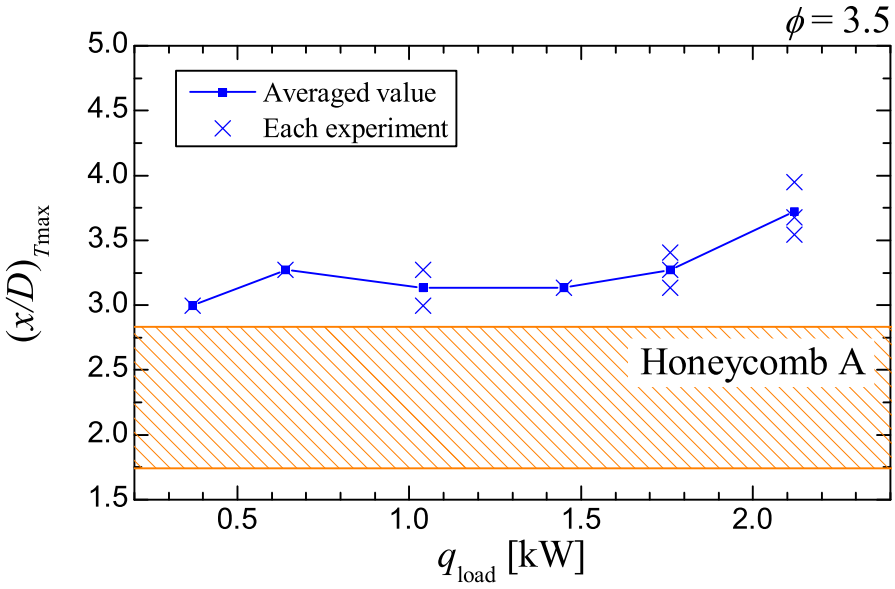

(b) $\phi = 3.5$

Figure 4.4: Location of the flame (stainless steel reactor).

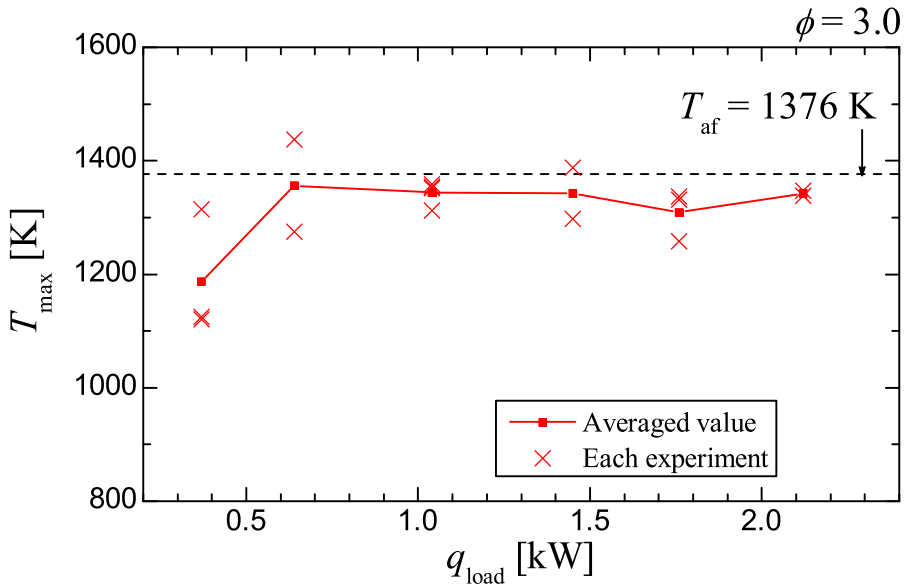

(a) $\phi = 3.0$

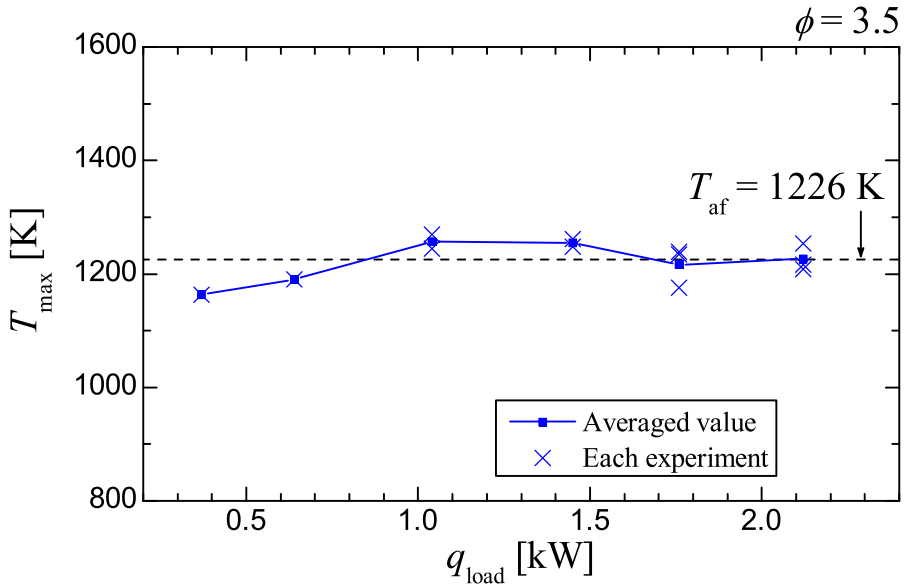

(b) $\phi = 3.5$

Figure 4.5: Measured maximum flame temperature (stainless steel reactor).

recirculation from the flame and post-reaction region to the honeycomb and mixture gas.

In the case of $\phi = 3.5$, the same trend could be seen. In Fig. 4.4(b), the flame stayed at around $x/D = 3.2$ in the conditions of $0.37 \leq q_{\mathrm{load}} \leq 1.76\,\mathrm{kW}$. The values of T_{max} corresponding to these q_{load} conditions shown in Fig. 4.5(b) stayed at around T_{af}, and slightly increased as q_{load} is decreased.

Secondary, in the case of $q_{\mathrm{load}} = 0.37\,\mathrm{kW}$ in $\phi = 3.0$, the flame moved into Honeycomb A, then T_{max} becomes much lower than the other q_{load} conditions. In addition, the secondary temperature peak in the downstream of Honeycomb A was observed (see Fig. 4.3(a)). This secondary peak is due to the secondary reaction taking place after the primary reaction took place within the honeycomb. The secondary reaction occurred because the primary reaction within Honeycomb A was incomplete due to the low temperature. Hence, the remaining reactant was consumed at the outlet of Honeycomb A, that produced the secondary temperature peak.

The reason why T_{max} decreases drastically when the reaction takes place within the honeycomb is the quenching effect of the solid surface of the honeycomb caused by the radiation loss. When the reaction takes place within the honeycomb, the heat release by the reaction is also used to heat up the solid phase of the honeycomb. The solid surface of the honeycomb, then, emits radiation and induces radiation flux toward the downstream region, which results in the additional energy loss. Detailed analysis of the radiation loss will be presented later.

In the smaller q_{load} condition ($q_{\mathrm{load}} < 0.64\,\mathrm{kW}$) in $\phi = 3.5$, T_{max} also observed the same slight decrease as $\phi = 3.0$ case. The flame in this case, however, did not move into the honeycomb. This is due to the relatively smaller heat release rate in $\phi = 3.5$ compared with that in $\phi = 3.0$. In the case of $\phi = 3.5$, the flame could not migrate into the honeycomb since the quenching effect of the honeycomb was large enough to prevent the flame from moving into the honeycomb and to keep the flame outside the honeycomb.

On the other hand, in $q_{\mathrm{load}} = 2.12\,\mathrm{kW}$ in both ϕ cases, the flame moved far downstream compared with the stable conditions of $0.64 < q_{\mathrm{load}} < 1.76\,\mathrm{kW}$. In this larger q_{load} condition,

however, $T_{\max}$ still stayed around the same level as the stable conditions of q_{load}. This behavior can be explained as "liftoff" of the flame from Honeycomb A. The reaction itself kept on at the same level as for the stable conditions, even though the flame moved downstream due to its large mixture velocity. The flame in much greater q_{load} conditions experienced "blowoff" in the present experimental apparatus.

Reaction Characteristics

Figures 4.6 and 4.7 show the fuel reformer evaluation parameters presented in Sec. 3.3 in both $\phi = 3.0$ and 3.5 cases. In $\phi = 3.0$ case, as long as the reaction was stabilized at the outlet of Honeycomb A ($q_{\text{load}} \geq 0.64\,\text{kW}$), the value of α did not change markedly and stayed at a constant level of 0.9. This is because $T_{\max}$ did not vary in these q_{load} conditions as shown in Fig. 4.5(a). The values of β and γ also stayed at almost-constant values in $q_{\text{load}} \geq 0.64\,\text{kW}$, respectively. This indicates that the reaction characteristics did not change because the same level of the flame temperature was achieved. The value of ξ_{H2} can be written as $2\alpha\beta$ (cf. Eq. (3.22)), both of α and β have an influence on ξ_{H2}. Thus, in $q_{\text{load}} \geq 0.64\,\text{kW}$, ξ_{H2} takes an almost-constant value in the same manner as α and β.

In the smaller q_{load} condition ($q_{\text{load}} < 0.64\,\text{kW}$), on the other hand, α deteriorated drastically. In this case, the reaction occurred within Honeycomb A as shown in Fig. 4.6(a), and $T_{\max}$ was considerably decreased below T_{af}. When the reaction takes place within the honeycomb, the thermal quenching effect of the honeycomb solid surface caused the decrease in $T_{\max}$ and the degree of the methanol decomposition reaction, which resulted in the reduction of α.

This thermal quenching effect of the honeycomb also had influences on the reaction characteristics represented by β and γ. In the case of $q_{\text{load}} < 0.64\,\text{kW}$, β decreased and γ increased slightly with a decrease in q_{load}. As in Refs. [3,4], the POX reaction is often summarized to have several reactions taking place simultaneously. Among these reactions, the WGS reaction is one of the major reaction, which has temperature-sensitive characteristic and relatively slow reaction speed. Thus, the reduction of the reaction

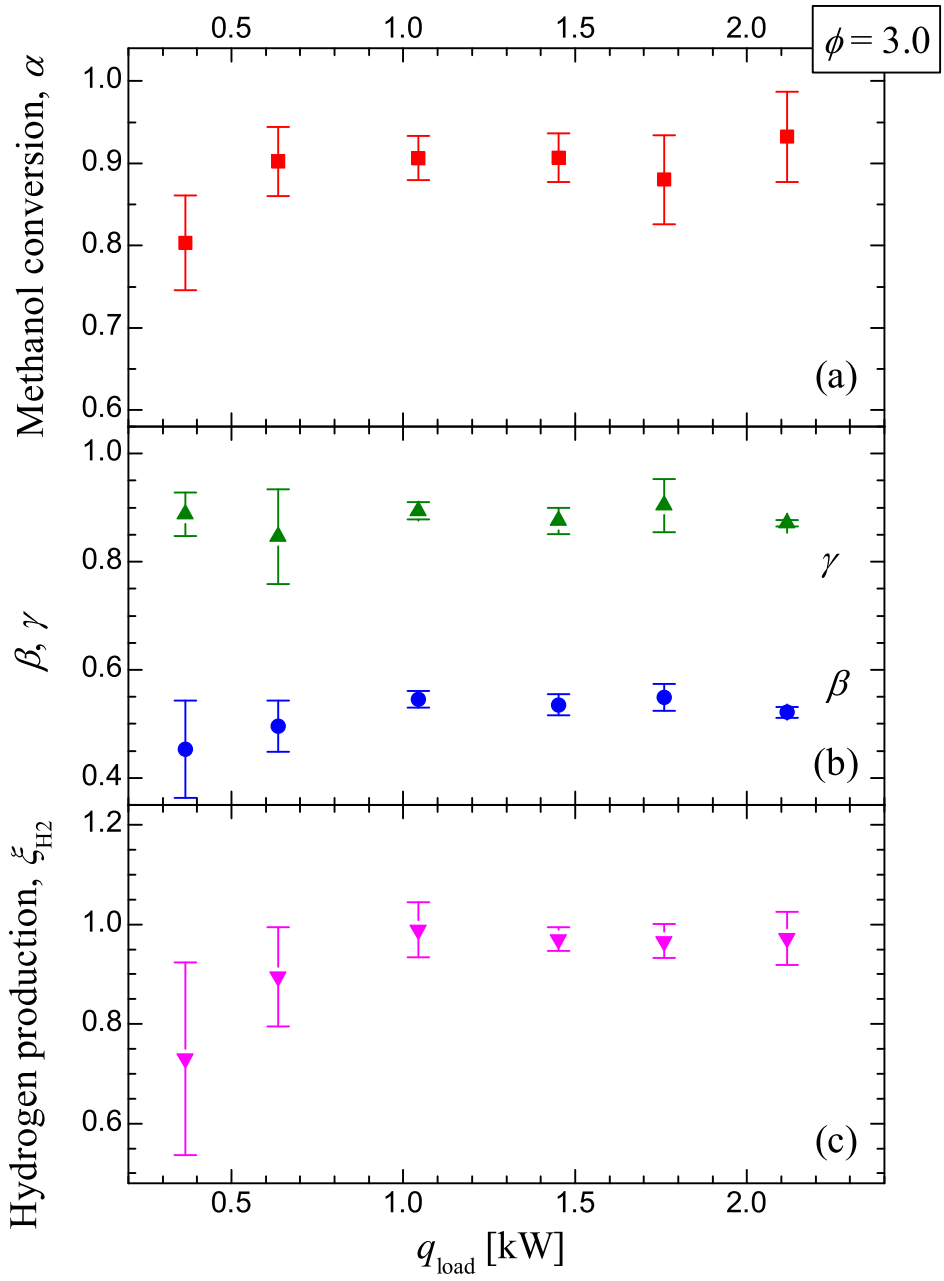

Figure 4.6: Reforming evaluation parameters in $\phi = 3.0$. (a) Methanol conversion ratio, α. (b) Preferential production ratios, β and γ. (c) Hydrogen production ratio, ξ_{H2}.

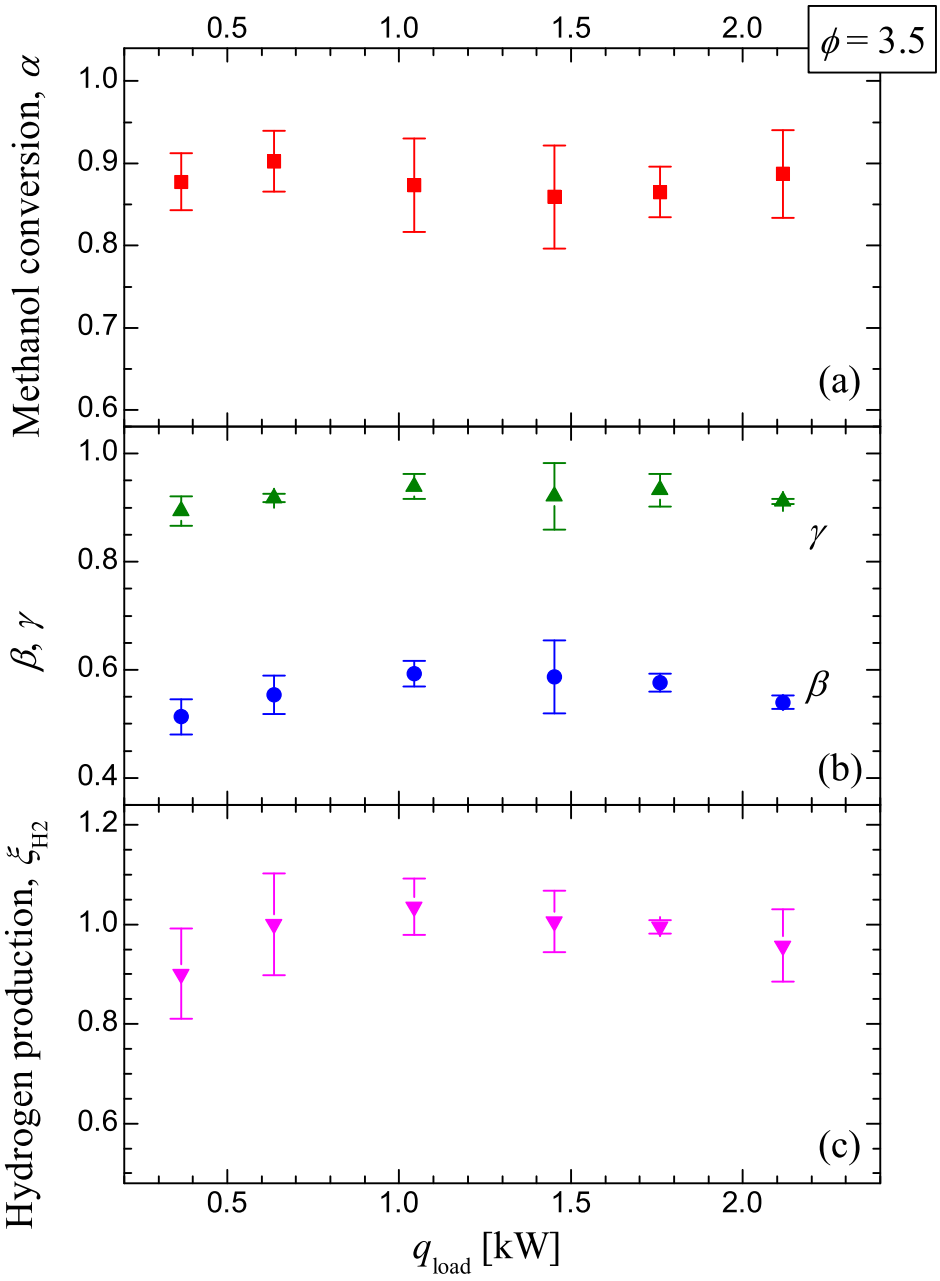

Figure 4.7: Reforming evaluation parameters in $\phi = 3.5$. (a) Methanol conversion ratio, α. (b) Preferential production ratios, β and γ. (c) Hydrogen production ratio, ξ_{H2}.

temperature caused the further slow down of the WGS reaction, and the products of the WGS reaction (H_2 + CO_2) were reduced. This may have caused the reduction of β and the increase in γ in smaller q_{load} conditions. By both of the reduction effects of α and β, the value of ξ_{H2} also experienced drastic deterioration in $q_{\mathrm{load}} < 0.64\,\mathrm{kW}$.

The error bar of ξ_{H2} in $q_{\mathrm{load}} < 0.64\,\mathrm{kW}$ conditions in $\phi = 3.0$ is much larger than the other conditions. This is due to the unstableness of the flame location in this q_{load}. As shown in Fig. 4.6(a), the flame locations in $q_{\mathrm{load}} = 0.37\,\mathrm{kW}$ varied from the upstream surface to the downstream surface of Honeycomb A. In $q_{\mathrm{load}} = 0.64\,\mathrm{kW}$, the flame is located very close to the honeycomb and the quenching effect produces the unstableness of the flame. This unstable characteristic of the flame in lower q_{load} conditions caused larger error bar than those in larger q_{load} when the reaction occurred outside the honeycomb.

In $\phi = 3.5$, shown in Fig. 4.7, the value of α stayed at a constant value of 0.85 in the whole range of q_{load}. In this case, α did not decrease even in $q_{\mathrm{load}} = 0.37\,\mathrm{kW}$. As shown in the distribution of $(x/D)_{T\mathrm{max}}$ (see Fig. 4.4(b)), the flame of $\phi = 3.5$ did not move into the honeycomb. This enabled the reaction to keep relatively high α even in the smallest q_{load} condition. The value of α in $\phi = 3.5$ in $q_{\mathrm{load}} = 0.37\,\mathrm{kW}$ is conversely higher than that in $\phi = 3.0$. This indicates that the quenching effect of the honeycomb in $q_{\mathrm{load}} = 0.37\,\mathrm{kW}$ of $\phi = 3.5$ is smaller than that in $\phi = 3.0$.

The values of β and γ in $\phi = 3.5$ also experienced almost-constant values in the whole range of q_{load}. Due to these constant feature of α and β, the deterioration of ξ_{H2} was smaller than for $\phi = 3.0$. This is because the flame barely stayed at the outlet of Honeycomb A even in the smallest q_{load}.

Based on these results, it was found that a robust reaction can be achieved by the ceramic honeycomb. However, it should be noted that the reaction temperature may be drastically decreased due to the direct interaction between the flame and the ceramic honeycomb when the reaction takes place very close to or within the ceramic honeycomb. Especially in smaller ϕ and q_{load} conditions, the flame tends to move into the honeycomb. Thus, it is important to set an appropriate ϕ and q_{load} conditions to operate the highly

efficient POX reaction in the honeycomb-type fuel reformer.

In order to attain the optimum operating condition, one can choose both conditions of ϕ and q_{load}. When the amount of hydrogen needed is very small, it is reasonable to reduce q_{load}. However, the reduction of q_{load} leads the deterioration of α (see Fig. 4.6). To avoid this deterioration of α, one can increase ϕ at the same time to reduce the quenching effect of the ceramic honeycomb. By utilizing these two degrees of freedom, a flexible reforming condition can be achieved in the present fuel reformer.

4.3.2 Reforming Experiments in Quartz Glass Reactor

Temperature Distributions

In this section, the experimental results of the quartz glass reactor are presented, and the differences from the stainless steel reactor are discussed. By the comparison between the results of these two reactors, the thermal characteristics of the reactors involving the reactor material characteristics such as thermal conductivity and radiation emissivity can be separated from the effect of the ceramic honeycomb. This enables the thermal effect of the ceramic honeycomb to be evaluated more accurately.

Figure 4.8 shows the temperature distributions in the quartz glass reactor in $\phi = 3.5$. The flame locations, $(x/D_{\mathrm{qz}})_{T\mathrm{max}}$, are also shown in Fig. 4.9 compared with the results in the stainless steel reactor. The flame with steep temperature gradients were also formed in the vicinity of the ceramic honeycomb. However, T_{max} in the quartz glass reactor was higher than that in the stainless steel reactor when the flame was formed close to the ceramic honeycomb ($q_{\mathrm{load}} \leq 0.64\,\mathrm{kW}$). This increase in T_{max} is due to the insulation effect of quartz glass which has much smaller thermal conductivity than stainless steel.

As shown in Fig. 4.9, the flame in the quartz glass reactor is formed in more downstream than that in the stainless steel reactor in $q_{\mathrm{load}} > 1\,\mathrm{kW}$. In smaller q_{load} conditions, on the other hand, the trend of the flame location goes in reverse. This reverse in trend is due to the fact that the flame location is determined by the balance of the thermal effects of

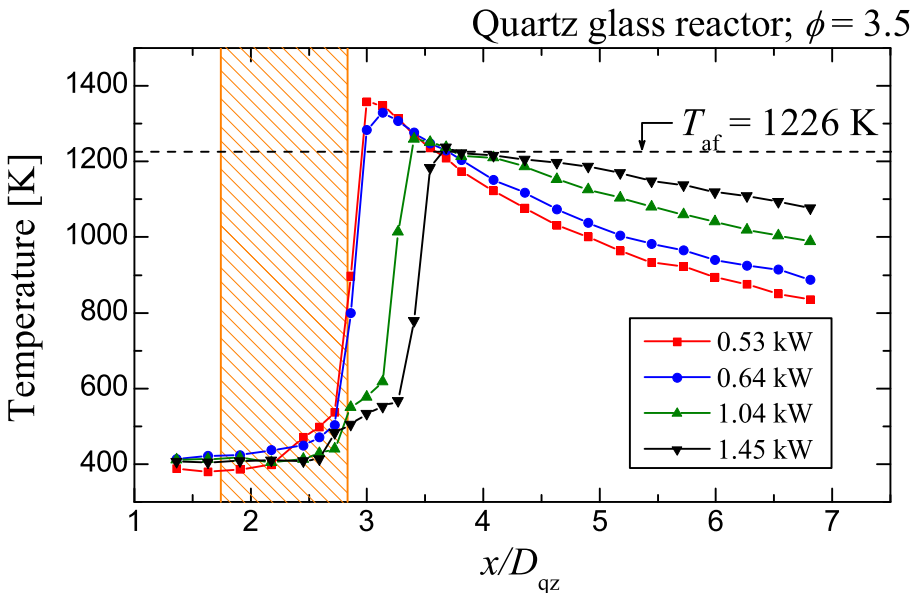

Figure 4.8: Streamwise temperature distributions in quartz glass reactor ($\phi = 3.5$).

quartz glass in the following two ways.

First, the thermal conductivity of stainless steel is about 20 W/(m·K), while that of quartz glass is about 1.4 W/(m·K) [5]. This implies that the conduction heat flux in quartz glass is 1/14 smaller than in the stainless steel in the same temperature gradient. In addition, the emissivity of quartz glass is much smaller than stainless steel, therefore, the radiation emission from the reactor inner wall is much smaller in the quartz glass reactor. Therefore, the energy recirculation from the post-reaction region to the ceramic honeycomb and to the unburned mixture through the reactor wall conduction and thermal radiation is much smaller in the quartz glass reactor. This reduces the extent of preheating of the mixture, resulting in the flame location to be moved downstream.

On the other hand, in the quartz glass reactor, the heat loss from the ceramic honeycomb to the exterior in a radial direction becomes small due to the lower thermal conductivity of quartz glass. This causes the ceramic honeycomb to be insulated and higher temperature of the ceramic honeycomb to be realized. Thus, by this insulation effect, the flame location can be moved upstream.

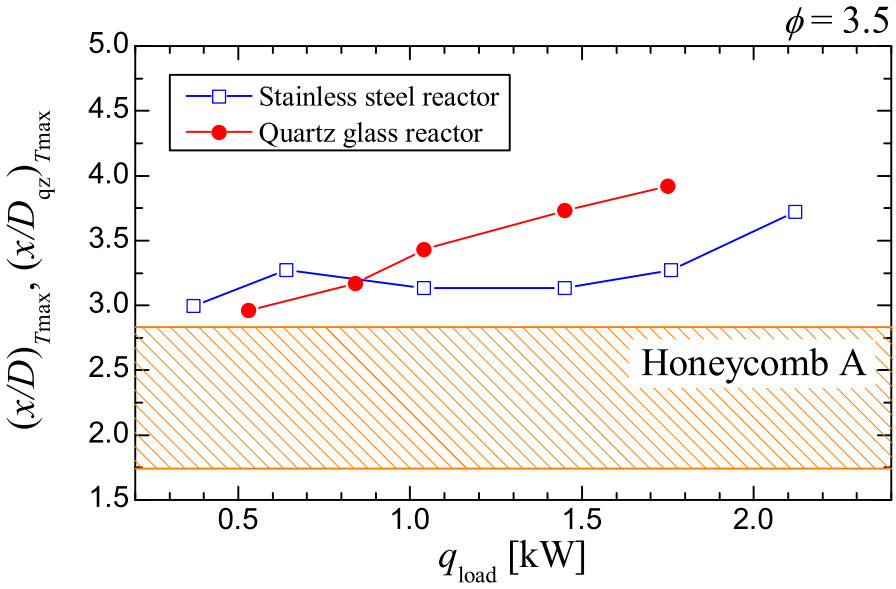

Figure 4.9: Comparison of the flame locations between quartz and stainless steel reactors ($\phi = 3.5$).

The above two thermal effects of the quartz glass reactor are balanced according to the flame location in the reactor. In the case when the flame is formed close to the ceramic honeycomb, the temperature of the ceramic honeycomb becomes high. In this case, the latter effect of the thermal insulation becomes dominant, so that the flame is formed closer to the honeycomb than in the stainless steel reactor.

When the flame is formed at a distance from the honeycomb, the reduction of the thermal recirculation by conduction heat transfer through the reactor wall dominates the flame formation, so that the flame moved downstream compared with the stainless steel reactor. By these characteristics of thermal balance, the trend of the flame location was determined by q_{load}.

On the qualitative discussion, in either case, both of these reactors have the same tendency that the flame moves close to the honeycomb with a decrease in q_{load}. However, as shown in Fig. 4.9, the flame location in the quartz glass reactor is more sensitive to q_{load} and the effect of the thermal interaction between the flame and the honeycomb is more remarkable than that in the stainless steel reactor.

Reaction Characteristics

Figure 4.10 shows the reforming evaluation parameters in the quartz glass reactor operated under $\phi = 3.5$. For comparison, the results of the stainless steel reactor are also plotted in each figure.

First, in Fig. 4.10(a), though α takes an almost-constant value in the stainless steel reactor, the quartz glass reactor observes the deterioration of α in $q_{\mathrm{load}} < 1.0\,\mathrm{kW}$ conditions. This deterioration in a smaller q_{load} conditions was caused by the upstream transition of the flame due to the insulation effect of the quartz glass reactor. As mentioned in the previous section, the adiabatic nature of quartz glass increases the effect of the interaction between the flame and the ceramic honeycomb. Thus, the quenching effect of the ceramic honeycomb was observed in a wider range of q_{load} conditions in the quartz glass reactor than the stainless steel reactor.

The values of β and γ, on the other hand, decreased slightly in the whole experimental range of q_{load} compared with the stainless steel reactor. The decrease in β and γ was about 10 % and 5 % at the maximum, respectively. The decrease of these two parameters are not significant compared with the deterioration of α.

In the quartz glass reactor, α and β in the smaller q_{load} conditions were smaller than that in the stainless steel reactor. Therefore, the overall hydrogen production ratio, ξ_{H2}, was also reduced in smaller q_{load} conditions. In the smallest q_{load} condition, the value of ξ_{H2} was deteriorated in about 40 % compared with larger q_{load} conditions in the quartz glass reactor, or with the same q_{load} condition of the stainless steel reactor.

By comparing the reforming evaluating parameters in both reactors, the quenching effect of the ceramic honeycomb became remarkable especially in smaller q_{load} conditions in the quartz glass reactor. In larger q_{load} conditions, on the other hand, the reaction characteristics represented by these evaluation parameters basically agreed with each other. Thus, the basic reaction characteristics were not so much different between these two reactors in the present experimental conditions. Therefore, the phenomena observed in the stainless steel reactor can also be explained qualitatively by the observation of the

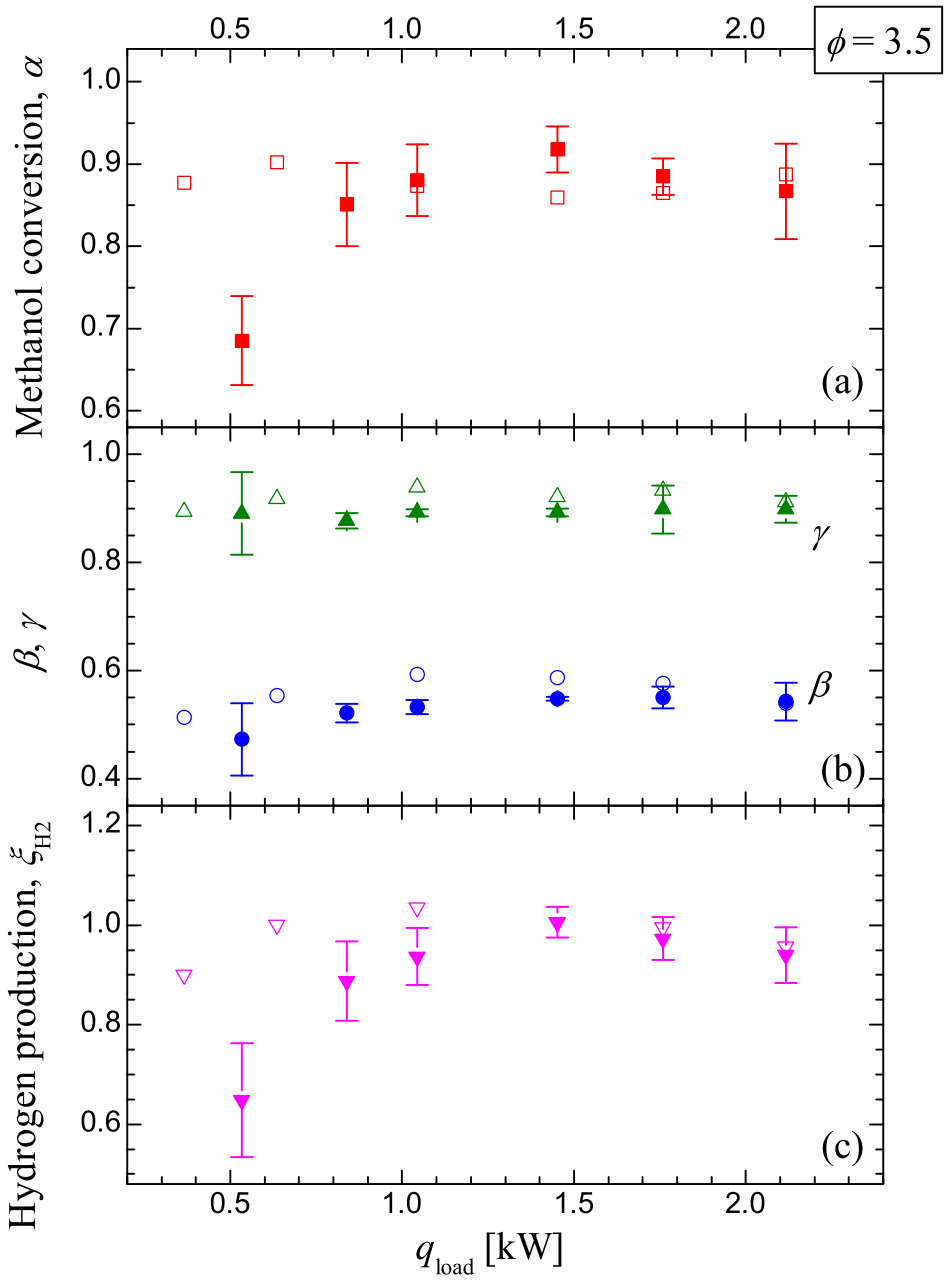

Figure 4.10: Comparison of reforming evaluation parameters between stainless steel reactor (open symbols) and quartz glass reactor (solid symbols) in $\phi = 3.5$. (a) Methanol conversion ratio, α. (b) Preferential production ratios, β and γ. (c) Hydrogen production ratio, ξ_{H2}.

quartz glass reactor.

In the following section, the relation between the flame shapes and the velocity distributions are considered in the quartz glass reactor. By the visualization of the flame and the measurement of the velocity distributions, the interaction between the flame and the ceramic honeycomb are observed and the reaction characteristics of the POX reaction using the ceramic honeycomb are presented.

Flame Shape and Velocity Distribution (Quartz Glass Reactor)

Figure 4.11 shows the direct images of the flame in each q_{load} condition of $\phi = 3.5$. The outlines of the reactor wall and ceramic honeycomb, and the locations of the flame front identified by the author's observation are indicated as solid lines in the images. Three kinds of flame shapes were observed. First in Fig. 4.11(a), the flame attaches to the outlet surface of the honeycomb except for the center region where the flame has a convex surface. In Fig. 4.11(b) and (c), on the other hand, the flame forms a conical shape with the base of the cone attached to the honeycomb outlet in the near-wall region. In these two conditions, the flame forms a slight asymmetric shape having the tip of cone hanging down. This is due to the effect of buoyancy. Since the cold premixed gas has higher density than the high temperature reforming gas, which results in the movement of the flame tip in the downward direction. Figures 4.11(d)–(f) show liftoff flames having non-axisymmetric shapes. It will be explained later in detail how the flame shapes are determined like these three patterns using the velocity distributions by PIV measurements.

Figure 4.12 shows the streamwise velocity distribution of each q_{load} condition in the non-combustion field (PIV experiment). The velocity distributions were calculated by the arithmetic averaging of the data obtained in the region of $3.1 < x/D_{\mathrm{qz}} < 3.38$.

All the distributions in Fig. 4.12 have peaks at the center region and have shoulder-like shape in the outer region ($0.2 < r/D_{\mathrm{qz}} < 0.3$). These distributions may be caused by the dimensions and the configuration of the holes opened on the baffle plate.

In Fig. 4.11, the calculated flame shapes are also shown as broken lines in the small

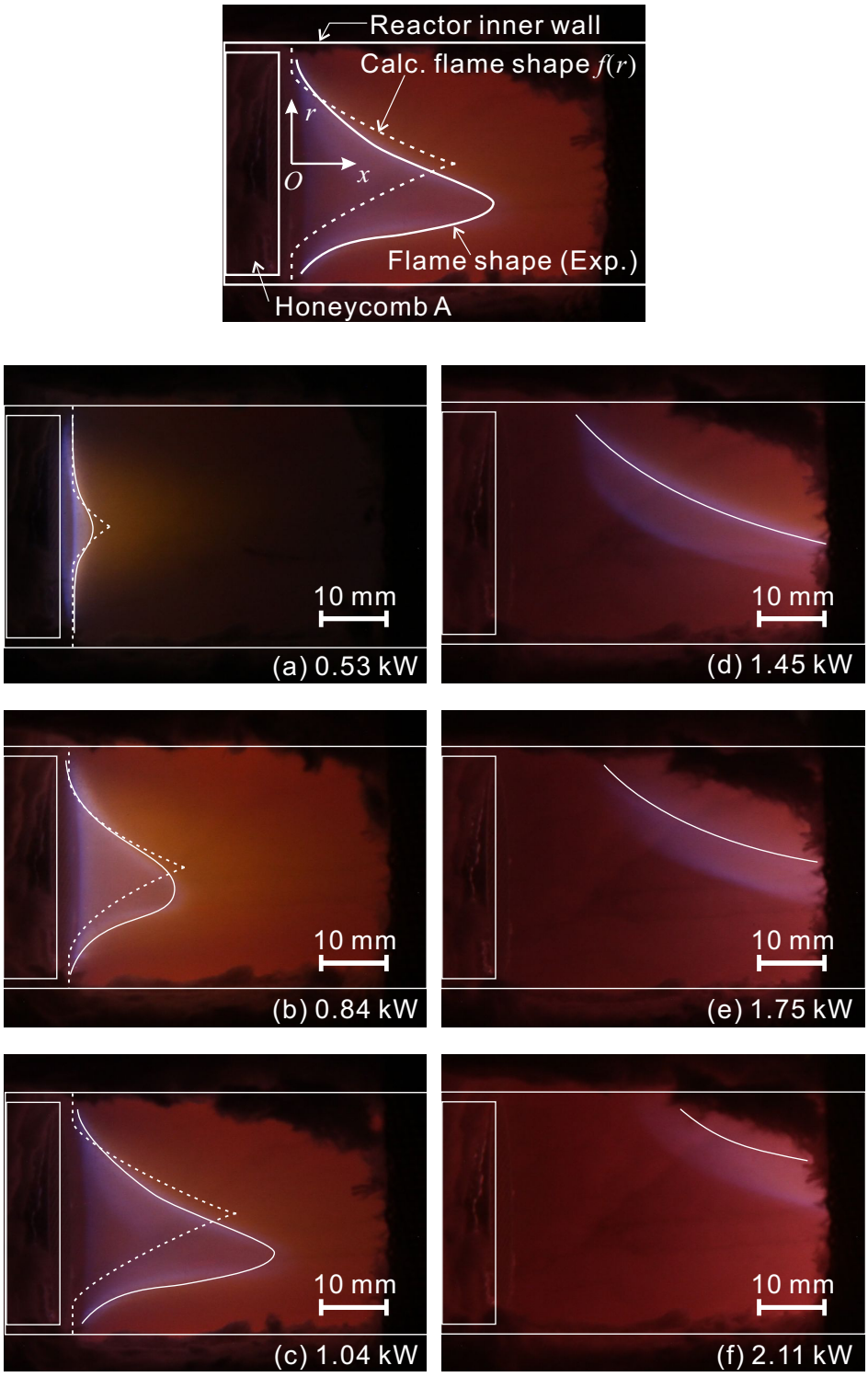

Figure 4.11: Direct images of the flame ($\phi = 3.5$).

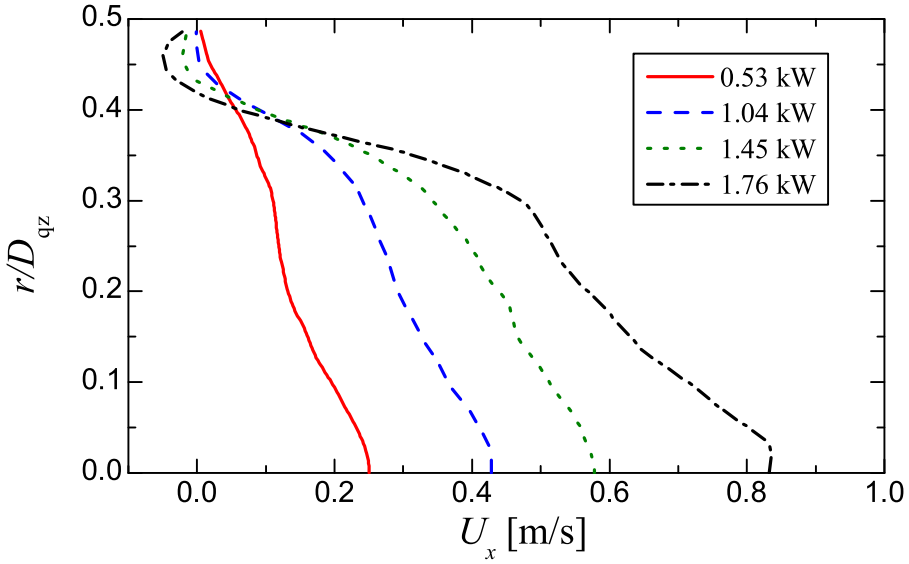

Figure 4.12: Velocity distributions in non-combustion field.

q_{load} conditions. The flame shapes were calculated by the measured velocity balancing with the laminar burning velocity, S_{L}. The value of S_{L} was assumed to be 0.15 m/s, referred to Ref. [6]. The flame was assumed to be stabilized having a certain inclination angle to the orthogonal plane to the center axis of the reactor, $\theta(r)$, by which S_{L} balanced with the normal component to the flame surface of the mixture velocity as

$$U_x(r)\cos\theta(r) = S_{\mathrm{L}}. \tag{4.1}$$

The inclination angle, θ, is calculated readily as

$$\theta(r) = \begin{cases} 0 & (S_{\mathrm{L}} > U_x(r)) \\ \cos^{-1}\left[S_{\mathrm{L}}/U_x(r)\right] & (S_{\mathrm{L}} \leq U_x(r)) \end{cases} \tag{4.2}$$

Note that the flame was assumed to attach to the honeycomb where the mixture velocity was less than S_{L}. The streamwise distance of the flame from the honeycomb outlet surface

at $r = r'$, $f(r')$, can be calculated by an integral form:

$$f(r') = \int_{R_{\mathrm{qz}}}^{r'} \tan\theta(r) dr, \tag{4.3}$$

where R_{qz} denotes the radius of the reactor.

The calculated flame shapes agree well with the experiments in the conditions when the conical flames were observed. These results show that the flame of the POX reaction is predominated by the velocity profile in the reaction region. Thus, it is meaningful to estimate the flame shape and the reaction performance on the basis of the velocity profiles in the reactor in the following discussion.

Integrating both of the results in Figs. 4.11 and 4.12, the thermal and flow characteristics can be summarized as follows:

In $q_{\mathrm{load}} = 0.53\,\mathrm{kW}$, the flame was attached to the honeycomb except for the center region. This is because the mixture velocity balanced with S_{L} in the broad outer region of the reactor, so that the flame was stabilized at the adjacent region to the honeycomb outlet. As shown in the velocity distribution, indeed, the streamwise velocity is 0.1–0.15 m/s in the outer region. In the near-wall region, on the other hand, U_x is much smaller than S_{L}. The flame in this region is estimated to migrate into the honeycomb or to experience a backfire considering only the balance of U_x and S_{L}. However, a stable flame could be obtained even in this region. This is explained by the heat loss by the conduction heat transfer and the thermal radiation. When a solid surface exists close to the flame, the reaction heat is removed by the solid surface and the burning velocity is reduced. This heat loss from the flame is believed to cause the deterioration of the reforming performance. The radiation energy loss will be estimated in the next section. This near-wall region worked as the attachment point of the flame due to the balance between U_x and the reduced burning velocity. In the experiment, when q_{load} was set below 0.53 kW, the flame moved into the honeycomb eventually.

Next, in $q_{\mathrm{load}} = 0.84$–$1.04\,\mathrm{kW}$, even though the velocity gradient in the outer region was increased, there still existed a low-velocity region at around $0.4 < r/D_{\mathrm{qz}} < 0.5$. This

region worked as a flame attachment point, by which the flame could be kept from liftoff or blowoff. In the center region, on the other hand, the streamwise velocity was larger than S_{L}, therefore, the conical flame was stabilized.

In further higher thermal load conditions, $q_{\mathrm{load}} \geq 1.45\,\mathrm{kW}$, there is a backflow observed in the near-wall region. This backflow was caused by the configuration that the 34 mm honeycomb in diameter was inserted in the 36 mm reactor in inner diameter. The gap between the honeycomb and the reactor inner wall worked as a backward-step-like configuration for the flow. However, the effect of this backward step was limited only in the narrow region near the wall, so that the backflow did not have a stabilizing effect on the flame. In the meanwhile, since the reactor was installed horizontally, the flame experienced liftoff easier in the lower part of the reactor due to the larger heat loss effect by the natural convection around the reactor. Therefore, the flame was lifted off from the lower part of the honeycomb and stretched as a non-axisymmetric shape.

The attachment point in the upper region moved downstream as q_{load} was increased. This movement of the attachment point was caused by the larger velocity gradient in the near-wall region in the larger q_{load} conditions. When q_{load} is increased, the velocity gradient in near-wall region is also increased, which causes a liftoff of the flame. By both of these effects by the velocity gradient and the heat loss, the flame was first lifted off in the lower part, then the flame in the upper attachment point also experienced liftoff, by which the attachment point migrated downstream gradually. By increasing q_{load} beyond 2.11 kW, the flame was blown off completely.

Radiation Loss and Its Influence on Reaction

In the above discussion, the reason of the deterioration of methanol conversion ratio in the lower q_{load} condition was explained by the energy loss by radiation emission. When the POX flame attached to the outlet surface of the ceramic honeycomb, the temperature of the solid phase of the ceramic honeycomb increases, and the thermal radiation from the ceramic surface to the downstream region may increase. In this section, the thermal

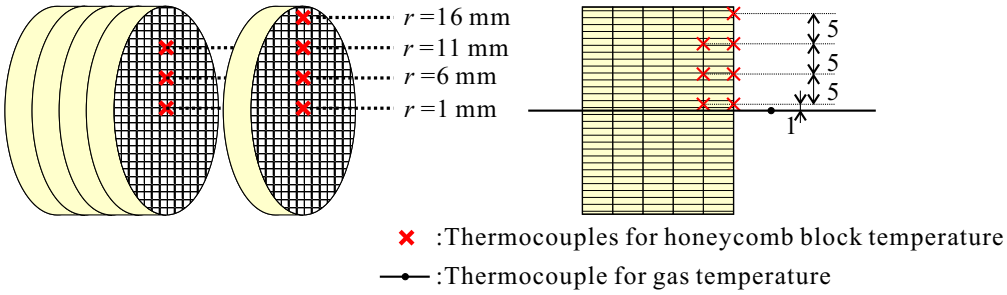

Figure 4.13: Temperature measurement points of the solid surface of the ceramic honeycomb.

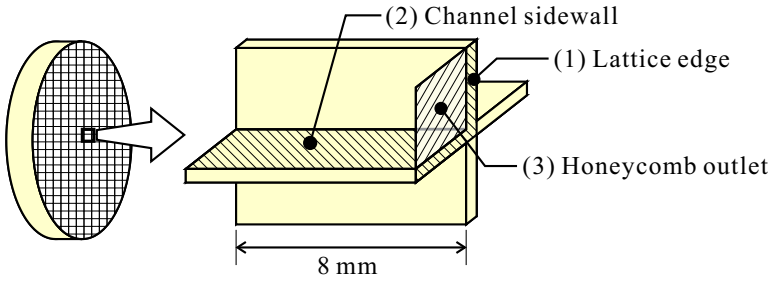

Figure 4.14: Surfaces involved in the radiation emission from the honeycomb.

radiation emitted from the ceramic honeycomb will be calculated from the measured solid temperatures, and the effect of the radiation loss on the reaction will be estimated.

First, the temperature measurement and the calculation methods of radiation loss are explained. The measurement of the solid surface of the ceramic honeycomb was conducted at seven locations shown in Fig. 4.13. The bare bead of the 0.1-mm thermocouple wires were attached at the shown locations. The radial location of each measurement point was $r = 1$, 6, 11, 16 mm, respectively.

Next, the emissive power from the honeycomb solid surface was modeled as follows. By a rough calculation, more than 99 % of the radiation energy emitted to the downstream region of the honeycomb was originated from the last 8 mm end part of Honeycomb A. Thus, only the region of $2.62 < x/D_{\mathrm{qz}} < 2.83$ was considered to calculate the radiation loss.

A single unit of the honeycomb lattice shown in Fig. 4.14 was considered. Each

solid surface was numbered and named as (1) lattice edge, (2) channel sidewall, and (3) honeycomb outlet (virtual surface for the consideration of the view factor). The dimensions were previously shown in Fig. 4.1. The view factor $F_{i,j}$ is defined as the fraction of the radiation leaving surface i that is intercepted by surface j. In this case, the view factor from surface 2 to surface 3 is $F_{2,3} = 0.0387$ [7].

The total emissive power from (1) lattice edge, q_1, and (2) channel sidewall, q_2, are written as

$$q_i = \varepsilon_{\text{ceram}} \sigma T_i^4 A_i \quad (i = 1, 2) \tag{4.4}$$

where T_i is the solid temperature of surface i, $\varepsilon_{\text{ceram}}$ is the emissivity of the ceramic, and σ is Stefan-Boltzmann constant. The total radiation flux through the downstream cross-section of Honeycomb A, q_{rad} is

$$q_{\text{rad}} = \sum_{\text{mesh}} (q_1 + 4 q_2 F_{2,3}). \tag{4.5}$$

The second term is multiplied by four, since the honeycomb channel is confined by four sidewalls. The radial distribution of the solid temperature was interpolated from the measured results.

The radiation loss from the surface of the honeycomb is actually affected by the irradiation from the downstream reactor wall surface. In the experiment, the inner wall temperature may around 800 K, which in turn emits radiation and causes the heat up of the honeycomb. In rough calculation, the reactor wall within 50 mm from Honeycomb A (assume temperature to be 800 K and emissivity of quartz to be 0.7) cause the irradiation to the downstream cross-section of Honeycomb A, and the irradiation was calculated about 14 W. This value is not negligible compared with the radiation loss from Honeycomb A. However, since the reactor inner wall temperature distribution close to Honeycomb A does not change markedly with q_{load}, the irradiation from the reactor wall does not change a lot with respect to q_{load}. Therefore, in the following discussion, only the radiation emission

Table 4.3: Parameters for radiation analysis.

$F_{2,3}$	σ [W/(m^2·K^4)]	$\varepsilon_{\mathrm{ceram}}$	$\varepsilon_{\mathrm{qz}}$
0.0387	5.67×10^{-8}	0.5	0.7

from Honeycomb A, q_{rad}, is considered as the radiation loss.

To evaluate the radiation loss quantitatively, the theoretical value of the heat release rate of the POX reaction, q_{POX}, was calculated and compared with q_{rad}. The value of q_{POX} was calculated based on the equilibrium composition in $\phi = 3.5$. The ratio of q_{rad} to q_{POX} is defined as radiation loss rate, L_{rad}. Since the emissivity is very sensitive to the composition and surface structure of the material, the value of emissivity for the present material was not available, thus typical values of the corresponding materials are chosen [7,8]. The parameters related to the radiation analysis are presented in Table 4.3.

Figure 4.15 shows the radial temperature distributions of the honeycomb solid surface. The temperatures of the honeycomb solid surface are high in all q_{load} conditions at around $r/D_{\mathrm{qz}} = 0.3$ which corresponds to the flame attachment point.

In $q_{\mathrm{load}} = 0.53\,\mathrm{kW}$, the flame was attached to the honeycomb as shown in the visualization results. Therefore, the solid surface temperature at $0.3 < r/D_{\mathrm{qz}} < 0.4$ was extremely high compared with the other q_{load} conditions. In this lower q_{load} condition, very stable flame was achieved due to the high temperature solid surface of the honeycomb.

However, as reported in Refs. [9,10], the flame temperature decreases when the flame is located in the vicinity of a porous material because the high temperature solid surface emits thermal radiation to the downstream region which causes heat loss from the flame. In Fig. 4.8, on the other hand, the maximum temperature increased with a decrease of q_{load}. This is due to the radial heat flux effect. At the center region of the honeycomb, the flame was formed at a distance from the honeycomb, by which the honeycomb temperature was decreased. However, in the outer region, where the flame was attached to the honeycomb, high temperature honeycomb surface was realized. This temperature difference between the outer region and the center region induced the radial heat flux from the outer region to

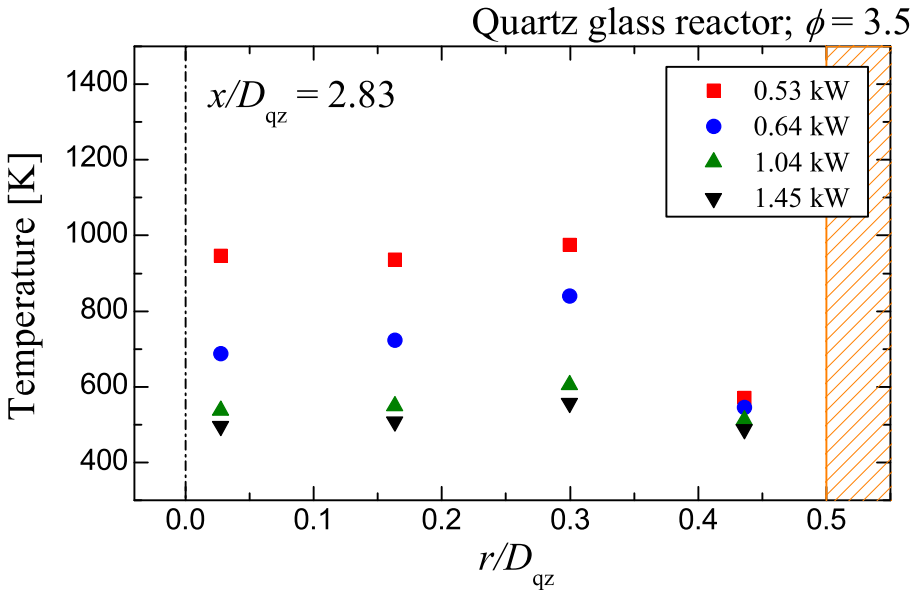

(a) At downstream surface of Honeycomb A, $x/D = 2.83$

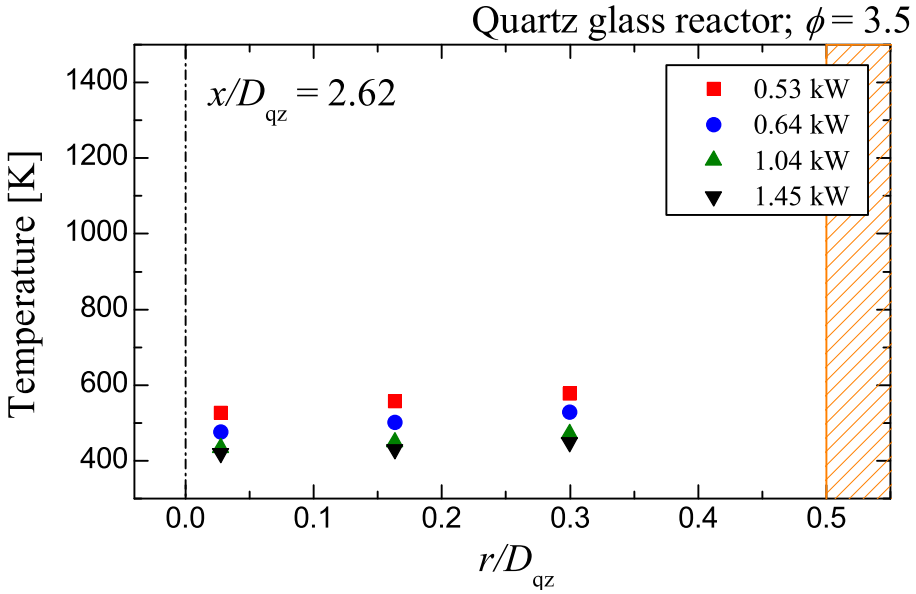

(b) 8 mm upstream of the honeycomb outlet, $x/D = 2.62$

Figure 4.15: Radial temperature distributions of the ceramic honeycomb.

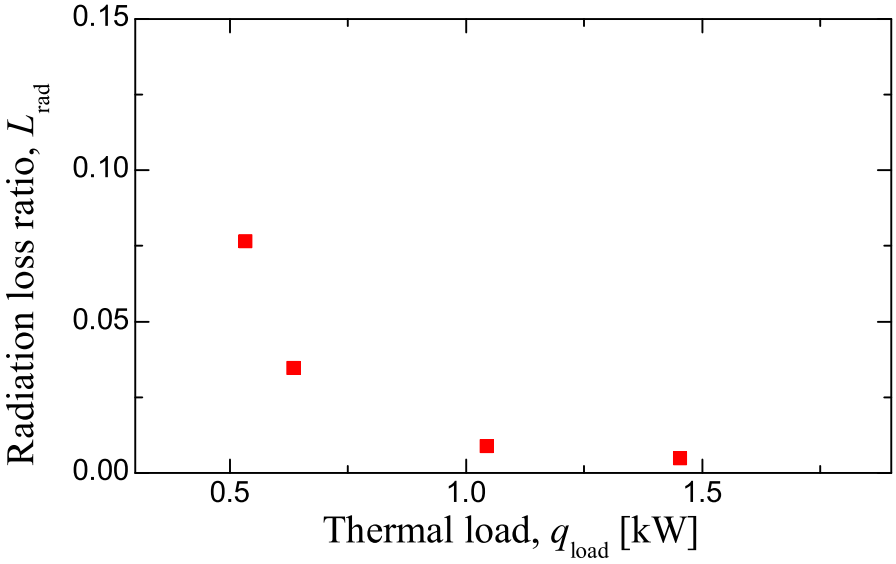

Figure 4.16: Radiation loss (Quartz glass reactor, $\phi = 3.5$)

the center region. This heat flux preheated the mixture in the center region and caused the higher flame temperature. This effect of the radial heat flux only appeared in the center region, therefore, the reaction as a whole was inactivated by the dominant radiation loss in the outer region, which reduced α in the small q_{load} conditions.

Next, by increasing q_{load}, the flame was formed away from the honeycomb except for the near-wall region. In this case, the thermal loss to the honeycomb was decreased, so that the gaseous reaction was not disturbed by the thermal interaction with the honeycomb. However, a further increase in q_{load} made the flame unstable, which is also not favorable as a fuel reformer.

Figure 4.16 shows the relation between the radiation loss ratio, L_{rad}, and q_{load}. It is obvious that the radiation has a great effect in the smaller q_{load} conditions. In $q_{\mathrm{load}} = 0.53\,\mathrm{kW}$, the radiation loss was $q_{\mathrm{rad}} = 9\,\mathrm{W}$, and the theoretical POX heat release was 117 W. The ratio, L_{rad}, is about 8 %, which is not negligible to the reaction activity in a small q_{load} condition. In higher q_{load} conditions, on the other hand, the value of L_{rad} decreases drastically with q_{load}. This was caused by the decrease of q_{rad} in higher q_{load}

conditions, and the increase of q_{load} itself.

4.4 Conclusions

In this chapter, the effects of the flame shape and location on the reaction performance was investigated. For realizing the simpler thermal field, and for the visualization experiments, the quartz glass reactor was fabricated in addition to the stainless steel reactor. Both of these reactors were applied to the POX reaction.

Experiments were conducted by varying the mixture flow rate (thermal load, q_{load}) at fixed equivalence ratios. This was due to reveal the effect of the flame shape and location on the reaction performance. The temperature distributions and the reaction performances in both of the reactors agreed qualitatively and the deterioration in the reaction performance in the lower thermal load conditions were observed.

Visualization of the flame in the quartz glass reactor was conducted and two-dimensional flame was observed. The reaction performance was discussed by relating the flame shape and the location relative to the ceramic honeycomb. The velocity distribution in the reactor was also measured to evaluate the flame shape.

By integrating the results in the quartz glass reactor, the effect of the radiation loss from the solid surface of the ceramic honeycomb was calculated and it was found that the radiation emission was the primary cause of the deterioration of the reaction in the lower thermal load conditions.

The major conclusions obtained are listed in the following:

- In the stainless steel reactor, the flame location moved to upstream with decreasing the thermal load.

- In the case of $\phi = 3.0$ in the stainless steel reactor, the reaction finally moved into the ceramic honeycomb in the smallest thermal load condition. In that case, the reaction temperature decreased drastically and the methanol conversion ratio was deteriorated markedly.

- The quartz glass reactor has the same trends of temperature distribution and reaction

performance as the stainless steel reactor. However, it was shown that the quartz glass reactor is more sensitive to the interaction between the flame and the ceramic honeycomb due to the adiabatic characteristic of quartz glass.

- Three types of the POX flame shape were observed regarding thermal load conditions. The conical flame had the best performance in terms of H_2 production and the reaction stability.

- The major effect determining the flame shape is the mixture velocity distribution at the outlet of the honeycomb.

- Radiation loss from the surface of the ceramic honeycomb was as high as 8 % of the POX reaction heat release rate in the smallest thermal load condition, which is believed to be the major reason of the deterioration of the reforming performance.

Bibliography

[1] Sathe, S. B., Kulkarni, M. R., Peck, R. E., and Tong, T. W., "An Experimental and Theoretical Study of Porous Radiant Burner Performance", *Proceedings of Twenty-Third Symposium (International) on Combustion*, (1990), pp. 1011–1018.

[2] Bouma, P. H., and de Goey, L. P. H., "Premixed Combustion on Ceramic Foam Burners", *Combustion and Flame*, Vol. 119 (1999), pp. 133–143.

[3] De Groote, A. M., and Froment, G. F. "Simulation of the Catalytic Partial Oxidation of Methane to Synthesis Gas" *Applied Catalysis A: General*, Vol. 138, No. 2 (1996), pp. 245–264.

[4] Held, T. J., and Dryer, F. L., "A Comprehensive Mechanism for Methanol Oxidation", *International Journal of Chemical Kinetics*, Vol. 30, No. 11 (1998), pp. 805–830.

[5] Japan Society of Mechanical Engineers (Ed.), *JSME Data Book: Thermophysical Properties of Fluids*, (1983), Japan Society of Mechanical Engineers (in Japanese).

[6] Egolfopoulos, F. N., Du, D. X., and Law, C. K., "A Comprehensive Study of Methanol Kinetics in Freely-Propagating and Burner-Stabilized Flames, Flow and Static Reactors, and Shock Tubes", *Combustion Science and Technology*, Vol. 83 (1992), pp. 33–75.

[7] Incropera, F. P., Dewitt, D. P., Bergman, T. L., and Lavine, A. S., *Introduction to Heat Transfer, Fifth Ed.*, (2007), John Wiley and Sons.

[8] Japan Society of Thermophysical Properties (Ed.), *Thermophysical Properties Handbook*, (2008), Yokendo Co. Ltd. (in Japanese).

[9] Yoshizawa, Y., Sasaki, K., and Echigo, R., "Analytical Study on the Structure of Radiation Controlled Flame", *Transactions of the Japan Society of Mechanical Engineers Ser. B*, Vol. 52, No. 482 (1986), pp. 3587–3593 (in Japanese).

[10] Hanamura, K., Echigo, R., and Yoshizawa, Y., "Structure and Transient Behavior of Radiation-Controlled Flame in A Highly Porous Medium", *Transactions of the Japan Society of Mechanical Engineers Ser. B*, Vol. 57, No. 533 (1991), pp. 315–321 (in Japanese).

Chapter 5

Enhancement of POX Reaction Using Energy Regeneration by Ceramic Honeycomb

5.1 Introduction

In the previous two chapters, the basic reaction characteristics of POX, the flame stability, and the reaction performance in terms of the flame shape and location were investigated. It was revealed that the reaction performance is very sensitive to the flame location when the POX flame is stabilized in the vicinity of the ceramic honeycomb since the thermal interaction between the flame and ceramic honeycomb has a major influence on the flame temperature and the degree of methanol decomposition reaction. This is because a radiation loss is induced when the flame is attached to the honeycomb, which causes the quenching effect and reduces the reaction activity.

On the basis of the knowledge obtained in the previous chapters, the concept of energy regeneration by a radiation converter is introduced in the present reformer. Weinberg [1] first proposed the methods to control the combustion temperature by means of energy regeneration. He pointed out that since the reaction temperature has a steep dependence on the reaction rate, flexible reaction systems can be achieved by utilizing the regenerated energy to extend the conventional operation limits. His proposal to design novel combustion

systems were then applied to various combustors to extend operation limits, minimize pollution, and optimize the combustion intensity. Echigo [2] proposed a concept of a radiation converter on the engineering perspectives wherein the enthalpy of the working gas flowing through a porous material is efficiently converted into radiation emission because of the high convection heat transfer coefficient between the gas and solid surface. For example, Yoshizawa et al. [3] utilized a radiation converter as a heat source of steam reforming of methane. They realized a very high radiation flux from the radiation converter having an high efficiency of radiation conversion up to 80–90 %. It was clarified that a wide range of operating condition was possible. Okuyama et al. [4] also reported that by adding a porous material to a combustor, it was possible to stabilize a super-rich flame beyond the flammability limit. Jugjai et al. [5] applied a porous material to a liquid fuel combustor, then combined with a porous radiation converter to enhance the evaporation of the liquid fuel by radiation energy regeneration, which resulted in a lower exhaust emission characteristics. Lammers et al. [6] pointed out that when a porous material is introduced in a combustor, a radiation loss from the porous material has a remarkable effect on the flame stability. They revealed that the temperature of the reactor inner wall plays an important role in the flame stability characteristics because the amount of the radiation loss is primarily dominated by the surrounding wall temperature.

In order to achieve higher methanol conversion and hydrogen production ratios in the present reactor, a secondary honeycomb was introduced in the downstream of the primary honeycomb. This secondary honeycomb works as a radiation converter and realizes energy regeneration from the post-reaction reforming gas toward the reaction region by means of radiation emission from the solid surface of the secondary honeycomb. Due to the radiation exchange between the secondary honeycomb and inner wall of the reactor, and between the primary and secondary honeycombs, the primary honeycomb and inner wall of the reactor is heated up and the preheating of the mixture gas is enhanced.

In the following discussion, the effect of the secondary honeycomb configuration on the energy regeneration and resulted reaction performance were investigated. Moreover, the

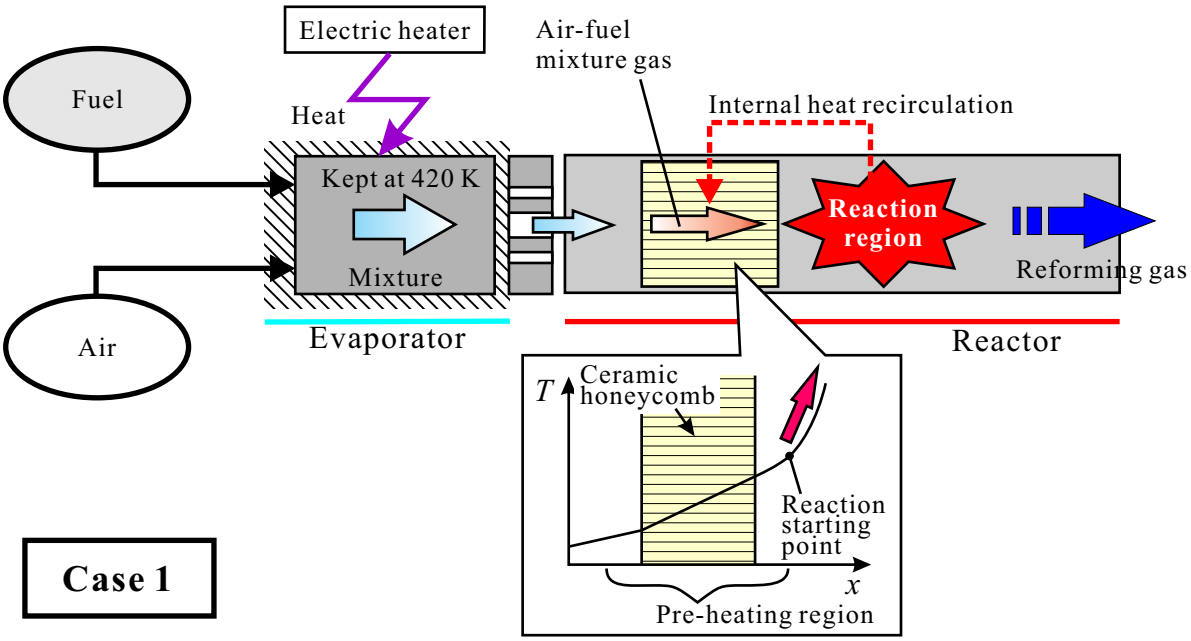

Figure 5.1: Schematic of experimental configuration and its reaction region (Case 1).

flame location and temperature were measured in the case with the secondary honeycomb to reveal the optimum use of the ceramic honeycomb to the POX fuel reformer as a radiation converter.

5.2 Experimental Apparatus and Conditions

5.2.1 Concept of Radiation Converter

In this chapter, we investigate the effect of the secondary honeycomb inserted in the post-reaction region for the purpose of utilizing the exhaust heat possessed by the reforming gas.

In the previous chapters, the primary honeycomb, Honeycomb A, was inserted as a flame stabilizer. We call this case with a single honeycomb Case 1. The reactor configuration and the schematic concept is shown in Fig. 5.1. Because a ceramic honeycomb has a large surface area and higher thermal conductivity than the working gas, we expected to realize a wider range of operating condition than the case without the honeycomb. This extension

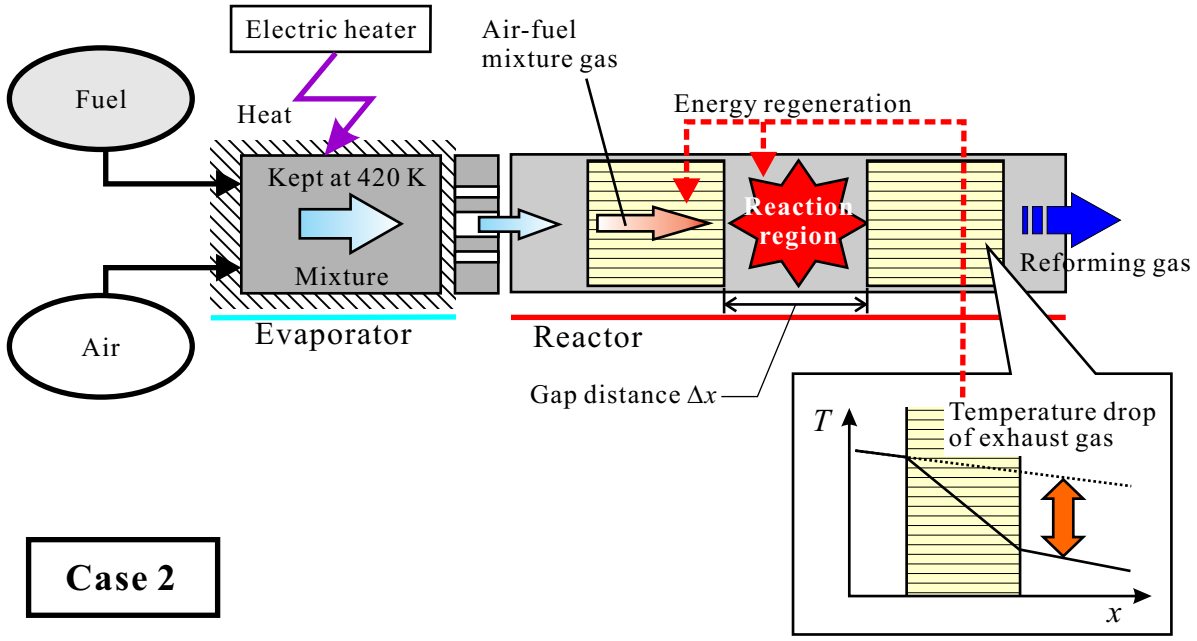

Figure 5.2: Schematic of experimental configuration and its reaction region (Case 2).

of the operation limit is due to the enhancement of the mixture gas preheating caused by the "internal heat recirculation" through the reactor wall and solid phase of Honeycomb A. Due to this thermal characteristics of the ceramic honeycomb, fuel-rich combustion beyond the flammability limit was possible to sustain in the reactor. Moreover, Honeycomb A has a role to prevent backfire by its quenching effect which enabled the reaction with a very low thermal load condition to sustain as discussed in Chap. 4.

In this chapter, a secondary honeycomb—we call this Honeycomb B—is added to the downstream of the reaction region. This case is called Case 2. The material characteristics and dimensions of Honeycomb B is the same as Honeycomb A. The schematic concept of energy regeneration by Honeycomb B in Case 2 is shown in Fig. 5.2. Honeycomb A still works as a flame stabilizer in the same manner as Case 1. Honeycomb B is, on the other hand, expected to play a role to regenerate the heat possessed by the reforming gas, i.e., the enthalpy of the reforming gas was absorbed by Honeycomb B when the reforming gas flowed through it, and a portion of the absorbed enthalpy was regenerated toward the upstream reaction region by radiation and conduction heat transfers. By this effect, temperatures

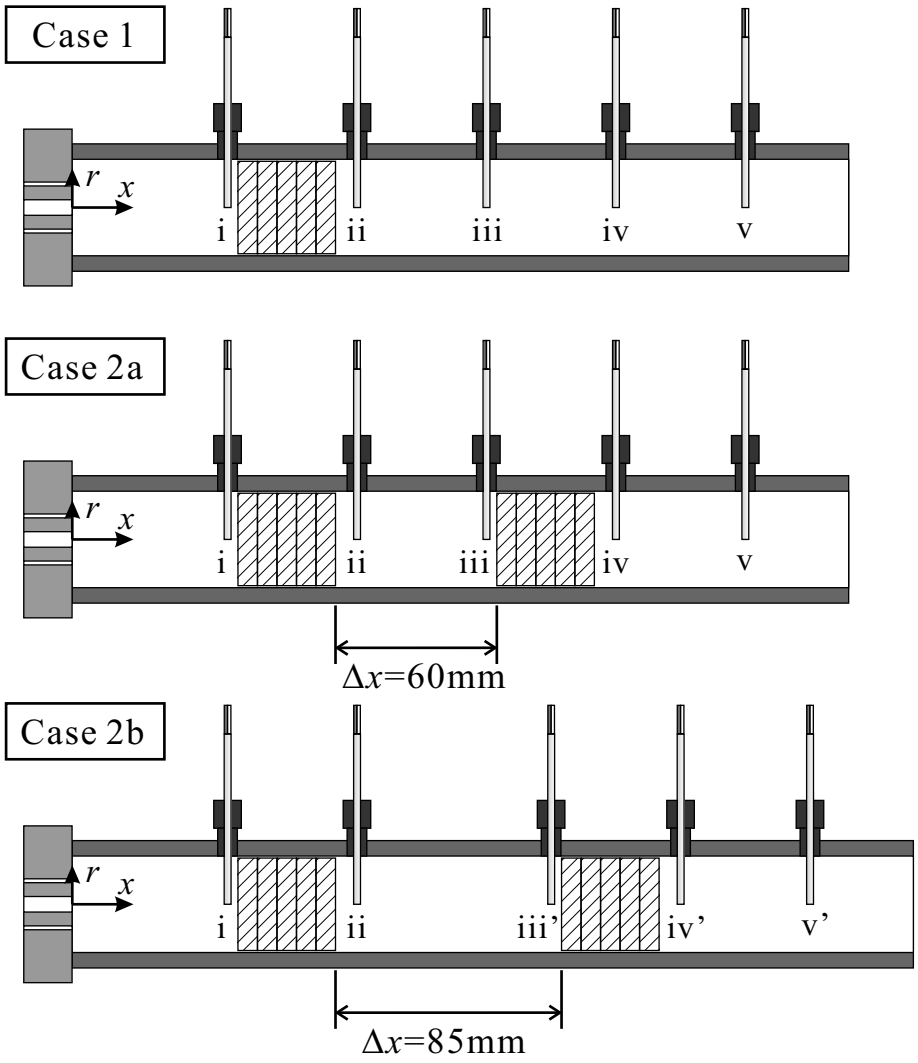

Figure 5.3: Honeycomb block and thermocouples positions in each case.

of Honeycomb A and inner wall of the reactor increase, which enhance the preheating of the mixture gas and reduce the thermal loss from the working gas to the exterior of the reactor.

5.2.2 Apparatus Setup

Because the ignition of the POX reaction between Honeycomb A and Honeycomb B was not possible in the quartz glass reactor due to a safety issue, experiments in Case 2 were conducted by the stainless steel reactor. The visualization of the flame, therefore, was

Table 5.1: Positions of thermocouples.

Case	1, 2a, 2b		1, 2a			2b		
Position	i	ii	iii	iv	v	iii'	iv'	v'
x [mm]	60	110	160	210	260	185	235	285
x/D	1.6	3.0	4.4	5.7	7.1	5.0	6.4	7.8

not conducted in Case 2. However, as discussed in Chap. 4, the qualitative discussion is interchangeable between the stainless steel reactor and quartz glass reactor. therefore, the discussion involving the thermal interaction and flame characteristics are also devoted in this chapter.

In the following discussion, the results in three cases—Case 1, Case 2a, and Case 2b—are presented. First, the experiment with only Honeycomb A is presented again for comparison. This case is called Case 1, which are previously discussed in Chaps. 3 and 4.

By introducing Honeycomb B, on the other hand, the effect of energy regeneration was added to the reaction. This is Case 2, in which two conditions were set according to the gap distance between Honeycomb A and Honeycomb B, Δx. These cases are called Case 2a and Case 2b. By changing Δx, the degree of energy regeneration is varied. Therefore, the influence of energy regeneration on the reforming reaction can be evaluated quantitatively. In Case 2a, Δx was set to 60 mm, while in Case 2b, Δx was set to 85 mm.

The configurations of the reactor in the respective cases are shown in Fig. 5.3. Note that in Case 2b, the locations of the radial-type thermocouples in downstream region are different from Case 1 and Case 2a. The locations of thermocouples in Case 2b are, therefore, re-named as iii', iv', and v'. Each locations and its dimensionless coordinates are shown in Table 5.1.

5.3 Results and Discussion

In this section, Honeycomb B was added to the reactor having a gap distance, Δx. The effect of the gap distance, Δx, was first investigated by the experiments where Δx is varied in two conditions ($\Delta x = 60\,\mathrm{mm}$ and $85\,\mathrm{mm}$) and the extent of the enhancement of the preheating of the mixture gas and the change of the reaction characteristics were investigated. Then, the experiments in a wide range of q_{load} conditions are conducted to investigate the effect of energy regeneration on the thermal interaction between the flame and solid surface of the ceramic honeycomb. The reforming performance in Case 2 is compared with that in Case 1 to discuss the effect of energy regeneration.

5.3.1 Effects of Equivalence Ratio and Gap Distance

First, the streamwise temperature distributions in Case 2a and Case 2b are compared with those in Case 1. The temperature distributions measured by the radial-type thermocouples are shown in Fig. 5.4. The thermal load condition was chosen $q_{\mathrm{load}} = 1.45\,\mathrm{kW}$ as a representative case.

In the case of $\phi = 3.0$, the temperature at Position ii increased in both Case 2a and Case 2b compared with Case 1. In addition, at Position iii, the temperature in Case 2a was also higher than Case 1. This is because the probes at Position ii and Position iii are located between Honeycomb A and Honeycomb B. Therefore, higher temperature in the gap region between these honeycombs was realized by the effect of Honeycomb B. In Case 2b, the locations of the thermocouples are different from those in Case 1 and Case 2a, thus, it is not possible to compare the temperature simply here.

At Position iv and Position v located in the downstream of Honeycomb B, on the other hand, temperatures in Case 2 were about 100 K lower than those in Case 1. This temperature decrease in the downstream of Honeycomb B was due to the fact that a portion of the enthalpy possessed by the reforming gas flowing through Honeycomb B was absorbed by the solid surface of Honeycomb B and used to heat up the honeycomb solid. A radiation flux induced by the high temperature solid surface of Honeycomb B, on the other hand,

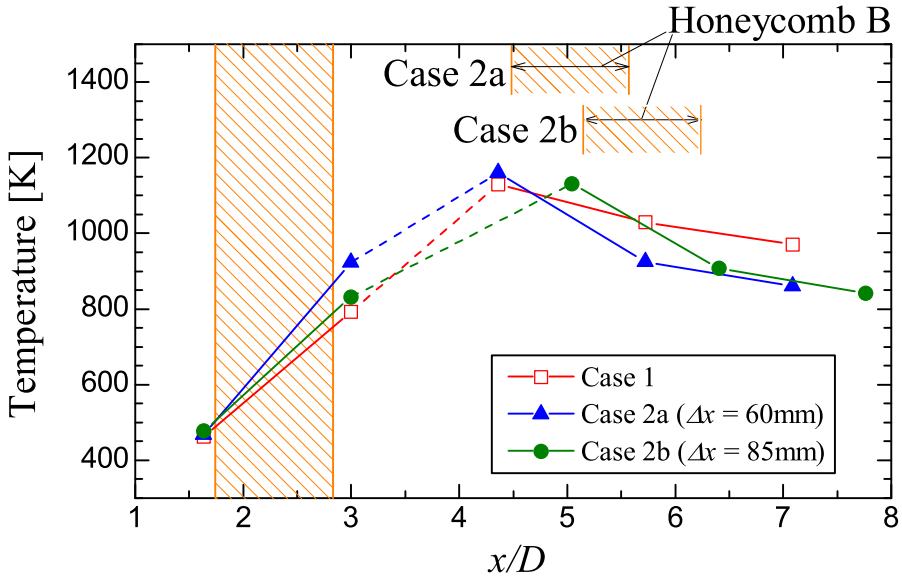

(a) $\phi = 3.0$

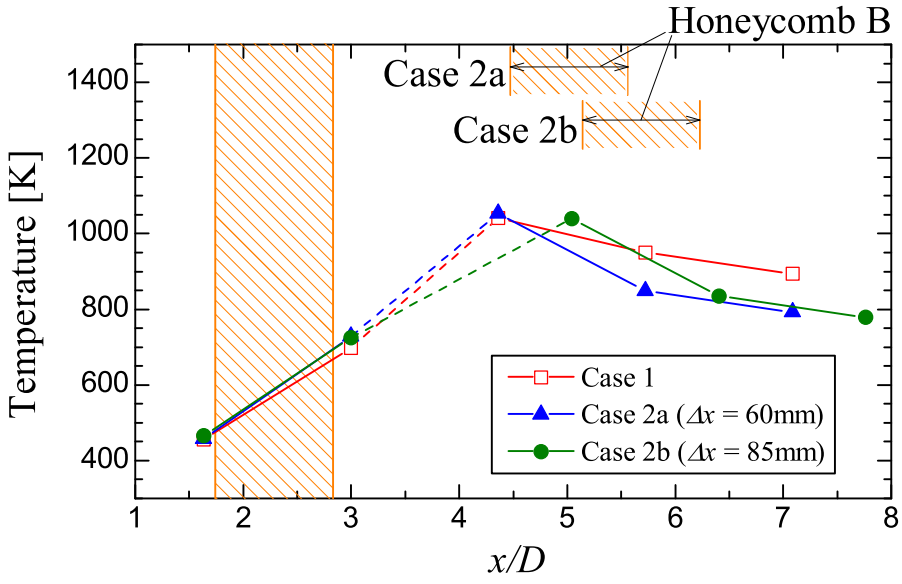

(b) $\phi = 3.5$

Figure 5.4: Streamwise temperature distributions measured by radial-type thermocouples ($q_{\mathrm{load}} = 1.45\,\mathrm{kW}$).

removes the energy from the honeycomb solid surface, thus the temperatures at Position iv and Position v were lowered.

In the case of $\phi = 3.5$, however, the temperature at Position ii did not change markedly in Case 2 compared with Case 1. While, in the downstream part of the reactor, temperature decreased in the same way as $\phi = 3.0$. The reason of the different trend at Position ii will be explained later.

Next, in order to closely look into the flame temperature and location in Case 2, detailed temperature distributions measured by the transverse-type thermocouple are shown in Fig. 5.5. In Fig. 5.5(a), the maximum flame temperature, $T_{\max}$, in $\phi = 3.0$ of both Case 1 and Case 2a exceeded T_{af}, but the value of $T_{\max}$ in Case 2a was 50 K higher than in Case 1. Moreover, the flame location is much closer to Honeycomb A in Case 2a.

In the detailed temperature measurements, the temperature drop inside Honeycomb B in Case 2a was clearly observed. The temperature difference between Case 1 and Case 2 at the outlet of Honeycomb B was as much as about 100 K. This tendency is due to energy regeneration effect by Honeycomb B. A portion of enthalpy absorbed by the solid phase of Honeycomb B was used to increase the solid temperature of Honeycomb B. The higher temperature solid surface of Honeycomb B facing upstream emits net radiation toward the relatively lower temperature solid surface located upstream. The emitted radiation reaches the inner wall of the reactor or downstream surface of Honeycomb A. Based on a rough calculation of view factors within the reactor, about 92 % of the radiation energy emitted from the upstream surface of Honeycomb B reaches the inner wall surface of the reactor, while about 8 % of the radiation energy reaches the outlet surface of Honeycomb A. Therefore, most of the regenerated energy was used to warm up the reactor inner wall, thereby decreasing the thermal loss from the reforming gas to the environment. The rest of the radiation energy contributed to warm up the solid surface in the vicinity of Honeycomb A, which directly enhanced the preheating of the mixture gas. Both of these effects worked sufficiently to increase temperatures in the reaction and post-reaction regions.

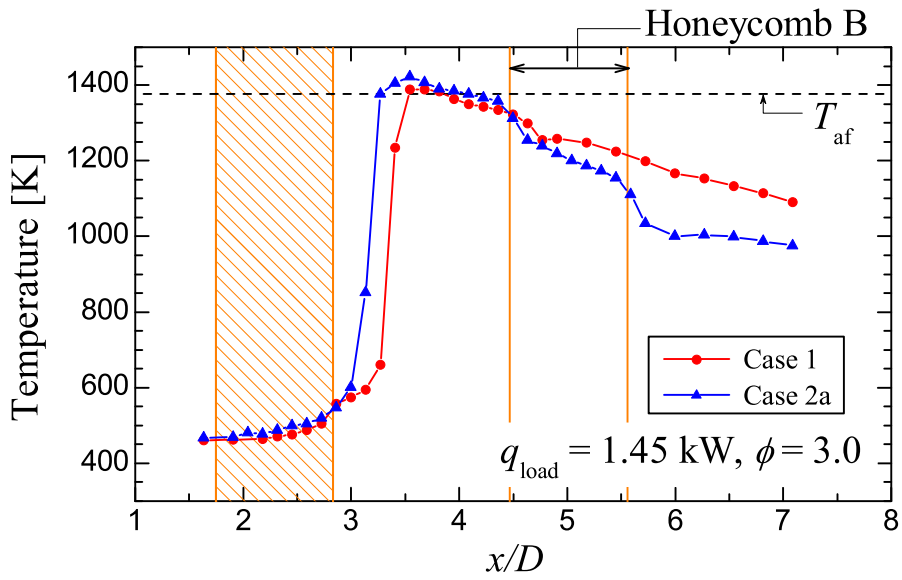

(a) $\phi = 3.0$

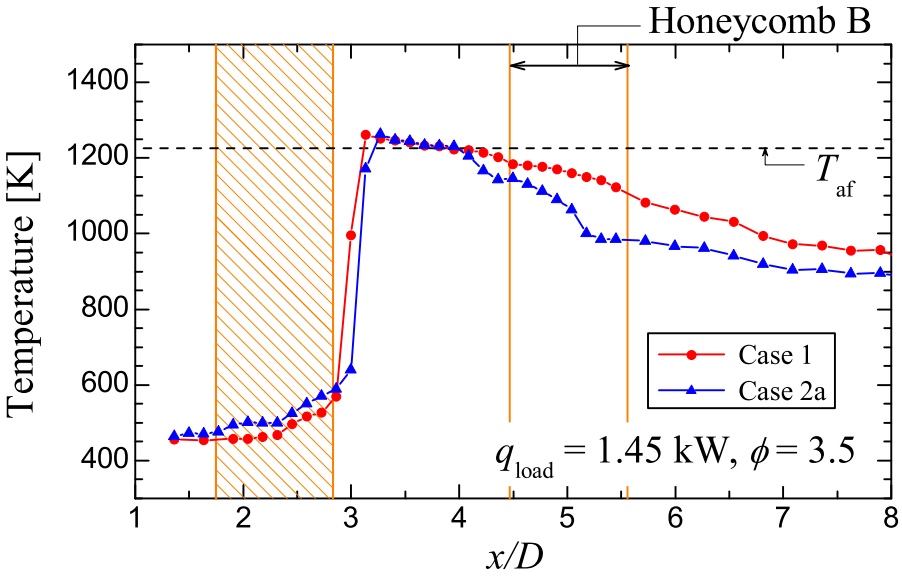

(b) $\phi = 3.5$

Figure 5.5: Streamwise temperature distributions (measured by transverse-type T/C, q_{load} = 1.45 kW in Case 1 and Case 2a).

In the case of $\phi = 3.5$, however, the reaction temperature in Case 2a is not so much increased by Honeycomb B, and the flame location did not move upstream (slightly moved downstream in fact). By considering the radiation effect mentioned above, this phenomenon in $\phi = 3.5$ is contradictory to the previous discussion. We now need to consider the radial temperature distributions in the reactor for more precise understanding of the phenomena within the reactor.

Figure 5.6 shows the radial temperature distributions at Position ii (adjacent to the outlet surface of Honeycomb A) measured by the radial-type probe. First, in $\phi = 3.5$ (shown in Fig. 5.6(b)), comparing the temperature distribution in Case 2b with that in Case 1, the temperature at around the center axis did not change in Case 2b. Thus, the effect of Honeycomb B is limited in the outer region of the reactor, $0.2 \leq r/D \leq 0.4$. In Case 2a, on the other hand, temperature increase region spread into more inner region and reached the axial center of the reactor. This is because of the smaller Δx in Case 2a than Case 2b. It is reasonable to have such a tendency that temperature increasing region spread from the outer region to the inner region according to the increase in the radiation flux with respect to the decrease in Δx.

The effect of Δx on the reaction temperature can be explained by the difference of the view factor. Comparing Case 2a and Case 2b, view factor from the upstream surface of Honeycomb B to the downstream surface of Honeycomb A is 0.08 in Case 2a ($\Delta x = 60\,\mathrm{mm}$), and 0.04 in Case 2b ($\Delta x = 85\,\mathrm{mm}$). Since the temperatures at the adjacent location of the upstream surface of Honeycomb B are not so much different between Case 2a and Case 2, the irradiation from Honeycomb B is directly influenced by the view factor. Therefore, by comparing simply the radiation flux directly irradiated to the downstream surface of Honeycomb A, Case 2a has twice as much radiation flux as Case 2b.

In $\phi = 3.0$ (shown in Fig. 5.6(a)), however, a different tendency was observed. Comparing the temperature distributions of Case 1 with Case 2b, a similar trend to $\phi = 3.5$ was observed. That is to say, the region of temperature increase by the effect of Honeycomb B was first observed in the outer region of the reactor, $0.1 \leq r/D \leq 0.5$, in this

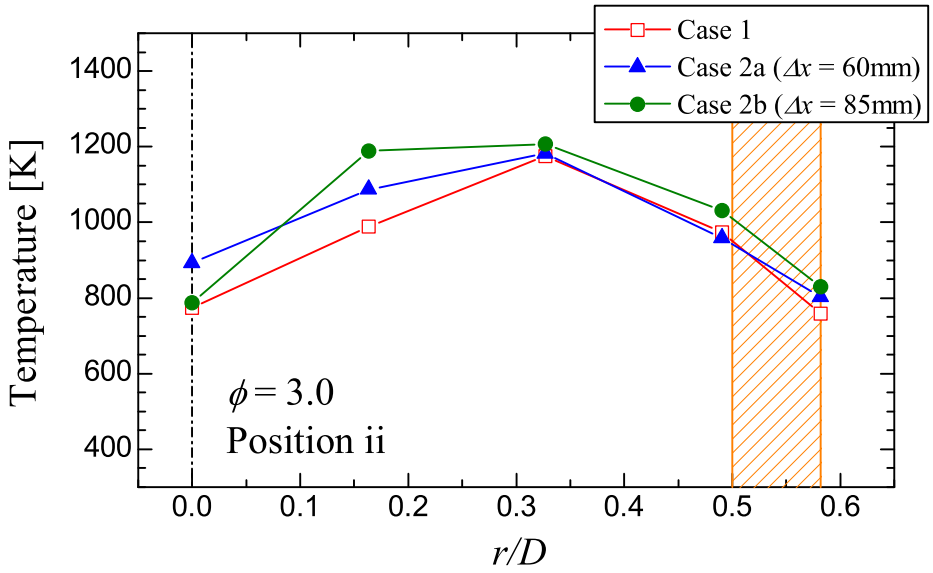

(a) $\phi = 3.0$

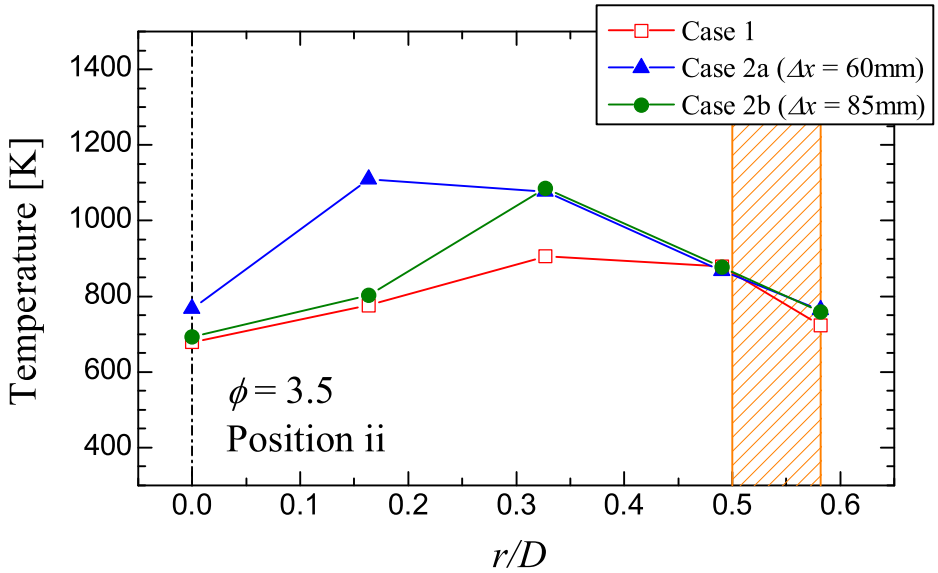

(b) $\phi = 3.5$

Figure 5.6: Radial temperature distributions measured by radial-type thermocouples (q_{load} = 1.45 kW).

case. However, even though the temperature in Case 2a at the axial center observed an increase compared with Case 2b, temperature decreased in the outer region $0.1 \leq r/D \leq 0.5$ in Case 2a. This trend can be explained by the quenching effect due to the thermal interaction between the flame and ceramic honeycomb as previously discussed in Chap. 4. The flame in Case 1 has a conical shape with a base attaching on the outer region of Honeycomb A. The peak of the gas temperature at Position ii was observed at around $r/D = 0.3$ in Case 1, which indicates that the flame attached at around this location. When Honeycomb B was inserted (Case 2b) and energy regeneration was in effect, the preheating of the mixture gas was enhanced and the upstream shifting of the flame was realized. This shifting corresponds to the temperature increase in the region $0.1 \leq r/D \leq 0.5$. In Case 2a that Δx was reduced to 60 mm, a degree of energy regeneration, therefore, became larger than Case 2b due to the closer configuration of Honeycomb B which increased the radiation flux toward upstream. This caused the further shifting of the flame toward upstream. Finally, the flame in the outer region moved into or very close to Honeycomb A, which caused the quenching effect due to the closely existing flame to the ceramic honeycomb. The quenching effect may reduce the flame temperature as discussed in Chap. 4, therefore, the temperature in the outer region in Case 2a was decreased below Case 2b. At the axial center region, on the other hand, the flame was still not in contact with Honeycomb A, thus, the temperature was increased due to the enhancement of the mixture preheating.

Figure 5.7 shows the methanol conversion ratio, α, in various ϕ of three cases: Case 1, Case 2a, and Case 2b. Comparing these cases, both Case 2a and Case 2b observed higher α than Case 1 in most of the ϕ conditions. In a rough observation, the value of α increased in the order of Case 1, Case 2b, and Case 2a. These results indicate that the reforming performance is improved by Honeycomb B, and smaller Δx is favorable in terms of α.

The value of Δx has also an influence on the enhancement of the reaction especially in larger ϕ. In large ϕ conditions, the heat release rate of POX becomes small due to the reduction of the oxygen flow. On the other hand, the temperature in the post-reaction region is still high. Thus, the ratio of the regenerated radiation flux to the reaction heat

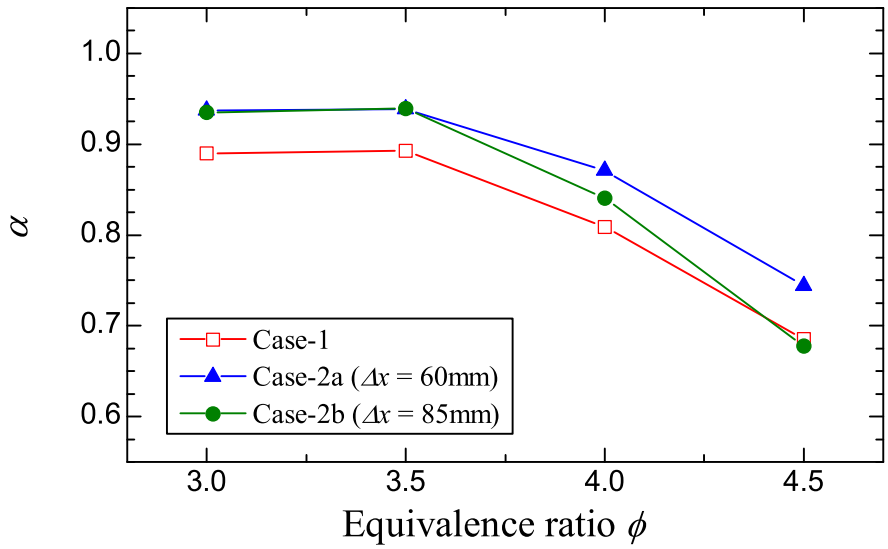

Figure 5.7: Methanol conversion ratio in Case 1, Case 2a, and Case 2b ($q_{\mathrm{load}} = 1.45\,\mathrm{kW}$).

release rate is not so much reduced in larger ϕ. This makes the effect of energy regeneration more apparent in larger ϕ conditions. By the above influence of Honeycomb B, a slight difference of α with respect to Δx in larger ϕ was observed.

Next, we evaluate the effect of Honeycomb B on the preferential production ratios, β and γ. Figure 5.8 shows the influences of ϕ on β and γ. The value of β increased with ϕ in all cases, while γ took an almost-constant value. These tendencies of β and γ with respect to ϕ was explained in Chap. 3 by the equilibrium compositions of POX.

Comparing Case 1 with Case 2, the values of β in Case 2 are smaller in larger ϕ conditions. Also γ took slightly larger values in Case 2. The decrease in β and increase in γ may be caused by the equilibrium shift of the reaction due to the increase in the temperature of the flame in Case 2. As discussed in the previous section, higher flame temperature is realized in Case 2 compared with Case 1 even though the premixed gas composition is the same. Thus, the chemical equilibrium was shifted according to the temperature increase. In Fig. 3.10, it is observed that when the reaction is taking place at T_{af}, the sensitivity of both β and γ to the reaction temperature expressed respectively by $\left|\frac{\Delta\beta}{\Delta T}\right|_{T=T\mathrm{af}}$ and $\left|\frac{\Delta\gamma}{\Delta T}\right|_{T=T\mathrm{af}}$,

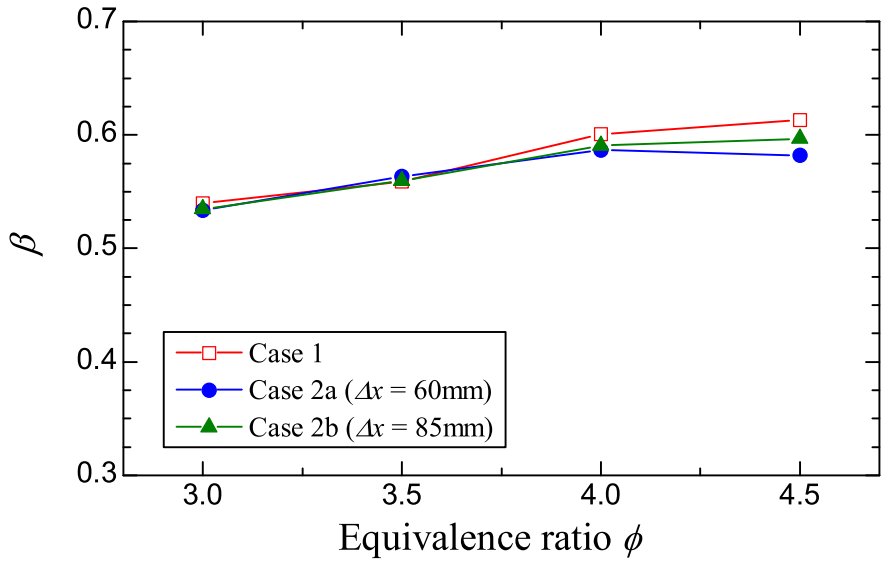

(a) β

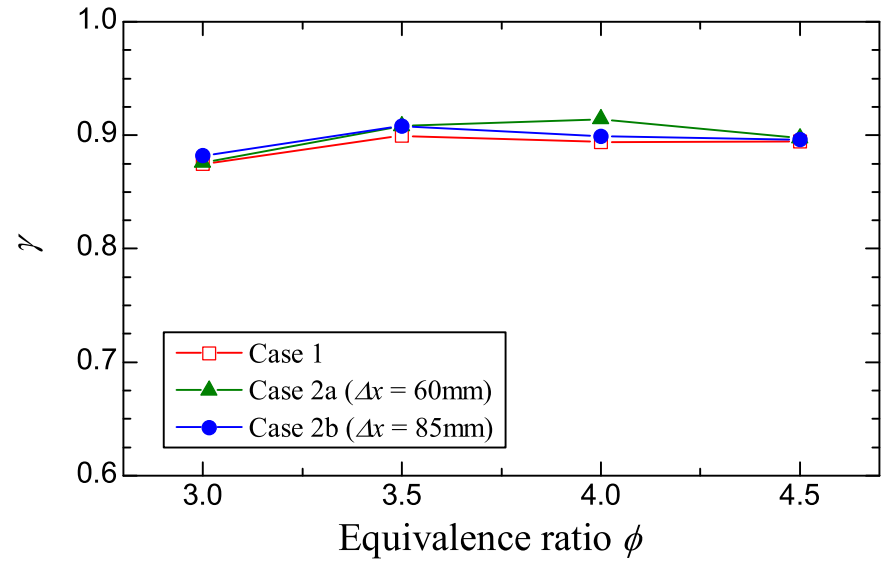

(b) γ

Figure 5.8: Preferential production ratios (Case 1 and Case 2, $q_{\mathrm{load}} = 1.45\,\mathrm{kW}$).

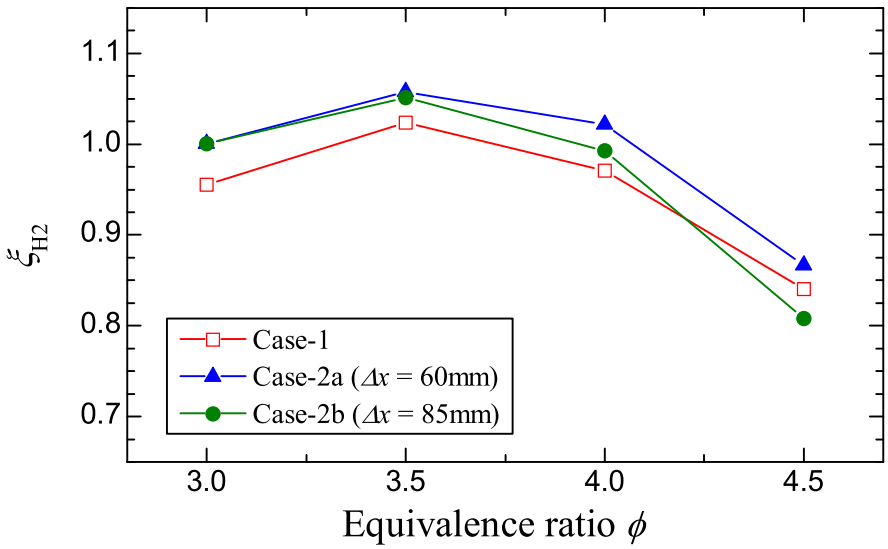

Figure 5.9: Hydrogen production ratio in Case 1, 2a and 2b ($q_{\mathrm{load}} = 1.45\,\mathrm{kW}$).

increases with ϕ. This is one of the reasons why the difference between Case 1 and Case 2 appeared in larger ϕ conditions.

Figure 5.9 shows the hydrogen production ratio, ξ_{H2}. In most conditions, the values of ξ_{H2} in Case 2 is larger than that in Case 1, and the plot of Case 2b lay between those of Case 1 and Case 2a. As stated before, ξ_{H2} is influenced by both α and β. Thus, we consider separately the effect on ξ_{H2} of each parameter.

First, larger α is obtained in Case 2 in the whole ϕ conditions. This is because the thermal effect of Honeycomb B increased the reaction temperature, and resulted in higher α. On the other hand, the effects of the temperature increase on the reaction characteristics represented by β and γ are relatively small. Thus, the value of ξ_{H2} was almost directly influenced by the trend of α. Therefore, the value of ξ_{H2} took the highest value at $\phi \approx 3.5$ where α also took the highest value.

From these results, it is noted that the important factor of the enhancement of the fuel reforming reaction is to increase α by increasing the reaction temperature. Honeycomb B worked to induce energy regeneration which kept the reaction region to observe higher

temperature. In the next section, we examine whether the same trend can be achieved in the whole range of thermal load conditions and discuss in terms of the flame locations and temperature distributions within the reactor.

5.3.2 Effects of Thermal Load

To evaluate the flame location affected by Honeycomb B, Case 1 and Case 2 are compared with each other in Fig. 5.10 in terms of $(x/D)_{T\max}$. In $\phi = 3.0$, the flame shifted upstream in all q_{load} conditions in Case 2a. Both plots in Case 1 and Case 2a are almost parallel in $q_{\mathrm{load}} \leq 1.76\,\mathrm{kW}$, i.e. the degree of the upstream shifting did not change markedly with respect to q_{load}. In the largest q_{load} of Case 1, the flame experienced liftoff, while the flame in Case 2a stayed at the similar location to the smaller q_{load} conditions. This indicates that the stable conditions of q_{load} was extended up to 2.12 kW in Case 2a due to the effect of Honeycomb B.

However, by comparing the flame locations in relatively small q_{load} conditions, it was easier for the flame to move into Honeycomb A in Case 2a because of the upstream shifting of the flame. Comparing both cases, the critical q_{load} condition in which the flame moves into Honeycomb A is larger in Case 2a than in Case 1. This means that the quenching effect of Honeycomb A must be considered in a wider q_{load} conditions in Case 2a.

In $\phi = 3.5$, the flame also moved upstream by the effect of Honeycomb B in the limited condition of $q_{\mathrm{load}} < 1.45\,\mathrm{kW}$. In larger q_{load} conditions, the shifting of the flame was not noticeable. In these conditions, the ratio of the net amount of energy regeneration to the reaction heat release is smaller because the reaction heat release rate increases corresponding to q_{load}. For this reason, the flame location is not so much affected by Honeycomb B in relatively large q_{load} conditions.

Figure 5.11 shows the maximum flame temperature measured in both Case 1 and Case 2a. In both ϕ, the temperature distribution is not so much different comparing between Case 1 and Case 2a. (A slight increase in temperature is observed in Case 2a, though.) As discussed in Sec. 5.3.1, the thermal effect of Honeycomb B is more obvious in

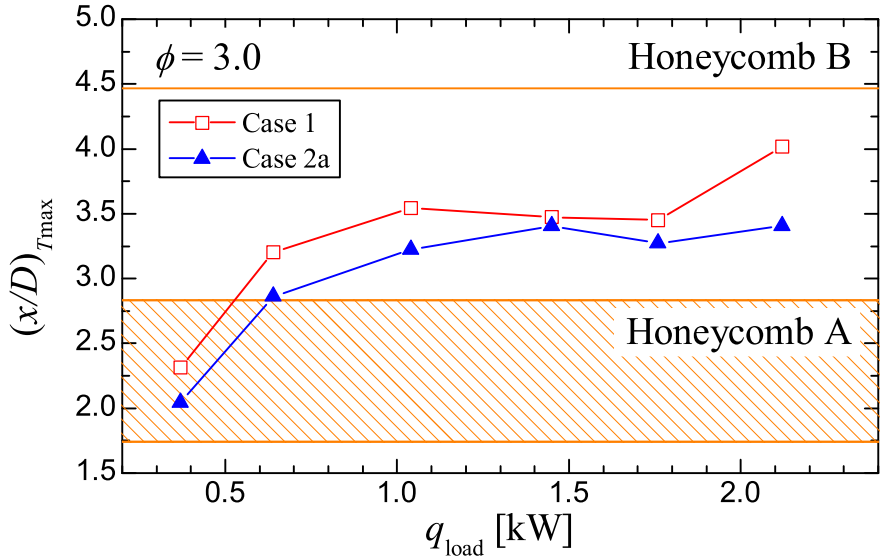

(a) $\phi = 3.0$

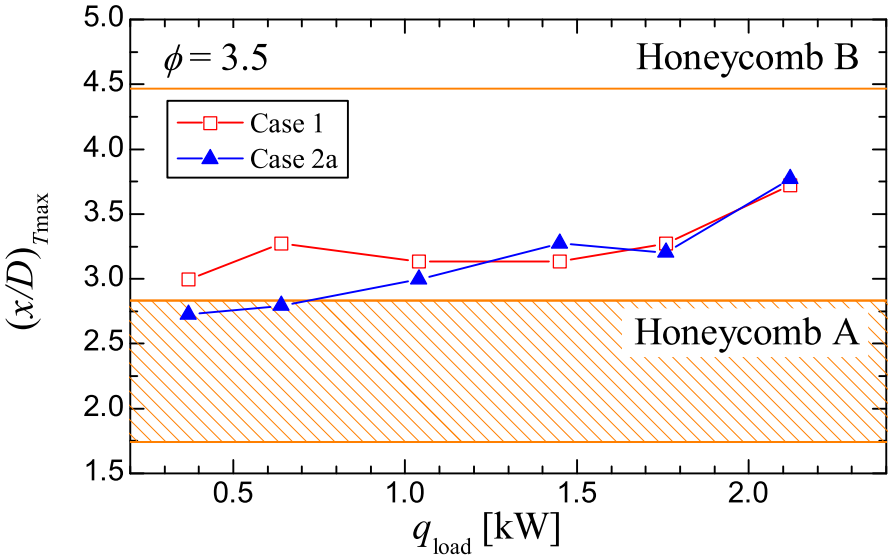

(b) $\phi = 3.5$

Figure 5.10: Comparison of the locations where the maximum flame temperature was observed between Case 1 and Case 2a.

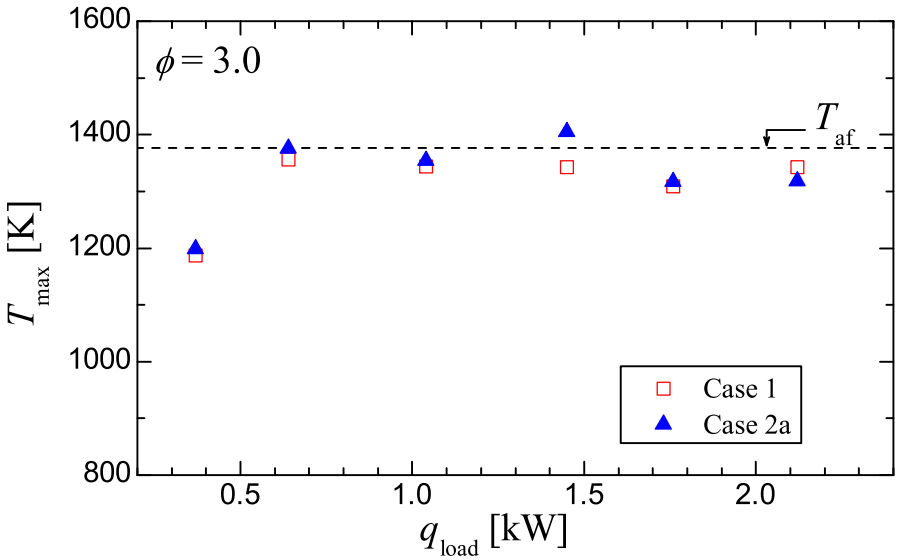

(a) $\phi = 3.0$

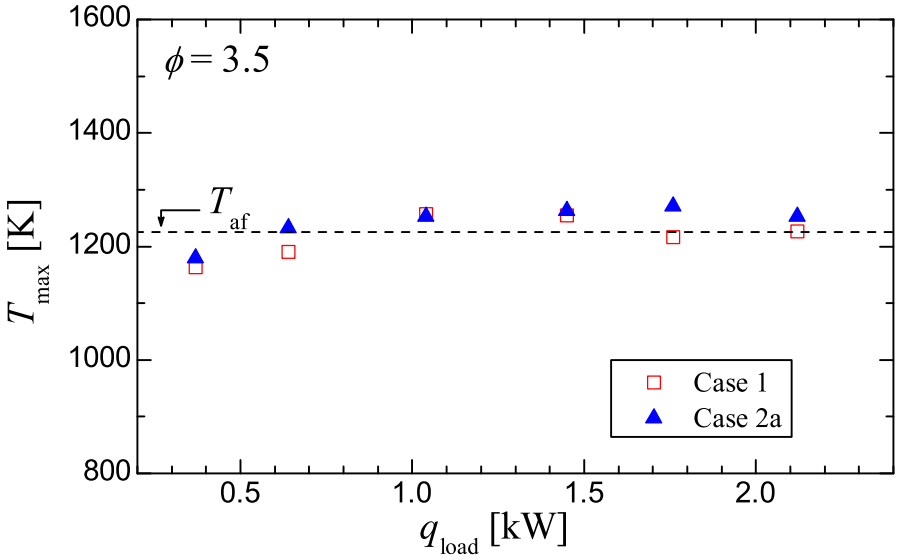

(b) $\phi = 3.5$

Figure 5.11: Comparison of the maximum flame temperature measured at the axial center of the reactor between Case 1 and Case 2a.

the outer region. Thus, in the axial temperature measurements, only the flame shifting was observed and the apparent temperature increase was not observed in the axial temperature distribution.

In the following discussion, the effect of Honeycomb B on the reforming characteristics are discussed based on the flame location and the corresponding thermal interaction between the flame and honeycomb.

Figures 5.12 and 5.13 show the comparison of the reforming evaluation parameters in each ϕ condition. In $\phi = 3.0$, the value of α increased in most of the q_{load} conditions in Case 2a. Since the flame temperature at the axial center did not change in Case 2, the increase in α is mainly because of the temperature increase in the outer region. In smaller q_{load}, α in Case 2a also experienced deterioration compared with larger q_{load}. However, the deterioration in Case 2a is much smaller than that in Case 1. This is due to both the quenching effect and energy regeneration. In Case 2a, the flame of $q_{\mathrm{load}} = 0.37\,\mathrm{kW}$ moved into Honeycomb A as shown in Fig. 5.10(a). Thus, the quenching effect caused the deterioration of α. However, in this case, the irradiation from Honeycomb B recover a portion of the radiation loss, which reduced the quenching effect and degree of the deterioration of α.

In $\phi = 3.5$, the value of α in Case 2a is increased in comparison with Case 1 in $0.64 \leq q_{\mathrm{load}} \leq 1.74\,\mathrm{kW}$. This enhancement was caused by the energy regeneration effect by Honeycomb B in the same way as $\phi = 3.0$.

In the condition $q_{\mathrm{load}} = 0.37\,\mathrm{kW}$ of Case 2a, α is reduced to the same level of Case 1. This deterioration of α was due to the quenching effect of Honeycomb A. In this q_{load} condition, the flame of Case 1 existed slightly outside of Honeycomb A. However, by introducing Honeycomb B, the flame moved into Honeycomb A as presented in Fig. 5.10(b). This shifting of the flame into Honeycomb A induced the quenching effect and reduced the value of α.

In $q_{\mathrm{load}} = 2.12\,\mathrm{kW}$ the value of α also decreased drastically compared with other q_{load} conditions. This deterioration was, on the other hand, caused by the existence

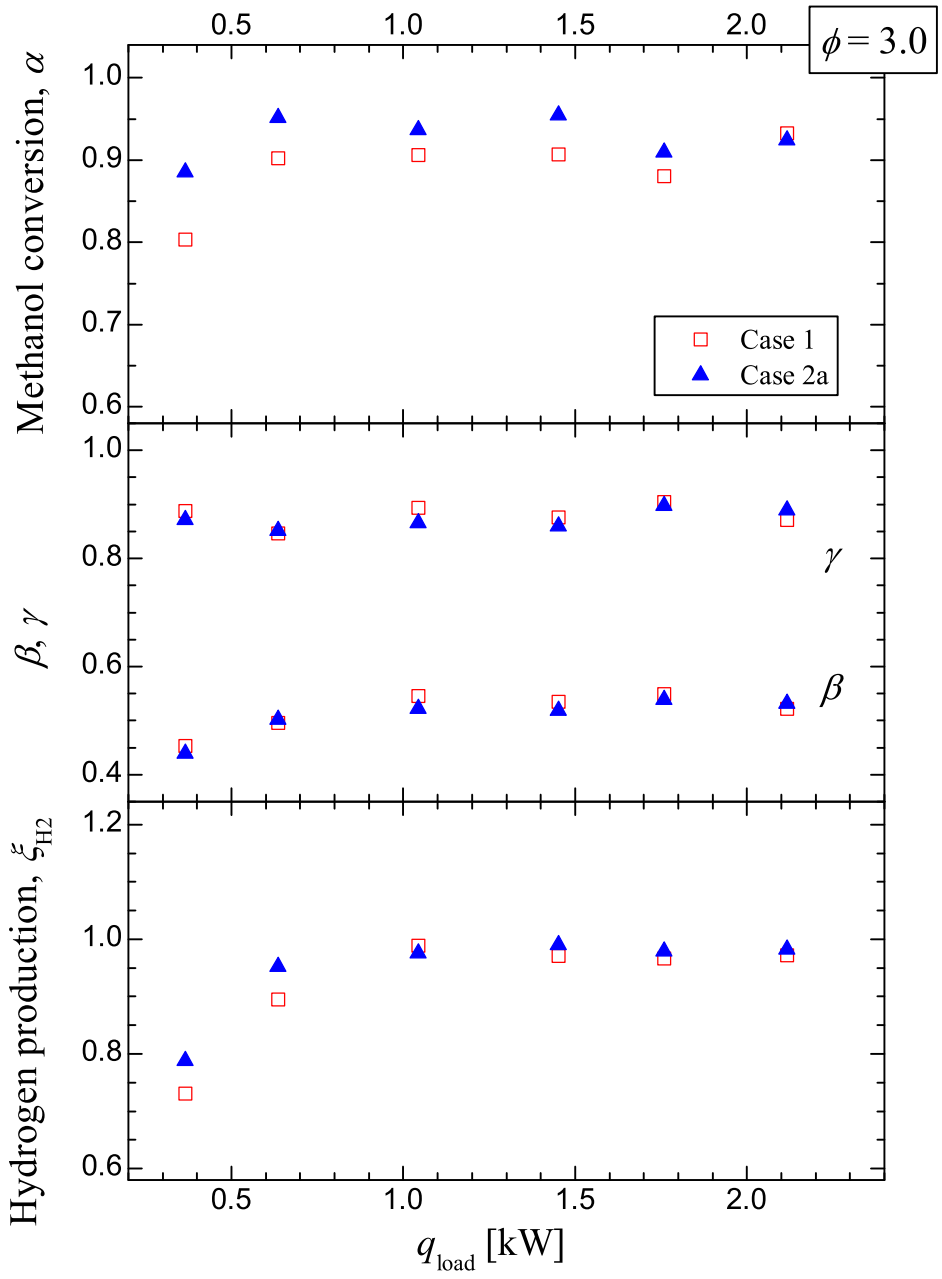

Figure 5.12: Comparison of reforming evaluation parameters in $\phi = 3.0$ between Case 1 and Case 2a. (a) Methanol conversion ratio, α. (b) Preferential production ratios, β and γ. (c) Hydrogen production ratio, ξ_{H2}.

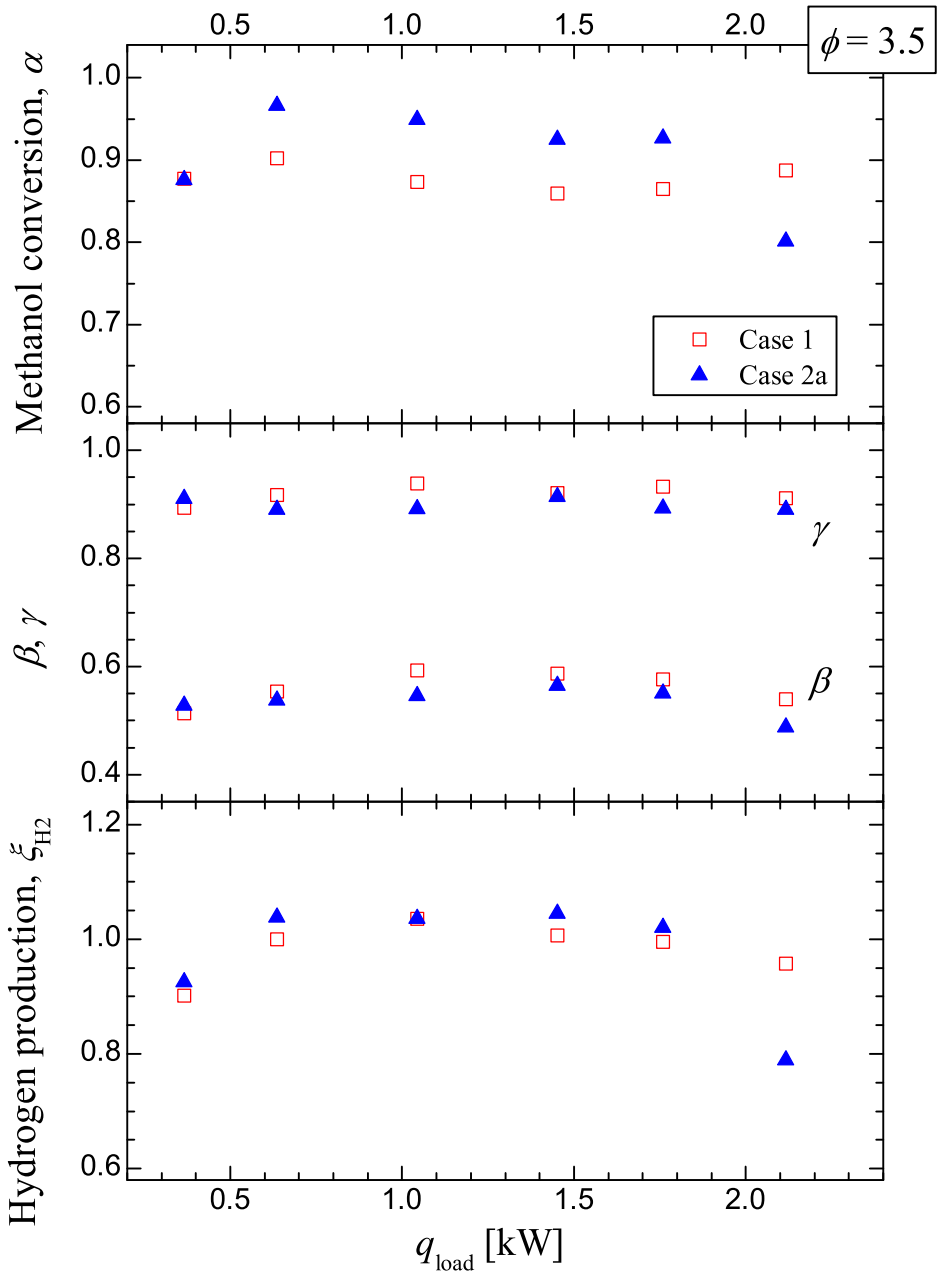

Figure 5.13: Comparison of reforming evaluation parameters in $\phi = 3.5$ between Case 1 and Case 2a. (a) Methanol conversion ratio, α. (b) Preferential production ratios, β and γ. (c) Hydrogen production ratio, ξ_{H2}.

of Honeycomb B. POX has much slower reaction speed than normal combustion in a stoichiometry, so that the reaction takes place within as wide as several millimeters to one centimeter. Thus, the temperature distribution within this reaction region is very important for the reaction, especially for α. The flame in $q_{\mathrm{load}} = 2.12\,\mathrm{kW}$ of $\phi = 3.5$ existed at $x/D \approx 3.8$. This reaction region existed very close to the inlet surface of Honeycomb B, thus the quenching effect of Honeycomb B came into effect.

The values of β and γ experienced a slight decrease, however, the changes of these parameters are small in the whole range of q_{load} in both ϕ cases. This is because the difference in the flame temperature was up to 50 K, that is not enough to shift the chemical equilibrium and to alter the product compositions.

Because the distributions of β and γ did not change from Case 1 to Case 2a, the trend in ξ_{H2} is similar to that in α. However, ξ_{H2} is affected also by the slight decrease in β of Case 2a, therefore, the enhancement of ξ_{H2} was limited up to several %.

From these results, it was found that Honeycomb B could be used as an radiation converter that enhanced the preheating of the mixture gas and decomposition reaction of methanol. However, if the flame is formed close to the outlet of Honeycomb A, the insertion of Honeycomb B caused a shifting of the flame into Honeycomb A, resulting in a drastic decrease in temperature and deterioration of α and ξ_{H2}. Therefore, the effective use of the secondary ceramic honeycomb needs to be carefully determined in accordance with the location of the flame.

Through the discussion, it was confirmed that the non-catalytic methanol POX reaction was stabilized and possibly enhanced using ceramic honeycomb by its nature as a porous material. Honeycomb A worked as a flame stabilizer due to its highly convective heat transfer characteristic. A stable flame of POX was possible in a wide range of equivalence ratio and thermal load conditions. By adding Honeycomb B, higher temperature in the reaction region was realized which increased the methanol conversion ratio by enhancing the mixture preheating and methanol decomposition. Due to the increase in temperature, however, the preferential production ratio of H_2 was slightly

decreased, thus the enhancement of the overall hydrogen production ratio, ξ_{H2}, was limited up to several %.

5.4 Conclusions

In this chapter, based on the knowledge obtained in the previous chapters, the concept of energy regeneration was applied to the present fuel reformer in order to enhance the POX reaction. By regenerating energy from the reforming gas in the post-reaction region, it was estimated that the preheating of the mixture gas was enhanced resulting in the improvement of the reaction efficiency.

As a method of energy regeneration, a porous material working as a radiation converter was introduced. For this purpose, the secondary honeycomb (Honeycomb B) having the same dimensions as the primary honeycomb (Honeycomb A) was introduced with the gap distance Δx. Honeycomb B worked as a radiation converter which regenerated a portion of the enthalpy of the reforming gas by means of radiation emission. By introducing the radiation converter in the post-reaction region, the temperature in the reaction region was increased and the methanol conversion, α, was enhanced. However, the enhancement of the overall hydrogen production ratio, ξ_{H2}, was limited to the smaller thermal load, q_{load}, conditions because of the reduction of the preferential production ratio of H_2, β.

Then, it was revealed that the optimum configuration of the ceramic honeycomb is needed according to the equivalence ratio, ϕ, and q_{load} conditions to obtain the enhancement of the reaction, otherwise the quenching effect of the ceramic honeycomb reduces the reaction efficiency drastically. The results and obtained knowledge are listed as follows:

- It was confirmed that introducing Honeycomb B in the post reaction region increased the maximum flame temperature.

- The effect of energy regeneration was observed first in the outer region. By increasing the amount of energy regeneration by reducing Δx, the effect of energy regeneration spread into more inner region.

- By the effect of Honeycomb B, the flame location was shifted upstream. The stable reaction without liftoff was obtained in more larger q_{load} conditions. In smaller q_{load},

on the other hand, the flame became easier to move into Honeycomb A in Case 2.

- Methanol conversion ratio, α, was increased in a wide range of q_{load} by Honeycomb B. However, in smaller and larger q_{load} conditions, the quenching effect of Honeycomb A and Honeycomb B came into effect due to the closely located flame to the respective honeycombs.

- The enhancement of hydrogen production ratio, ξ_{H2}, was limited up to several % in Case 2 since the temperature increase conversely reduced the preferential production ratio of H_2, β, slightly.

Bibliography

[1] Weinberg, F. J., "Combustion Temperatures: The Future?", *Nature*, Vol. 233, No. 5317 (1971), pp. 239–241.

[2] Echigo, R., "Effective Conversion Method between Gas Enthalpy and Thermal Radiation and Its Application to Industrial Furnaces", *Transactions of Japan Society of Mechanical Engineers Ser. B*, Vol. 48, No. 435 (1982), pp. 2315–2323 (in Japanese).

[3] Yoshizawa, Y., Hayashi, A., and Echigo, R., "An Application of A Porous Medium Radiant Heat Exchanger to A Reactor for Methane Steam Reforming: The Concept and the Analysis of Basic Operation Characteristics", *Transactions of Japan Society of Mechanical Engineers Ser. B*, Vol. 54, No. 504 (1994), pp. 2192–2197 (in Japanese).

[4] Okuyama, M., Echigo, R., Yoshida, H., Koda, M., and Hanamura, K., "Spectral Radiation Properties of Super Fuel-Rich Premixed Flame", *Transactions of Japan Society of Mechanical Engineers Ser. B*, Vol. 60, No. 577 (1994), pp. 3145–3152 (in Japanese).

[5] Jugjai, S., and Polmart, N., "Enhancement of Evaporation and Combustion of Liquid Fuels through Porous Media", *Experimental Thermal and Fluid Science*, Vol. 27 (2003), pp. 901–909.

[6] Lammers, F. A., and de Goey, L. P. H., "A Numerical Study of Flash Back of Laminar Premixed Flames in Ceramic-Foam Surface Burners", *Combustion and Flame*, Vol. 133 (2003), pp. 47–61.

Chapter 6

Conclusions

6.1 Summary of the Thesis

In this study, we investigated on the reaction and heat transfer characteristics of non-catalytic partial oxidation (POX) of methanol for the purpose of applying to a 1-kW-class compact fuel reformer. Because of the instability of the POX reaction, a porous material was applied to the fuel reformer as a flame stabilizer. Then, the optimum use of a porous material regarding the reforming performance and reaction stability was investigated. A ceramic honeycomb was chosen as a porous material to produce hydrogen-rich gas in case the POX reaction is stabilized in the vicinity of the honeycomb.

The experiments were conducted to examine the influential factors such as equivalence ratio and mixture flow rate on the reaction characteristics. The effects of these factors on temperature distribution, flame shape and location, and product compositions were examined. The aim of the study was to propose the criteria on designing compact fuel reformer using porous material through the investigation of the POX reaction in terms of thermal engineering.

In Chap. 2, we explored the basic fuel reforming reactions, considering the significance of the on-site hydrogen production in the transition period to the hydrogen society, including POX, steam reforming (STR), autothermal reforming (ATR), as well as CO purification reactions. The reaction characteristics, the appropriate catalysts, and the overall system

construction for each reaction were investigated. Through the investigation, the advantages and disadvantages of the POX reaction which was focused on the present thesis were clarified. The importance of detailed investigation in this chapter is attributed to the practical application of the POX reaction to the fuel reformer. The requirements of the fuel reformer was then presented by considering energy efficiency of the hydrogen system. Several components of hydrogen energy system were combined and the overall efficiency was compared with the conventional power generation method using internal combustion engine. The degree of feasibility and the performance requirements of the fuel reformer in terms of energy efficiency were indicated.

In Chap. 3, the basic reaction characteristics of methanol POX were investigated. First, chemical equilibrium composition of methanol POX was calculated to clarify the effects of equivalence ratio and reaction temperature on the hydrogen production. The results showed that the equivalence ratio and reaction temperature have positive and negative correlations to the hydrogen production efficiency, respectively. In case the reaction takes place in an adiabatic temperature, higher equivalence ratio is favorable to the hydrogen production. Based on the chemical equilibrium calculation, honeycomb-type compact fuel reformer was then fabricated. When the ceramic honeycomb was applied to the reactor, the POX flame was stabilized in the outlet vicinity of the honeycomb due to the enhancement of preheating of the mixture by means of the internal heat recirculation through the reactor wall and honeycomb solid. The results of gas analysis showed that the methanol conversion ratio monotonically decrease with an increase in equivalence ratio, while the preferential production ratio of hydrogen increase with equivalence ratio. The overall reaction performance was optimized at a slight fuel-rich condition of $\phi = 3.5$ because of the trade-off relation between the conversion ratio and preferential production ratio of hydrogen.

In Chap. 4, the thermal effect of the ceramic honeycomb on the POX reaction was studied. Experiments were conducted by varying thermal load at fixed equivalence ratios. This was due to reveal the effect of the flame shape and location on the reaction

performance. In relatively large thermal load conditions, the flame of POX formed a conical shape where most of the reaction took place at a distance from the honeycomb. In such a case, the thermal interaction between the flame and the ceramic honeycomb was limited to the flame attachment point. On the other hand, the reaction is deteriorated drastically in smaller thermal load conditions. In this case, the flame is formed close to the ceramic honeycomb and the solid phase of the ceramic honeycomb is heated up. This high temperature solid surface emits radiation to the downstream region. Thus, in order to correlate the flame shape and its location to the flow and thermal fields within the reactor, visualization of the flame and velocity measurements were conducted. The major cause of the reaction deterioration in smaller thermal load conditions was concluded to be the radiation loss from the solid surface of the ceramic honeycomb to the downstream region.

In Chap. 5, another utility of the ceramic honeycomb—a radiation converter—was applied to the present reformer to further enhance the reaction performance. It is known that a porous material with high porosity can efficiently convert the enthalpy of the working gas to the radiation emission. Therefore, a secondary honeycomb, having the same dimensions with the primary honeycomb, was inserted in the downstream of the flame stabilization region to utilize the regenerated thermal radiation emission. This energy regeneration contributes to the enhancement of the mixture preheating resulting in higher rate of methanol conversion. Therefore, various experiments were conducted and the results were compared with those without the secondary honeycomb in terms of temperature distributions, flame locations, and reforming evaluation parameters. In most of the experimental conditions, the enhancement of the mixture preheating was observed and higher conversion ratio was achieved. The enhancement of the mixture preheating was realized by the radiation emission from the secondary honeycomb. Due to the irradiation from the secondary honeycomb, the reactor inner wall and the outlet surface of the primary honeycomb was heated up, then the mixture gas is additionally preheated through the solid phase of the honeycomb. However, in some smaller and higher thermal load conditions in which the flame was formed very close to either honeycomb, the primary or secondary,

the quenching effect conversely arose and reduced the conversion ratio drastically. It was confirmed that the relative location of the flame to the porous material is the crucial parameter in designing compact fuel reformers using a porous material.

6.2 Suggestion for the Future Work

In this thesis, the basic thermal characteristics of methanol POX reaction was obtained. However, in considering the practical application as a compact fuel reformer, the additional consideration may be required on the basis of the knowledge obtained.

First, as a fundamental investigation of non-catalytic POX reaction in the present study, the mixture gas was formed in an evaporator by the electric band heaters powered by a external power supply. However, in order to achieve a thermally self-sustainable system, this evaporation process also needs to be covered. Thus, total energy management is required, such as the heat exchange between the exhaust gas and the reactant mixture.

Next, to establish more efficient system, water vapor may be introduced to achieve ATR reaction in the reformer. As presented in Chap. 2, ATR reaction can be controlled by the amount of water introduction. By introducing water to the present reactor, the reaction speed and heat release rate decrease. Thus, the reaction rate and stability may deteriorate markedly without an additional procedure of reaction stabilization and thermal management in the reactor. Moreover, due to the existence of water, undesired production of soot or hydrocarbon may reduce the efficiency. The precise management of the reaction based on the control of the mixture composition and temperature profile needs to be established.

Another possibility of the study is to establish more stable and moderate reaction in the reactor. To achieve such a reaction, the mixture concentration may be radially stratified. Concentration-stratified mixture is often used in internal combustion engines. Especially, the stratified-charged engines are throughly studied to reduce NO_x emission and knocking. In the present fuel reformer, on the other hand, the stability of the reaction may be increased by utilizing the stratified mixture; fuel-lean mixture is introduced in the outer region of

the reactor, while fuel-rich mixture in the center region. The overall equivalence ratio, the extent of the stratification are to be explored. The same concept may be applied to the ATR system where oxygen-rich mixture is introduced in the outer region, while water-rich mixture in the center.

Finally, this fuel reformer may be applied other fuels: heavier fuels, low quality fuels, and bio-derived fuels. The knowledge obtained in this thesis may be applied. The dependence of the reaction and performance on fuels may be important when considering the fuel diversity of fuel reformer. Therefore, the knowledge of various fuels on the optimum hydrogen production are expected.

Nomenclature

a, b, c	temporary coefficients of the quadratic equation	[–]
A_i	area of surface i	[m^2]
c_p	specific heat	[kJ/(mol·K)]
D	inner diameter of the stainless steel reactor	[mm]
D_{qz}	inner diameter of the quartz glass reactor	[mm]
e_b	energy transferred through the boundary of the system	[kJ/mol]
f	calculated flame shape	[mm]
$F_{i,j}$	view factor from surface i to surface j	[–]
h	enthalpy	[kJ/mol]
Δh	enthalpy increase of the system	[kJ/mol]
ΔH	reaction heat release per mole	[kJ/mol]
k, l, m, n	coefficients in the chemical formula of the fuel $C_nH_mO_lN_k$	[–]
K	equilibrium constant of the WGS reaction	[–]
L_{rad}	radiation loss rate ($= q_{rad}/q_{POX}$)	[–]
M	molar flow rate	[mol/s]
p	absolute pressure	[Pa]
q_i	emissive power from surface i	[W]
q_{load}	thermal load	[kW]
q_{POX}	ideal net heat release rate of the POX reaction	[W]
q_{rad}	net radiation through downstream surface of Honeycomb A	[W]
r	radial coordinate in the reactor	[mm]
R_{qz}	inner radius of the quartz glass reactor	[mm]

Re_D	Reynolds number ($= \rho U_{\mathrm{m}} D_{\mathrm{qz}}/\mu$) [–]
S_{L}	laminar burning velocity [m/s]
T	temperature [K]
T_{gas}	gaseous reaction temperature in calculation [K]
U_x	streamwise velocity [m/s]
U_{m}	cross-sectional averaged streamwise velocity [m/s]
$\dot{V}$	volumetric flow rate [mL/min] or [L/min]
x	streamwise coordinate in the reactor [mm]
Δx	gap distance between Honeycomb A and Honeycomb B [mm]
y, Y	gas concentration [–]

Greek Symbols

α	conversion ratio of methanol [–]
β	preferential production ratio of H_2 [–]
γ	preferential production ratio of CO [–]
ϵ	stoichiometric molar ratio of fuel to O_2 [–]
ε	emissivity [–]
ζ	reaction ratio of POX in ATR reaction [–]
η_{el}	electrical efficiency of the system [–]
θ	inclination angle of the flame to the orthogonal plane to the axis [rad]
μ	viscosity coefficient of air [Pa·s]
ν_i	coefficient of the species i in the product mixture [–]
ξ	production ratio [–]
ρ	density of air [kg/m^3]
σ	Stefan-Boltzmann constant [W/(m^2·K^4)]
ϕ	equivalence ratio of the combustion reaction [–]

subscripts

0	initial condition
i	species number
i, j	surface number
Tmax	values at the maximum temperature location
X	species X value
af	adiabatic flame value
air	air value
ceram	ceramic value
CH3OH	methanol value
consumed	consumed amount value
ex	values by the wall-attached thermocouples
fuel	fuel value
in	values by the radial-type thermocouples
max	maximum value
qz	quartz glass value
r	reforming gas value
s	sample gas value
st	stoichiometry value
supplied	supplied amount value
u	unreacted gas value

superscript

j	iteration step in the calculation